Universiteit
Leiden
The Netherlands

Visualizing strongly-correlated electrons with a novel scanning tunneling microscope

Battisti, I.

Citation
Battisti, I. (2019, May 8). *Visualizing strongly-correlated electrons with a novel scanning tunneling microscope*. *Casimir PhD Series*. Retrieved from https://hdl.handle.net/1887/72410

Version:	Not Applicable (or Unknown)
License:	Leiden University Non-exclusive license
Downloaded from:	https://hdl.handle.net/1887/72410

Note: To cite this publication please use the final published version (if applicable).

Cover Page

Universiteit Leiden

The handle http://hdl.handle.net/1887/72410 holds various files of this Leiden University dissertation.

Author: Battisti, I.
Title: Visualizing strongly-correlated electrons with a novel scanning tunneling microscope
Issue Date: 2019-05-08

Visualizing strongly-correlated electrons with a novel scanning tunneling microscope

Proefschrift

ter verkrijging van
de graad van Doctor aan de Universiteit Leiden,
op gezag van Rector Magnificus prof. mr. C.J.J.M. Stolker,
volgens besluit van het College voor Promoties
te verdedigen op woensdag 8 mei 2019
klokke 11:15 uur

door

IRENE BATTISTI

geboren te Padova, Italië
in 1990

Promotor:	Prof. dr. J. Aarts	Universiteit Leiden
Co-promotor:	Dr. M.P. Allan	Universiteit Leiden
Promotiecommissie:	Prof. dr. P. Wahl	University of St. Andrews
	Prof. dr. C. Morais-Smith	Universiteit Utrecht
	Prof. dr. K. Schalm	Universiteit Leiden
	Prof. dr. E.R. Eliel	Universiteit Leiden

Casimir PhD series, Delft-Leiden 2019-09.
ISBN 978-90-8593-391-5

An electronic version of this thesis can be found at:
`https://openaccess.leidenuniv.nl`

This work is supported by the Netherlands Organization for Scientific Research (NWO/OCW) as part of the Frontiers of Nanoscience (NanoFront) program and the VIDI talent scheme (Project No. 680-47-536).

The cover shows a (Fourier-filtered) atomically-resolved STM topographic image measured by the author on Sr_2RhO_4. Few atomic defects act as scatterers for quasiparticles, resulting in the formation of standing waves that interfere with each other. The width of the author name corresponds to a scalebar of 2 nm.

Contents

1 Introduction **1**

1.1 Studying correlated electrons with a scanning tunneling microscope . . 1

1.2 From Mott insulators to high-T_c superconductors 3

1.3 Outline of this thesis 7

2 The experimental technique: spectroscopic-imaging scanning tunneling microscopy **9**

2.1 Scanning tunneling microscopy 10

2.1.1 STM as a probe of the local density of states 12

2.1.2 Tunneling into many-body systems 14

2.2 Spectroscopic-imaging STM 15

2.3 Probing momentum space: quasiparticle interference 17

2.3.1 Comparing STM and photoemission 18

2.4 STM on materials with poor electronic screening 19

2.5 Energy resolution in STM 21

3 Dome: design and construction of an ultra-stable scanning tunneling microscope 23

3.1 Introduction . . . 25
3.1.1 The technical challenge of building an STM . . . 25
3.1.2 Reducing vibrations in STM . . . 27
3.2 The STM head . . . 29
3.2.1 STM head design . . . 30
3.2.2 Improving the geometry with finite element analysis . . . 32
3.2.3 Measurement of resonant frequencies . . . 35
3.3 Cryogenic insert . . . 37
3.4 Vibration isolation table . . . 39
3.5 UHV chamber . . . 39
3.6 Performance . . . 40
3.6.1 Current and height noise at the tunneling junction . . . 40
3.6.2 Quasiparticle interference on Sr_2RhO_4 . . . 42
3.7 Conclusions . . . 44

4 Universality of pseudogap and emergent order in lightly doped Mott insulators 45

4.1 Introduction . . . 47
4.2 The electron-doped iridate $(Sr_{1-x}La_x)_2IrO_4$ . . . 47
4.3 Sample characterization . . . 49
4.4 Doping level determination with STM . . . 51
4.5 Low doping levels: frozen Mott state . . . 52
4.6 High doping levels: pseudogap and electronic order . . . 54
4.6.1 Phase separation . . . 54
4.6.2 Mapping pseudogap and Mott gap . . . 55
4.6.3 Emergent order . . . 58
4.7 Doping evolution: a sharp transition . . . 60
4.8 Discussion and conclusions . . . 63

5 Poor electronic screening in lightly doped Mott insulators 65

5.1 Introduction 66

5.2 Poor electronic screening and tip-induced band bending 66

5.3 Influence of poor screening on the energy gap of $(Sr_{1-x}La_x)_2IrO_4$ . . . 67

5.3.1 Calculation of the band-bending potential 69

5.3.2 Algorithm to retrieve the real energy scales in the LDOS . . . 72

5.4 Bubbles in the conductance layers of $(Sr_{1-x}La_x)_2IrO_4$ 74

5.5 Conclusions 78

6 Quasiparticle interference in the correlated metal Sr_2RhO_4 81

6.1 Introduction 82

6.2 The correlated metal Sr_2RhO_4 83

6.3 SI-STM quasiparticle interference measurements 86

6.4 Identification of scattering vectors: comparison with simulations . . . 89

6.5 Extraction of dispersions and Fermi vectors 92

6.6 Comparison with ARPES 94

6.7 Conclusions 96

7 Conclusions and outlook 99

Bibliography 103

Samenvatting 115

Publications 119

Curriculum Vitae 121

Acknowledgements 123

1

Introduction

1.1 Studying correlated electrons with a scanning tunneling microscope

Modern solid-state physics successfully describes the electronic properties of many solids within the framework of band theory [1]. Its most surprising aspect is the assumption that the interactions between the valence electrons are negligible, despite them carrying charge and therefore being subject to Coulomb repulsion. Many electronic and thermal properties of conventional materials can, indeed, be described in this independent-electron approximation, where the electron interactions are treated as a perturbation of the single-electron properties. These concepts are the foundation of Landau's Fermi-liquid theory. In this theory, the electronic properties of materials are described by single particle-like excitations that are called *quasiparticles*. Quasiparticles can be considered as electron-like particles that have renormalized properties, such as their mass, in order to take the interactions into account [2].

There are materials, however, where the Coulomb interaction between electrons is so strong that it cannot be treated by Landau's theory. These materials go under the name of *strongly-correlated electron systems*. The Fermi-liquid description fails to reproduce their physical properties, because the picture of independent quasiparticles does not hold any longer. These systems are characterized by emerging collective behavior that cannot be simply described by adding single-particle excitations. To quote P.W. Anderson: 'More is different' [3]. Strongly-correlated electrons are found

in a variety of materials, and are responsible for some of the most intriguing phenomena in condensed-matter physics, including high-temperature superconductivity, Mott physics and quantum criticality.

The field of correlated-electron systems has been initially driven by the experimental discovery of a number of novel, engineered materials. In the last thirty years, progress in material science has facilitated the growth of better crystals, and improvement of scientific instrumentation has brought to the acquisition of data with ever-increasing quality. We believe that these advances, combined with the efforts in the development of new theoretical techniques, are key to understand the emergent collective properties of quantum materials.

Among the experimental techniques that are used to study strongly-correlated electron systems, spectroscopic-imaging scanning tunneling microscopy (SI-STM) stands out for its ability to resolve electronic inhomogeneities at the atomic scale [4]. The power of SI-STM lies in its ability to directly measure the local density of states (LDOS) of the sample with very high energy and spatial resolution. This allows, for instance, the visualization of the effect of a single impurity atom on the electronic structure. This (otherwise unattainable) resolution achieved by STM is particularly important in the study of strongly-correlated electron systems, that are often characterized by nanoscale inhomogeneities in the electronic structure.

In the last twenty years, SI-STM has proven to be very successful in the study of correlated-electron systems. However, performing SI-STM experiments is technically challenging: most prominently, the technique is extremely sensitive to external vibrations, that easily impact the data quality and bury important features in the noise. For this reason, specially designed equipment is required to achieve good data quality.

This thesis discusses our contribution to the progress of the field of strongly correlated-electron systems in two main areas. The first is the construction of a new, home-built, cryogenic STM that is stiffer than any other reported in literature to date (where stiffness directly implies high stability against vibrational noise and thus better data quality). The second is the study of the physics of lightly doped Mott insulators, a prototypical example of how strong electron-electron correlations give rise to unusual phases of matter.

In the remainder of this introduction, we first give a general overview to the physics of Mott insulators, and then briefly review cuprate high-temperature superconductors, as an example of the exotic phases of matter that appear upon doping a Mott insulator (Sec. 1.2). This allows us to introduce several concepts that will be used throughout this thesis. Finally, in Sec. 1.3, we give an outline of the thesis.

1.2 From Mott insulators to high-T_c superconductors

Mott insulators are the simplest example of the effect of strong electron-electron correlations. Band theory fails to describe them, predicting that they would be metallic. Their theoretical description, however, is very simple once electron-electron repulsion is taken into account. It was first proposed by Nevill Mott as follows [5–7]: consider a lattice model as illustrated in Fig. 1.1a, with a single orbital per atom and one electron on each site (half filling). When the electrons move through the lattice with (hopping) kinetic energy t[1], some sites occasionally become doubly occupied. This is opposed by the on-site Coulomb repulsion U. If $U \gg t$, the hopping of the electrons from site to site is energetically suppressed. Electrons then localize on the atomic sites, and the material becomes insulating simply because the electrons can not move. They can be thought of as frozen at their atomic locations. Even if the electrons are localized, their spins are in principle still free to point in all possible directions. However, their interaction energy is minimized when they are either in parallel or antiparallel configuration. By considering virtual hopping processes, it is shown that they organize in an antiferromagnetic ground state [7].

From a different point of view, one can see how 'switching on' the Coulomb interaction affects the density of states [8]. This is schematically illustrated in Fig. 1.1b. For $U = 0$, i.e. without electron-electron correlations, a single band of width W forms from the overlap of the atomic orbitals; with single occupancy of each site, the system is metallic. The bandwidth W can be obtained from tight-binding calculations as $W =$

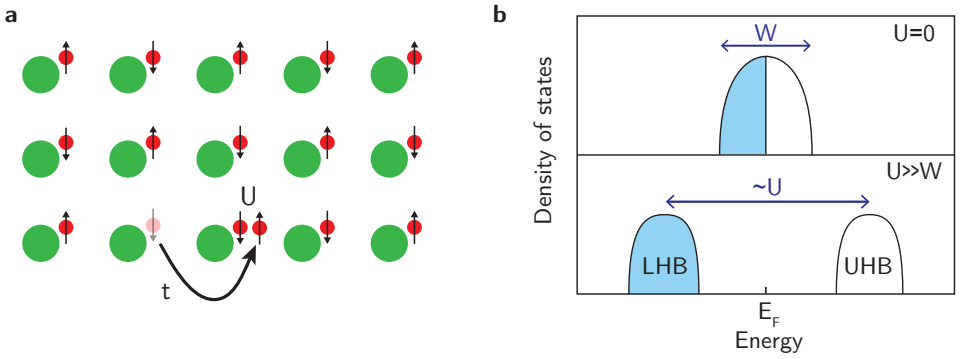

Figure 1.1: **a**, Cartoon picture of a Mott insulator. The kinetic hopping energy t competes with the on-site Coulomb repulsion U. **b**, Schematic illustration of the opening of the Mott gap, with the formation of a filled lower Hubbard band (LHB) and an empty upper Hubbard band (UHB); adapted from Ref. [8].

[1]Here, t represents the hopping matrix elements as defined in standard tight-binding models, and it contains the kinetic energy associated with the motion through the lattice.

$2zt$, where t represents the hopping matrix elements and z is the number of nearest neighbors, e.g., z=2 in one dimension, z=4 in a square lattice. The bandwidth is therefore related to the kinetic energy of the electrons. If $U \gg W$, a gap opens around the Fermi level, with the creation of two subbands. The lower band represents states with singly-occupied sites, while the upper band corresponds to states with doubly-occupied sites. These bands are called lower and upper Hubbard bands, respectively. Note how different this is from a band insulator or a semiconductor: instead of an energy gap determined by the periodic potential of the crystal lattice, we now have a gap that is entirely due to electron correlations.

But which materials are most likely to be Mott insulators? In other words, what governs the relation between U and W, and what are typical values in real materials? In a solid, the atoms are close together: the closer the atomic orbitals are to each other, the more the hopping term t (and therefore the bandwidth W) increases. At the same time, the bare Coulomb interaction U gets screened and becomes smaller. Transition metal oxides with $3d$ valence electrons are very good candidates to become Mott insulators, with a relatively narrow bandwidth ($W \approx 1 - 3\,\mathrm{eV}$) and large Coulomb interaction ($U \approx 5$ eV). Indeed, some of the vanadates, nickelates, cobaltates, and, most prominently, cuprates, are found to be Mott insulators. When moving in the periodic table towards the more spatially extended orbitals of $4d$ and $5d$ transition metal oxides, the bandwidth increases and the electron correlations are reduced. As we show in chapter 6, the $4d$-transition metal oxide rhodate Sr_2RhO_4 is a correlated metal that can almost perfectly be described by Fermi-liquid theory. With increasing atomic numbers, however, other quantities become relevant, in particular spin-orbit coupling. We will show in chapter 4 that indeed the interplay of bandwidth, Coulomb interaction and spin-orbit coupling can cause the $5d$-transition metal oxide iridate Sr_2IrO_4 to be a Mott insulator, even if Coulomb interactions for $5d$ transition metal oxides are strongly reduced and the bandwidths are larger.

The physics of Mott insulators as discussed thus far is well understood within the framework of the Hubbard model, and can be described by the Mott-Hubbard Hamiltonian:

$$H(t,U) = -t \sum_{<i,j>} c^{\dagger}_{i\sigma} c_{j\sigma} + U \sum_{i=1}^{N} n_{i\uparrow} n_{i\downarrow} \tag{1.1}$$

where $< i, j >$ indicates the sum over nearest neighbors, $c^{\dagger}_{i\sigma}(c_{i\sigma})$ creates (annihilates) an electron with spin σ on a lattice site i, and $n_{i\sigma} = c^{\dagger}_{i\sigma} c_{i\sigma}$ is the number operator. The model considers only electrons in a single band. Despite this being a considerable simplification, low-energy properties of several real systems are well-described by this model, because typically only a small number of bands (sometimes just one) are crossing the Fermi level [6].

If the description of a Mott insulator is relatively simple and successful, the situation becomes more complicated very quickly once one moves away from the Mott insulating state. This can happen by tuning external parameters like pressure, temperature or insertion of extra carriers (doping) [6, 9]. Due to the strong electron correlations, small changes of these external parameters strongly influence the properties of the system, giving rise to fascinating, emergent, collective behaviors and complex phase diagrams.

One of the most interesting and studied phases emerging from doped Mott insulators is unconventional, high-temperature superconductivity. In the remainder of this section, we will focus on cuprates, copper-oxide-based high-T_c superconductors, and we will give a description of their phase diagram.

Cuprates are a family of layered materials with perovskite crystal structure, characterized by the presence of CuO_2 planes. Since the discovery of high-temperature superconductivity in 1986[2], the chemical composition of cuprates has been tuned until reaching $T_c = 135\,\mathrm{K}$ [11]. Typically, their unit cells are large and complex, containing heavy elements such as Bi, Hg, and Ba.

In the parent state, without the insertion of extra carriers, the copper atoms are in the Cu^{2+} $3d^9$ configuration with half-filled $d_{x^2-y^2}$ orbitals. They are typical Mott insulators, with the localized spins arranged in an antiferromagnetic ground state. When doped with extra carriers[3], they show a wide number of different behaviors, as illustrated in the phase diagram in Fig. 1.2. Importantly, the strong Coulomb repulsion, that causes the parent compound to be a Mott insulator, keeps being the dominant interaction, also in the doped compound. The electrons are thus strongly correlated even in the phases that appear upon doping, and Fermi-liquid theory is unable to describe them. Understanding the cuprates phase diagram indeed remains one of the biggest open problems in condensed-matter physics [11].

We will now give a very brief overview of the electronic phases that are encountered in the phase diagram. We mainly follow Ref. [11], and, as a conclusion, emphasize the main contributions that the use of scanning tunneling microscopy has given to the field.

High-T_c superconductivity emerges at low temperatures upon doping, and spans a dome-shaped area around the so-called optimal doping level, where the highest T_c is achieved. The electron-pair wave function (also called order parameter) has d-wave symmetry, making it an unconventional superconductor — opposed to conventional

[2]High-T_c superconductivity was first found in $La_{2-x}Ba_xCuO_4$ ($T_c \approx 30\,\mathrm{K}$) by Bednorz and Müller [10], who were awarded the Nobel prize for the discovery in 1987.

[3]The highest T_c and the most interesting electronic phases are observed upon hole-doping. The effects of electron-doping cuprates have also been studied (see Ref. [12] for a review); here, we focus on hole-doped cuprates.

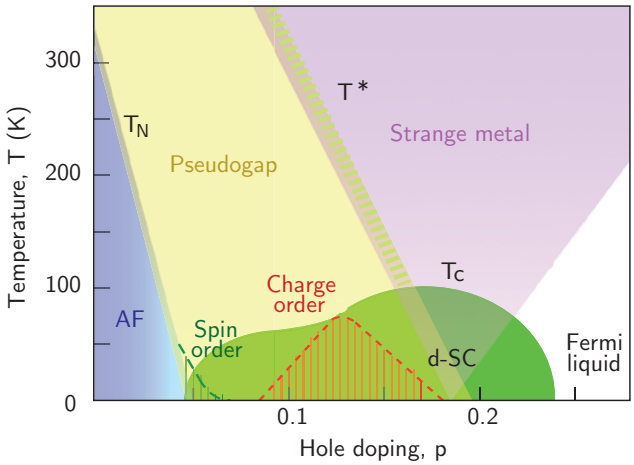

Figure 1.2: Phase diagram of cuprates, as a function of hole doping and temperature. Adapted from Ref. [11].

BCS superconductors, where the superconducting wave function has s-wave symmetry. This causes the superconducting gap to be anisotropic in momentum space.

When the temperature is raised, a variety of exotic electronic behaviors emerge, most of which are not yet fully understood. At low doping and high temperature, a very mysterious phase appear at the threshold indicated by T^*. It is called the *pseudogap* phase, because it is characterized by a depletion of the density of states close to the Fermi level, measured by several experimental techniques. Its origin is still under debate; one hypothesis is that at T^* electron pairs already start to form, however the superconducting order is suppressed by phase fluctuations. Between the pseudogap and the superconducting phase, at relatively low temperatures, a series of *intertwined orders* appear [13]. Their origin can be ascribed to the short-range antiferromagnetic correlations inherited from the Mott state, and they are believed to compete with superconductivity.

At high temperature, around optimal doping, cuprates enter the so-called *strange metal* phase. The name is due to the fact that the transport properties are remarkably different from the ones of 'normal' metals. The most striking example is the behavior of the resistivity ρ as a function of temperature: while in a normal Fermi liquid ρ grows quadratically with temperature and finally saturates according to the Mott-Joffe-Regel criterion[4], in cuprates $\rho \propto T$, and this behavior persists up to very high temperature. The strange metal phase has been proposed to be related to quan-

[4]The Mott-Joffe-Regel criterion puts a lower limit to the conductivity of metals, corresponding to a minimum mean free path equal to the lattice constant. This, in turn, puts an upper limit to the resistivity [14].

tum criticality emerging from the presence of a quantum critical point under the superconducting dome near optimal doping. This would imply the absence of quasiparticle excitations in this phase of matter.

Scanning tunneling microscopy greatly contributed to the understanding of the phase diagram of the cuprates, and allowed, among others, the visualization of nanoscale electronic disorder [15–17], the determination of the superconducting gap structure by quasiparticle interference [18], and the imaging of local symmetry breaking in the pseudogap phase [19, 20]. In the present work, we use STM to elucidate the transition between the Mott insulating state and the pseudogap phase for the iridate Sr_2IrO_4, that we find has striking similarities to the cuprates.

1.3 Outline of this thesis

In this thesis we aim to better understand correlated electron systems using spectroscopic-imaging STM. To this end, we both develop new scientific instrumentation and study correlated electron systems with an emphasis on lightly doped Mott insulators. The thesis is organized as follows.

Chapter 2 gives an introduction to the experimental technique of spectroscopic-imaging scanning tunneling microscopy and to the interpretation of its data.

Chapter 3 describes the design, construction and performance of our newly built ultra-stable scanning tunneling microscope, which we called *Dome*[5]. The microscope is the stiffest against external vibration reported to date, which makes it particularly suited to study quasiparticle interference. It lead to the experimental results presented in chapter 6.

Chapters 4 and 5 are dedicated to the study of lightly doped Mott insulators. The measurements have been performed with a commercial STM, in parallel to the construction phases of the home-built microscope. In chapter 4, we investigate the melting of the Mott state upon the addition of extra carriers in the Mott insulator Sr_2IrO_4. We show the appearance, at sufficient doping, of a pseudogap phase and of emergent order, and we are able to precisely elucidate how this state develops from the Mott insulating phase. In chapter 5, we focus on the special situation that is encountered when STM experiments are performed on materials with poor electronic screening. Our motivation stems from the results of chapter 4, where, at very low doping levels, we find discrepancies with other experimental techniques. Here, we develop a model that explains our results and reconciles them with literature.

[5] Referring, among other things, to the superconducting dome of unconventional superconductors.

Chapter 6 shows quasiparticle interference measurements on the correlated metal Sr_2RhO_4, which is an example of a 2D Fermi liquid. These are the first measurements that we perform with the home-built STM described in chapter 3.

Finally, chapter 7 gives some concluding thoughts and an outlook of the possible measurements that can be performed with the microscope *Dome* in the near future.

2

The experimental technique: spectroscopic-imaging scanning tunneling microscopy

2.1 Scanning tunneling microscopy

The working principle of scanning tunneling microscopy (STM) is based on quantum tunneling. To achieve tunneling, a sharp metallic tip is brought close to the flat surface of a conducting sample (typically a few angstroms), as illustrated in Fig. 2.1a. When a bias voltage is applied between tip and sample, electrons can tunnel through the vacuum gap between the two, just as they tunnel through a potential barrier in textbook, one-dimensional quantum tunneling [21]. This creates a measurable tunneling current, typically of the orders of pico- to nanoamperes, that decays exponentially with the distance between tip and sample. The tip is then scanned over the surface using a feedback loop that keeps the tunneling current constant by adjusting the tip-sample distance. By recording the vertical position of the tip at every location, a topographic image of the surface is created.

In Fig. 2.1b, we show an example of such an STM image (from now on called *topograph*) measured on the top BiO layer of a $Bi_2Sr_2CaCu_2O_{8+\delta}$ (BSCCO) sample. Atomic resolution is achieved, with the Bi atoms visible on the surface. The additional long-wavelength vertical corrugation is typical of the material and commonly called supermodulation. Importantly, the contrast in STM topographs is given by a mixture of geometrical height and electronic structure, whose contributions cannot generally be separated from each other.

The main motivation of Binnig and Roher, who invented STM and won a Nobel prize for it, was, however, not to construct a scanning probe technique, but to have an instrument able to perform tunneling spectroscopy locally on an area less than 100 Å in diameter [22]. Tunneling spectroscopy is a very powerful tool, and the combination of topographic information with spatially-resolved spectroscopy is indeed what made STM so important for understanding solid-state physics, and in particular quantum materials.

The process of incorporating spectroscopy in STM quickly developed from the first pioneering experiments on semiconductors [23] and metals [24, 25] to the study of BCS superconductors [26] and unconventional high-T_c superconductors. It is on the latter materials that the technique manifested its full potential, because they have an intrinsically inhomogeneous electronic structure at the nanoscale [15, 16]. Overall, performing spectroscopy with STM greatly outperformed the 100 Å-resolution goal of Binnig and Roher, since the technique can easily distinguish the effect of single impurity atoms on the density of states with picometer resolution [27, 28].

In the rest of this chapter, we motivate why the combination of STM with tunneling spectroscopy is ideally suited to study quantum matter. We start by showing that STM gives a local view into the density of states by deriving the expression for the tunneling current and the tunneling spectra (Sec. 2.1.1). We then introduce the tech-

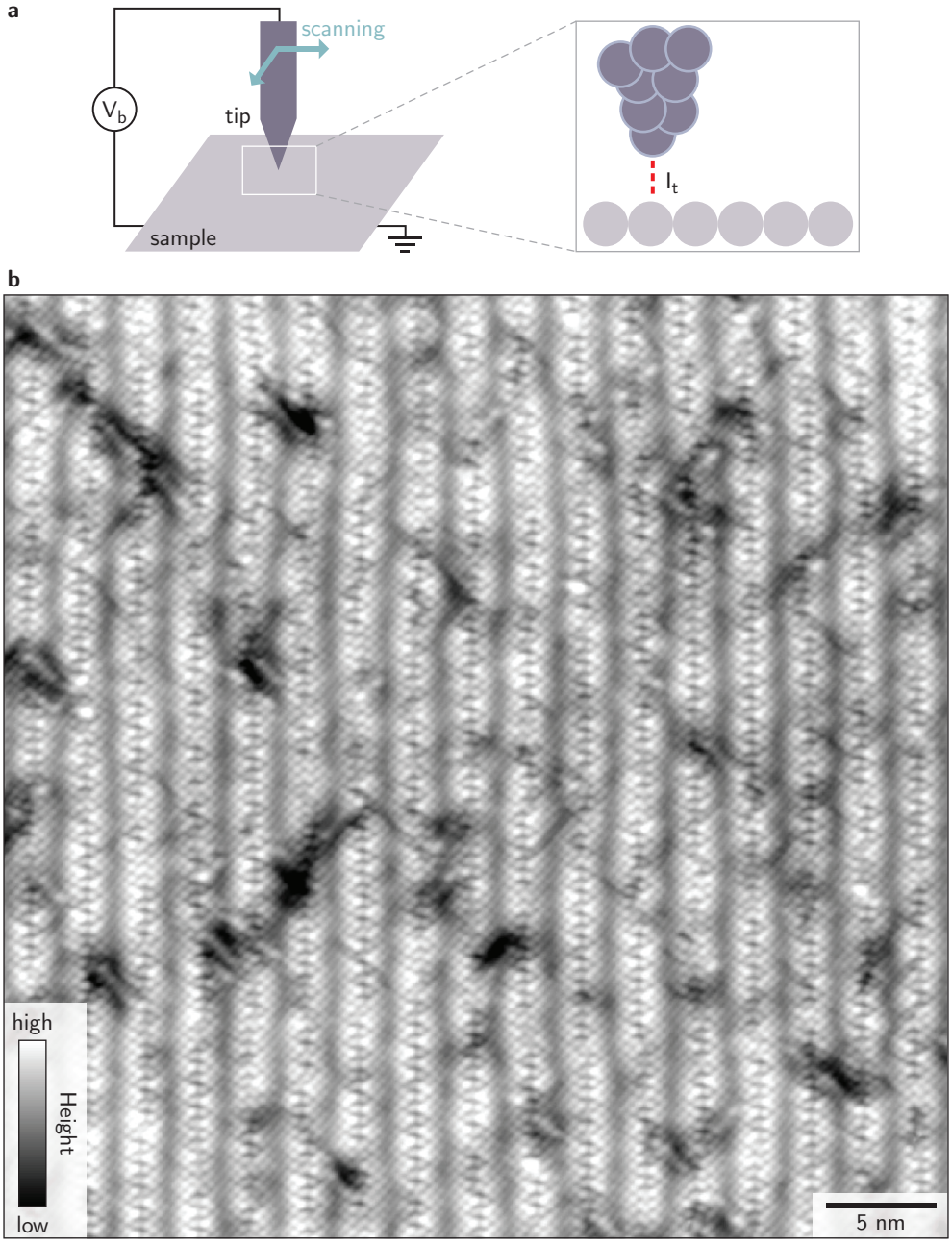

Figure 2.1: **a**, Cartoon picture of the working principle of an STM. **b**, Topograph measured on an underdoped $Bi_2Sr_2CaCu_2O_{8+\delta}$ sample ($T_c = 40\,K$). The field of view is $43 \times 43\,nm^2$ and the setup conditions are (V_b=160 mV, I_t=80 pA). Atoms and the extra corrugation known as supermodulation are resolved. Some defects of unknown origin are also visible on the surface.

nique of spectroscopic-imaging STM (Sec. 2.2), that yields powerful 3-dimensional datasets. We discuss several possibilities to analyze these datasets in order to obtain deep insights into the physics of the materials, both in real and in momentum space (Sec. 2.3). Finally, we introduce a tip-induced artifact that we will encounter in chapters 4 and 5 of this thesis (Sec. 2.4), and we conclude with a comment on energy resolution in STM (Sec. 2.5).

2.1.1 STM as a probe of the local density of states

Here, we give a brief derivation of the tunneling current between tip and sample, illustrating how it is related to the *local* density of states (LDOS) of the sample [29, 30].

In Fig. 2.2, the density of states of tip and sample, $g_{\mathrm{t}}(\epsilon)$ and $g_{\mathrm{s}}(\epsilon)$, respectively, are sketched next to each other. The tip is a good metal, and therefore its density of states (DOS) can be considered flat in the proximity of the Fermi level, while the sample has, in general, a more complicated DOS. If tip and sample are electrically connected, the two chemical potentials μ_{t} and μ_{s} are aligned at the same energy. Applying a positive bias voltage V_{b} to the sample causes its chemical potential μ_{s} to shift downwards by eV_{b} with respect to μ_{t}. Now, electrons can tunnel from the occupied states of the tip to the empty states of the sample within the energy window eV_{b}. At finite temperatures, the occupation probability for the electronic states is given by the Fermi-Dirac distribution

$$f(\epsilon, T) = \frac{1}{1 + \exp[(\epsilon - \mu)/(k_{\mathrm{B}}T)]}, \tag{2.1}$$

where μ is the chemical potential and k_{B} the Boltzmann constant. The number of occupied states on the tip at energy ϵ is therefore given by $g_{\mathrm{t}}(\epsilon) \cdot f(\epsilon, T)$, while the number of available states on the sample is $g_{\mathrm{s}}(\epsilon) \cdot [1 - f(\epsilon, T)]$. From now on, for simplicity, we set the chemical potential of the sample at zero energy, $\mu_{\mathrm{s}} = 0$. This is indeed the convention that is used in real STM measurements.

The tunneling current from tip to sample can be calculated as the integral over all energies of the number of filled states on the tip times the number of empty states on the sample. There is also a small contribution of electrons tunneling from the sample to the tip. The total tunneling current can obtained by summing this two opposite currents, and it is expressed as:

$$I(V_{\mathrm{b}}, h) = -2e\frac{2\pi}{\hbar}\int_{-\infty}^{+\infty} |M(h)|^2 \left[f(\epsilon) - f(\epsilon - eV_{\mathrm{b}})\right] g_{\mathrm{s}}(\epsilon)\, g_{\mathrm{t}}(\epsilon - eV_{\mathrm{b}})\, \mathrm{d}\epsilon. \tag{2.2}$$

Here, the factor 2 takes the two possible spin states into account, the factor $2\pi/\hbar$ is derived from perturbation theory, and $|M(h)|^2$ represents the tunneling matrix

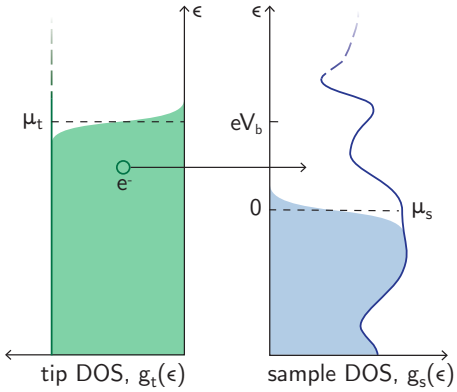

Figure 2.2: Schematic representation of the tunneling process between tip and sample density of states.

elements, which contain the exponential dependence of the tunneling current on the tip-sample distance h. The broadening of the Fermi-Dirac distribution is quantified by $k_\mathrm{B}T$. At liquid helium temperature, where all measurements reported in this thesis are performed, $k_\mathrm{B}T = 0.36\,\mathrm{meV}$. This is very sharp compared to typical features in the DOS, and therefore we can approximate the Fermi-Dirac distribution by a step function. This significantly simplifies the tunneling current to

$$I(V_\mathrm{b}, h) = \frac{4\pi e}{\hbar} \int_0^{eV_\mathrm{b}} |M(h)|^2 \, g_\mathrm{s}(\epsilon) \, g_\mathrm{t}(\epsilon - eV_\mathrm{b}) \, \mathrm{d}\epsilon. \tag{2.3}$$

Under the realistic assumptions that the tunneling matrix elements do not depend on energy and that g_t is flat in energy (a condition that is verified before every measurement by obtaining a flat DOS on a featureless gold sample), the expression for the tunneling current can be further simplified:

$$I(V_\mathrm{b}, h) = \frac{4\pi e}{\hbar} |M(h)|^2 \, g_\mathrm{t} \int_0^{eV_\mathrm{b}} g_\mathrm{s}(\epsilon) \, \mathrm{d}\epsilon. \tag{2.4}$$

The tunneling current therefore depends directly on both tip-sample separation h and the integrated sample density of states. Since STM probes the sample locally, it actually measures the *local* density of states, $\mathrm{LDOS}(\mathbf{r}, \epsilon = eV_\mathrm{b})$, defined as the number of electrons per unit volume and energy at a given point in space $\mathbf{r}$ and at a given energy ϵ [29].

Since the tunneling current is proportional to the integrated sample LDOS, its derivative with respect to the bias voltage (the differential conductance) is proportional to

the local density of states of the sample:

$$\frac{\partial I(V_\mathrm{b}, h)}{\partial V_\mathrm{b}} = \frac{4\pi e^2}{\hbar} |M(h)|^2 \, g_\mathrm{t} \, g_\mathrm{s}(eV_\mathrm{b}) \, . \tag{2.5}$$

This is exactly what is measured in a tunneling spectroscopy experiment, and it is commonly called a $\mathrm{d}I/\mathrm{d}V$ tunneling spectrum.

In practice, in order to acquire such a spectrum, the tip is brought in tunneling with setup conditions $(V_\mathrm{s}, I_\mathrm{s})$. This means that a bias voltage V_s is applied, and the feedback adjusts the tip-sample distance until the current reaches I_s. The feedback is then switched off and the bias voltage is swept while recording changes in the current to obtain a current-voltage (IV) curve. For bias voltage $V_\mathrm{b} > 0$ applied to the sample, electrons will tunnel from tip to sample, probing the unoccupied sample states. For $V_\mathrm{b} < 0$, electrons will tunnel from sample to tip, probing the occupied sample states.

Taking the numerical derivative of such acquired IV curves provides the sample LDOS as a function of energy. However, numerical derivatives usually enhance the noise. To overcome this problem, it is standard technique to use a lock-in amplifier to modulate the bias voltage with an amplitude $\mathrm{d}V$ and to directly measure the demodulated value of the current $\mathrm{d}I$. In this way, the differential conductance can be directly measured as a $\mathrm{d}I/\mathrm{d}V$ spectrum, where the energy resolution is given by the amplitude of the lock-in modulation. Typical modulations that are used in the work presented in this thesis range from 2 meV (rhodates, chapter 6) to 50 meV (low doping level iridates, chapter 4).

2.1.2 Tunneling into many-body systems: Green's functions and spectral functions

The density of states, that we used to describe the tunneling current so far, is a well-defined concept only for non-interacting electrons. In this case, the available energies for given states with wave vector $\mathbf{k}$ are defined by the dispersion relation. In correlated electron systems, however, even when $\mathbf{k}$ is well defined, the electron-like quasiparticle can exchange energy with other quasiparticles due to interactions. It is then better to use the formalism of many-body systems and express the relevant quantities through Green's functions and spectral functions. A good, full introduction to these concepts can be found in Ref. [31, 32]; here, we focus on expressing the quantities measured with STM in terms of these concepts.

The spectral function $A(\mathbf{k}, \omega)$ can be seen as a generalized version of the density of states for many-body systems, since it represents the probability of finding a single-particle excitation at a given energy ω and momentum $\mathbf{k}$. The tunneling equation can be fully derived using spectral functions instead of density of states, leading to the same final result that the tunneling current is proportional to the integrated local

density of states [32]. The local density of states can in fact be expressed as the *local* spectral function $A(\mathbf{r},\omega) = \sum_{\mathbf{k}} A(\mathbf{k},\omega;\mathbf{r})$, which is in turn related to the many-body retarded Green's function $G(\mathbf{r},\omega)$ by:

$$\mathrm{LDOS}(\mathbf{r},\omega) = A(\mathbf{r},\omega) = -\frac{1}{\pi}\mathrm{Im}[G(\mathbf{r},\omega)]. \tag{2.6}$$

STM tunneling spectra therefore measure the local (in real-space) spectral function averaged over all momenta [32, 33].

Experimentalists in strongly correlated electron systems are often acquainted with the concept of spectral functions from angle-resolved photoemission spectroscopy (ARPES), which directly measures the spectral function in momentum space. We show how the two techniques compare in section 2.3.1.

2.2 Spectroscopic-imaging STM

We now introduce spectroscopic-imaging STM[1], which is the most powerful technique to measure topographic and spectroscopic information simultaneously. It consists of measuring a $\mathrm{d}I/\mathrm{d}V$ spectrum for every pixel of a simultaneously acquired topograph. The result is a three-dimensional dataset representing the local density of states as function of position and energy, $\mathrm{LDOS}(r_x, r_y, \epsilon)$. Such a dataset is commonly called a *spectroscopic map*. Most of the data presented in this thesis is collected in this form.

A typical spectroscopic map contains 10^4–10^5 $\mathrm{d}I/\mathrm{d}V$ spectra, that are acquired one after the other. The feedback is only active when moving the tip to the new location, and switched off while acquiring the spectra. This makes this type of measurement extremely sensitive to external vibrations. Such a measurement can last from one to several days (it is typically limited by the hold time of the cryostat). SI-STM therefore puts highest demands on the stability of the microscope.

A spectroscopic map is extremely rich in information which can be extracted and analyzed in several different ways. In Fig. 2.3, we show a visual representation of a spectroscopic map, together with examples of data analysis options that are used throughout this thesis. One can look at the data 'vertically' (i.e. along the energy), analyzing the $\mathrm{d}I/\mathrm{d}V$ spectra one by one. For example, it is interesting to observe how they change with location, and how they are influenced by the presence of a dopant atom or an impurity in the crystal. This can be well visualized in *waterfall* plots. Additionally, a properly chosen function can be fitted to every single spectrum to extract locally changing parameters. A well-known example is extracting the width

[1] Note that the terms spectroscopic-imaging STM (SI-STM), Fourier-transform STM (FT-STM) and scanning tunneling spectroscopy (STS) are often used interchangeably. Here, we will use the convention SI-STM.

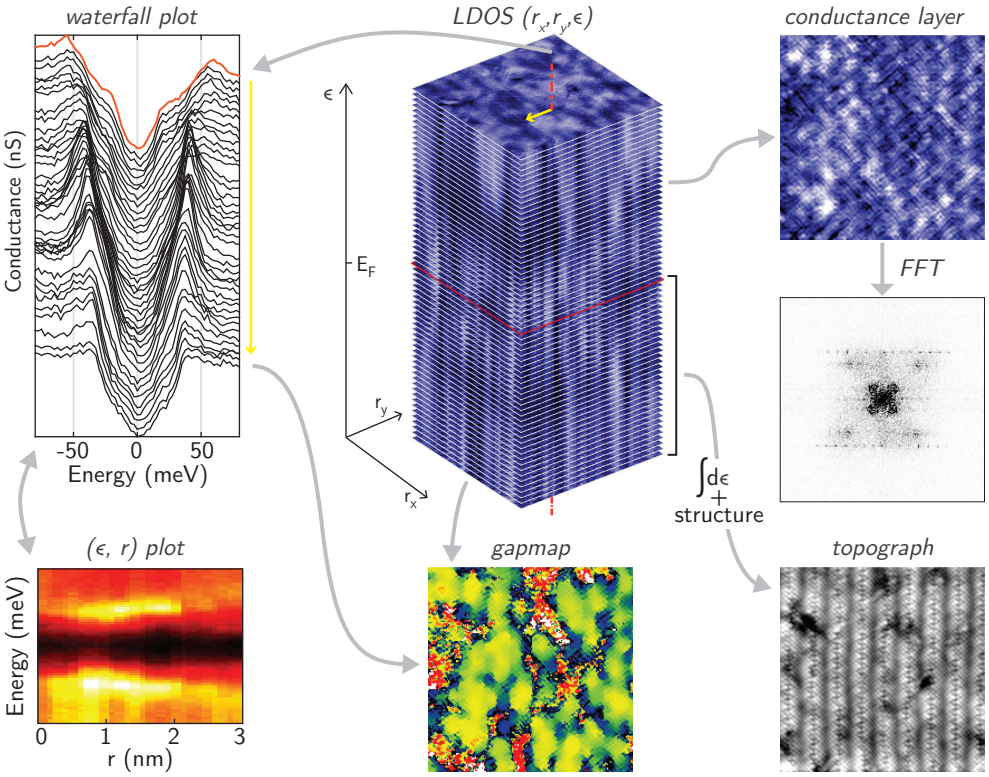

Figure 2.3: SI-STM generates 3-dimensional datasets. Exploring the data along different directions opens many data analysis options. The data shown as example is measured on an underdoped $Bi_2Sr_2CaCu_2O_{8+\delta}$ sample (T_c= 40 K). The field of view is 21×21 nm^2.

of the superconducting gap in unconventional superconductors [16]. This can then be used to build a so-called *gapmap*, where the magnitude of the gap is given as an intensity plot as function of location. Alternatively, one can look at the data 'horizontally' (i.e. along the spatial coordinates), directly analyzing the constant-energy conductance layers. They can reveal spatially organized structures hinting towards charge order or wave-like patterns indicating quasiparticle interference. When the conductance layers show periodicity, their Fourier transform can provide additional quantitative information.

2.3 Probing momentum space: quasiparticle interference

SI-STM is a direct probe for real space properties, but it can also access momentum space information through quasiparticle interference (QPI) imaging. This technique has been initiated by observing standing waves caused by QPI on the surface of Cu(111) [24]. Briefly afterwards, it was realized that quantitative information about the scattering vectors could be obtained by Fourier transforming the images of the standing waves pattern [25]. The technique has since then been extensively used, and it proved to be particularly powerful in the study of unconventional superconductors [18, 34–36], heavy fermions [37, 38] and topological insulators [39–41]. In the present section, we briefly explain the phenomenon of quasiparticle interference using the simple example of a metal, based on Ref. [30]. The concepts that we introduce here will then be applied in chapter 6 to study QPI in the correlated metal Sr_2RhO_4.

In an ideal metal, the quasiparticle eigenstates are Bloch wave functions with the periodicity of the crystal lattice. They are characterized by the momentum $\mathbf{k}$, and their energy must follow the dispersion relation $\epsilon(\mathbf{k})$. The presence of crystal defects or impurities causes elastic scattering of the quasiparticles, that mixes states with different wave vectors $\mathbf{k}_1$, $\mathbf{k}_2$ but same energy $\epsilon(\mathbf{k})$. The result of scattering are standing waves with wave vectors $\mathbf{q}(\epsilon) = \mathbf{k}_1(\epsilon) - \mathbf{k}_2(\epsilon)$. These standing waves and their interference pattern can be directly imaged in the conductance layers of spectroscopic maps measured with SI-STM.

In Fig. 2.4a, we show an example of standing waves on Cu(111) caused by quasiparticles scattering off a single impurity on the surface. By taking the two-dimensional

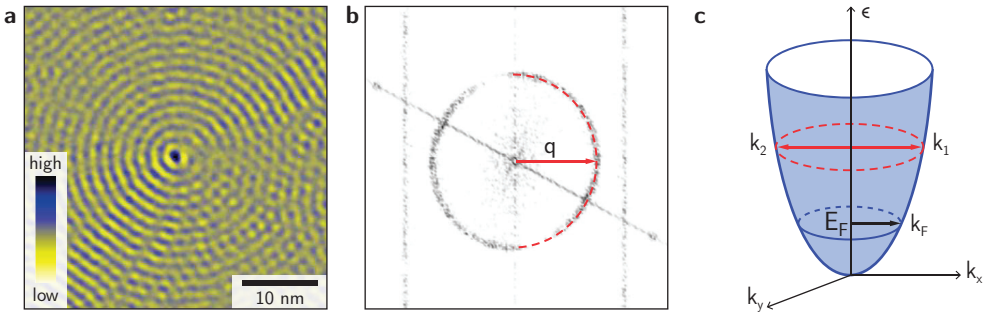

Figure 2.4: **a**, QPI on Cu(111) in real space: conductance layer at 50 meV around a single impurity scattering center. The field of view is 45 nm^2. Adapted from Ref. [42]. **b**, QPI in Fourier space: Fourier transform of panel **a**. Adapted from Ref. [42]. **c**, Cartoon picture representing the band structure of a 2D metal.

Fourier transform of such a conductance layer, an image in momentum space is obtained, as shown in Fig. 2.4b. Here, the magnitudes of the quasiparticle scattering vectors $\mathbf{q}$ are plotted as a function of direction. The pattern seen in the Fourier transformed images is related to the band structure of the material. For a 2D electron gas, the band structure is a paraboloid where the constant energy contours are circles with radius $k(\epsilon)$, as illustrated in Fig. 2.4c. The Fourier transform of the conductance layers will therefore be dominated by circles with radius $q(\epsilon) = 2k(\epsilon)$. The QPI pattern in real and momentum space will evolve with energy, reflecting the increasing diameter of the constant energy contours. By tracking the magnitude of scattering vectors $\mathbf{q}$ as a function of energy, one can measure their dispersion and extract information about the electronic properties of the material.

In general, it is challenging to identify the origin of the scattering vectors $\mathbf{q}$ without previous knowledge of the band structure. In a simplistic picture, the wave vectors $\mathbf{q}$ that dominate the QPI pattern correspond to a large joint DOS (JDOS) of pairs of $\mathbf{k}$ vectors. High JDOS can arise from regions in k-space where the constant energy contours are parallel, as for example in the quasi one-dimensional bands of Sr_2RuO_4 [43]. Alternatively, high JDOS arises from scattering that connects flat regions in the dispersion, where the density of states is significantly larger. In cuprates, this is at the origin of the well-known octet model for QPI in $Bi_2Sr_2CaCu_2O_{8+\delta}$ [18].

2.3.1 Comparing STM and photoemission

The most successful direct probe of momentum space is angle-resolved photoemission spectroscopy (ARPES), which is also a surface sensitive technique. Having seen that STM can also be used as a (indirect) probe for momentum space, it is interesting to compare its results with the ones of ARPES.

ARPES is based on the photoelectric effect. A beam of photons incident on the surface of a material can excite and eventually cause the emission of electrons from the material. By directly measuring the energy and momentum of the emitted electrons, one can reconstruct the band structure. Under a series of approximations (that go under the name of *sudden approximation*), the photocurrent measured by ARPES can be expressed in terms of the single-particle spectral function, $A(\mathbf{k}, \omega)$, as [44]:

$$I_{\mathrm{ARPES}}(\mathbf{k}, \omega) = I_0 \, |M_{f,i}|^2 \, f(\omega) \, A(\mathbf{k}, \omega), \tag{2.7}$$

where $M_{f,i}$ represents the photoemission matrix elements, and $f(\omega)$ is the Fermi-Dirac distribution.

We showed in section 2.1.2 that STM probes the local density of states, which can be expressed as the (real-space) local spectral function averaged over all momenta. The ARPES signal, on the other hand, is proportional to the spectral function in

momentum space, averaged over a real-space area corresponding to the photon beam size [32]:

$$I_{\mathrm{STM}} \propto A(\mathbf{r},\omega) = -\frac{1}{\pi}\,\mathrm{Im}\,[G(\mathbf{r},\omega)], \tag{2.8}$$

$$I_{\mathrm{ARPES}} \propto A(\mathbf{k},\omega) = -\frac{1}{\pi}\,\mathrm{Im}\,[G(\mathbf{k},\omega)]. \tag{2.9}$$

STM and ARPES data cannot be mathematically related to each other simply by a spatial Fourier transform, because their relationship involves terms that are not measured [33].

However, in a simplified JDOS picture for the origin of QPI, STM data can still be compared with ARPES through autocorrelation approaches [45–47]. Here, high JDOS for the scattering vectors $\mathbf{q}$ can be described as [47]:

$$\mathrm{JDOS}(\mathbf{q},\omega) = \int A(\mathbf{k}+\mathbf{q},\omega)A(\mathbf{k},\omega)\,\mathrm{d}^2k. \tag{2.10}$$

This corresponds to the autocorrelation of constant energy ARPES images when photoemission matrix elements are neglected. This approach to compare STM QPI and ARPES data is very simplified, though it is useful to at least qualitatively recognize the origin of the scattering vectors observed in FT-STM images.

We use this autocorrelation approach in chapter 6, to aid the identification of scattering vectors observed on the correlated metal Sr_2RhO_4.

2.4 STM on materials with poor electronic screening

The tunneling current equation obtained in Sec. 2.1.1 assumes as a starting point that the sample is metallic. STM experiments can, however, also be performed on materials that have a small gap around the Fermi level (up to 2-3 eV), such as semiconductors or lightly doped Mott insulators. These materials, differently than metals, are characterized by poor electronic screening, which can affect the interpretation of STM results.

We encounter such a situation in our STM measurements on Sr_2IrO_4 (chapter 4), which leads to some artifacts in the data. Here, we give a brief introduction to this phenomenon, and derive how it affects the tunneling current equation (2.4). Chapter 5 is dedicated to explore this effect in more detail, in order to have a correct interpretation of the experimental data measured on materials with poor elecronic screening.

To understand the effect of poor electronic screening in STM measurements, we consider a standard tip-sample configuration, and assume for simplicity that the bias

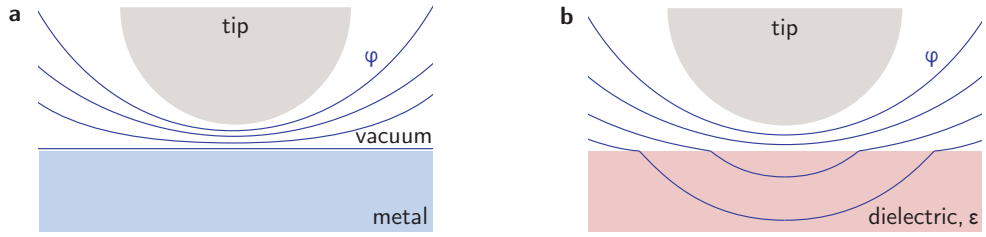

Figure 2.5: Equipotential lines in STM experiments showing different screening of electric fields in different materials. **a**, In standard STM experiments on metals, the electric field generated by the tip is largely screened within the first atomic layer and there is no significant field penetration. **b**, In samples with a gapped density of states at the chemical potential, the electric field can penetrate the sample due to poor electronic screening.

voltage is applied to the tip. When a metallic sample like copper is placed in the electric field generated by the STM tip, the field is almost perfectly screened and the sample has a uniform potential. If the bottom of the sample is grounded, the full sample will be at zero electric potential, and the tunneling equation Eq. (2.4) holds. This scenario changes if the sample is not a metal: the electric field generated by the tip can then partially penetrate the sample surface, causing an additional potential drop inside the sample. This is schematically depicted in Fig. 2.5. Because the potential landscape in the sample changes in a way similar to how bands bend at semiconductor interfaces, this effect is known as *tip-induced band bending* (TIBB) [48–50].

Tip-induced band bending will affect the tunneling equations because the surface of the sample directly below the STM tip will not be at zero potential, but at some finite potential φ_{BB}. The tunneling current in the presence of band bending at $T \sim 0\,\mathrm{K}$ is therefore given by

$$I(V_{\mathrm{b}}, h) = \frac{4\pi e}{\hbar}\,|M(h)|^2 \int_0^{eV_{\mathrm{b}}-\varphi_{\mathrm{BB}}(V_{\mathrm{b}},h)} g_s(\epsilon)\, g_t\big(\epsilon - eV_b + \varphi_{\mathrm{BB}}(V_{\mathrm{b}}, h)\big)\,\mathrm{d}\epsilon, \qquad (2.11)$$

which, in the assumption of constant tip DOS, simplifies to

$$I(V_{\mathrm{b}}, h) = \frac{4\pi e}{\hbar}|M(h)|^2\, g_t \int_0^{eV_{\mathrm{b}}-\varphi_{\mathrm{BB}}(V_{\mathrm{b}},h)} g_s(\epsilon)\,\mathrm{d}\epsilon. \qquad (2.12)$$

It is essential to know the expression for φ_{BB} if one wants to extract quantitative information about the LDOS from tunneling spectroscopy experiments. In the semiconductor community, the phenomenon of TIBB is well known, and methods to compute φ_{BB} in order to get a correct interpretation of the data are available (for example, the Poisson's equation solver developed by Feenstra [51]). In lightly doped Mott insulators, on the other hand, the phenomenon of TIBB is less studied, and the models developed for semiconductors cannot be applied. In chapter 5, we thoroughly discuss

the phenomenon of TIBB for this case, with an application to the lightly doped Mott insulator Sr_2IrO_4.

2.5 Thermal broadening and energy resolution in STM

To obtain the expression for the tunneling current shown in Eq. (2.4), we approximated the Fermi-Dirac distribution by a step function. This is licit only when $T = 0\,\mathrm{K}$, because for any finite temperature the Fermi-Dirac function has a finite spread of a few $k_\mathrm{B}T$ that broadens all features in energy.

Taking this into account, the question arises of how much the thermal broadening will affect the energy resolution of tunneling spectroscopy. The finite temperature expression for $\mathrm{d}I/\mathrm{d}V$ spectra can be obtained by taking the derivative of Eq. (2.2):

$$\frac{\partial I(V_\mathrm{b})}{\partial V_\mathrm{b}} \propto \int_{-\infty}^{+\infty} g_\mathrm{s}(\epsilon)\, \frac{\partial f(\epsilon - eV_\mathrm{b})}{\partial V_\mathrm{b}}\, \mathrm{d}\epsilon \tag{2.13}$$

The derivative of the Fermi-Dirac distribution shows a peak of height $1/(4k_\mathrm{B}T)$ centered at $\epsilon = eV_\mathrm{b}$. A standard measure for the energy resolution is given by the FWHM of this peak [4], that can be easily evaluated being

$$\Delta E = k_\mathrm{B}T \cdot [\ln(3 + 2\sqrt{2}) - \ln(3 - 2\sqrt{2})] = 3.53\, k_\mathrm{B}T\,. \tag{2.14}$$

The energy resolution at 4.2 K is therefore 1.3 meV. We have seen that the resolution of a $\mathrm{d}I/\mathrm{d}V$ spectrum directly measured with a lock-in amplifier is given by the amplitude of the voltage modulation $\mathrm{d}V$. Thermal broadening therefore puts a fundamental lower limit for the smallest value of $\mathrm{d}V$.

3

Dome: design and construction of an ultra-stable scanning tunneling microscope

This chapter has been published as:
Battisti *et al.*, Rev. Sci. Instrum. **89**, 123705 (2018).

3.1 Introduction

This chapter describes the design, construction and performance of our fully home-built scanning tunneling microscope optimized for spectroscopic-imaging measurements, that we called *Dome*. Chapter 2 gives an introduction to the working principle of STM and to the different types of measurements that can be performed, but does not discuss technical challenges. For instance, how is it possible to bring and keep two macroscopic objects such as tip and sample at a constant distance of few angstroms from each other? And more generally, what are the most critical points one has to take care of when designing and building a microscope?

Here, we start in section 3.1.1 by describing the factors that most critically affect STM measurements and, in light of that, we give an overview of the key specifications for designing an STM dedicated to spectroscopic-imaging. We then explain some basic principles of vibration isolation in section 3.1.2, to motivate the choices we made for the design of Dome. In the remainder of the chapter, we discuss the design, construction and performance of the microscope, which is shown in Fig. 3.1 as a computer-aided design (CAD) rendering. We start in section 3.2 with the STM head where tip and sample are placed, therefore the most critical part of the instrument. We show how finite element analysis calculations guide our design choices to obtain a very stiff microscope. Combined with a careful choice of materials, this leads to an STM head that is three times stiffer than what has been previously reported [52]. We continue with a description of the cryogenic insert (Sec. 3.3), the vibration isolation table (Sec. 3.4) and the UHV chamber (Sec. 3.5). Finally, we demonstrate the performance of the microscope by showing vibrational noise spectra and quasiparticle interference data on the correlated metal Sr_2RhO_4 (Sec. 3.6).

All data presented in chapter 2, 3 and 6 of this thesis is acquired with this new microscope.

3.1.1 The technical challenge of building an STM

The exponential dependence of the tunneling current on the tip-sample distance can be considered the main strength of STM, because it is the factor allowing it to resolve atoms. It is however also a considerable drawback: the smallest vibrations coupling to the tip-sample junction from the environment are directly transmitted, exponentially, to the tunneling current signal. And vibrations are, indeed, the main source of noise in STM measurements. When acquiring a topograph, the tip scans over the sample using a feedback mechanism that can partially correct for vibrations transmitted to the junction, as explained in chapter 2. During most spectroscopy experiments, instead, the feedback to the tip is switched off, and even the smallest vibration can

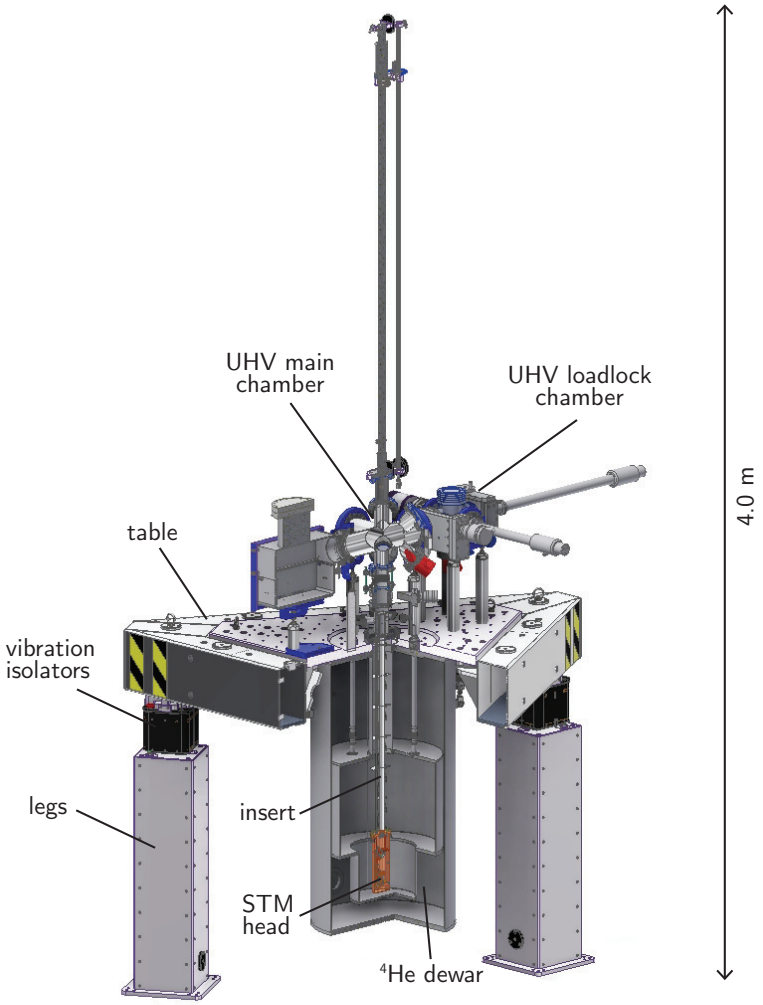

Figure 3.1: Overview of the full Dome microscope. The insert and the STM head are shown by virtually cutting open the CAD rendering. The most significant parts are indicated.

exponentially couple to the tunneling current, causing the $\mathrm{d}I/\mathrm{d}V$ spectra to be significantly noisier. For a spectroscopic map, typically $10^4 - 10^5$ spectra are acquired subsequently over a period of several days (up to a full week of continuous measurement). An extreme stability of the microscope against external vibrations is thus the prime requirement one has to meet when building an STM for spectroscopic imaging.

The other requirements depend on the samples and the physics one wants to study: low temperatures are needed for quantum materials and to achieve higher energy resolution, as explained in section 2.5; ultra high vacuum (UHV) is necessary to

prepare and maintain atomically clean surfaces; a magnet opens the possibility to study samples in a magnetic field.

Our instrument is designed to operate in UHV and at low temperatures, with an achieved base pressure $p = 3 \times 10^{-10}$ mbar and base temperature $T = 4.27$ K. Both low temperatures and UHV requirements make the building more challenging: only a selected amount of materials are compatible with cryogenic and UHV conditions. Moreover, one has to compensate for the different thermal contractions of different materials and to ensure good thermal stability to avoid thermal drift during cool down procedures and measurements.

3.1.2 Reducing vibrations in STM

The transmission of vibrations to the tunneling junction is typically reduced by combining a very rigid microscope construction with the use of a vibration isolation table (and, if available, laboratories with low-vibration facilities). In this section, we show that the reasons underlying this choice can be easily understood by considering both STM head and vibration isolation table as one-dimensional driven harmonic oscillators [29].

The basics of the isolation of a mass m from the vibrations of a reference frame can be understood as follows. Vibrations from the environment cause a time-dependent displacement of the reference frame $X(t)$ that, in turn, causes a displacement $x(t)$ of the mass m, as illustrated in the inset of Fig. 3.2a. We can simplify the induced displacement to a harmonic excitation of frequency ω by using Fourier decomposition. The mass then moves with the same frequency ω as the reference frame, with a phase difference ϕ:

$$\begin{aligned} X(t) &= X_0 \cos(\omega t), \\ x(t) &= x_0 \cos(\omega t - \phi). \end{aligned} \tag{3.1}$$

The equation of motion for the mass m contains the restoring force of the spring, with spring coefficient k, and a damping term, with damping coefficient ν:

$$m\ddot{x} = -k(x - X) - \nu(\dot{x} - \dot{X}). \tag{3.2}$$

It is useful to define the natural frequency of the system by $\omega_0 = 2\pi f_0 = \sqrt{k/m}$, and the damping term by $\gamma = \nu/2m$. One can then solve the equation of motion Eq. (3.2) by using the ansatz of Eq. (3.1), to obtain the expressions for the transfer function $\Gamma(\omega)$ and the phase difference $\phi(\omega)$, plotted in Fig. 3.2a-b, respectively:

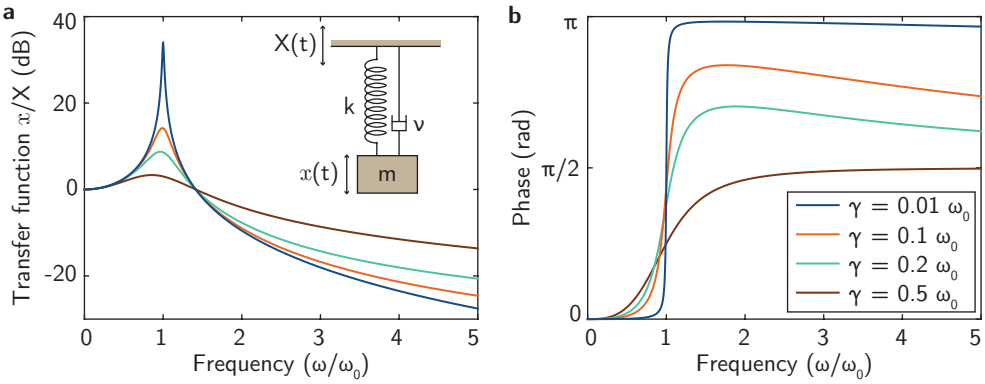

Figure 3.2: **a**, Transfer function of a harmonic oscillator with driven reference frame and damping, from Eq. (3.3). The system is schematically represented in the inset. **b**, Phase between the motion of m and the reference frame, from Eq. (3.4). Both transfer function and phase are shown for different damping values γ.

$$\Gamma(\omega) = \frac{x_0}{X_0} = \sqrt{\frac{\omega_0^4 + 4\gamma^2\omega^2}{(\omega_0^2 - \omega^2)^2 + 4\gamma^2\omega^2}}\,, \tag{3.3}$$

$$\phi(\omega) = \tan^{-1}\left(\frac{2\gamma\omega^3}{\omega_0^2(\omega_0^2 - \omega^2) + 4\gamma^2\omega^2}\right). \tag{3.4}$$

The problem of vibration isolation is to reduce the transfer function at all frequencies, while trying to push the resonance to a frequency where it is harming the least. Note that higher damping γ reduces the resonance peak height, but worsens the efficiency of vibration isolation for $\omega \gg \omega_0$ (see Fig. 3.2a). It is, therefore, necessary to find a compromise between reducing the peak height and having better isolation at higher frequency.

In an STM, typically one can find two systems that resemble such a harmonic oscillator. The first one is the vibration isolation table, with the table acting as the mass that is decoupled from the vibrating floor by means of (typically commercial) springs. Their natural frequency, $f_{\mathrm{iso}} = \omega_{\mathrm{iso}}/2\pi$, should be as low as possible, in order to have vibrations at most frequencies falling on the right-hand side of the resonance peak, where the transfer function is small (Fig. 3.2a). The second system resembling a harmonic oscillator is the STM head, with the sample as the reference frame, the tip as the mass, and the STM head connecting the two as the spring. In this case, one wants to avoid relative displacement between tip and sample, and this is achieved by having a very high value of the natural frequency $f_0 = \omega_0/2\pi$ for the STM head. One would then have most vibrations coupling on the far left-end side of the resonance peak, where the displacement is in phase, meaning that tip and sample will not move

relative to each other. In a continuous system such as the STM head, f_0 corresponds to the frequency of its first vibrational eigenmode, and it is directly related to the stiffness.

But what are the numbers in a real setup? The most damaging vibrations for STM measurements are in the 0−100 Hz range, introduced by people walking in the building, resonances of the building, and traffic (0−10 Hz), and by air ventilation and other appliances (10−100 Hz).

The vibration isolators of the table typically have a natural frequency f_{iso} of a few hertz (from 1-2 Hz for compressed air isolators, down to 0.5 Hz for negative spring coefficient isolators). The vibration isolation can be improved further by having a multiple stage system, where the STM table is placed on a heavy concrete block that is, in turn, resting on springs. This lowers f_{iso} further, however there is a lower limit at about 0.1 Hz.

The most room for improvement lies in the value of f_0 for the STM head. Typically, f_0 lies in the 1−5 kHz range, but can be increased of about one order of magnitude by choosing a smart design and stiff materials [29, 52], as we will show in the following. Obtaining a very stiff STM head, with the highest possible f_0, is, indeed, our main focus during the design phase.

3.2 The STM head

The STM head is often the most critical part in the determination of the microscope's performance. It needs to both guarantee a very stiff tip-to-sample connection and to provide an approach mechanism that allows to bring the tip from few millimeters away from the sample to tunneling distance. A beautiful solution to this problem was found 20 years ago by Pan et al. [53], with a design that is to date the best one for a cryogenic STM head. The stiffest cryogenic-compatible STM head that is reported in literature to date is based on this design, using oriented single-crystalline sapphire as the material for the body of the STM head [52]. This is our starting point. To improve the stiffness further, we optimize the geometry of all the components of the head with finite element analysis (FEA) calculations, towards achieving a higher f_0 of the fully assembled STM head.

Before describing the STM head design, we want to emphasize why sapphire is the ideal material from which to machine an STM head. Before White el al. (Ref. [52]) introduced sapphire as the main building material, the materials that have been used for STM heads are Macor or metals like titanium or molybdenum, mostly because they are much easier to machine. We note that is generally preferable to machine the STM head from an insulating material, to avoid the risk of electrical shorts. From

Material	ρ [g/cm^3]	E [GPa]	ν [-]	κ (4K) [W/m/K]
sapphire (Al_2O_3 99.99%)	3.98	360 - 440	0.32	100
Macor	2.52	66.9	0.29	0.1
titanium	4.54	110.3	0.32	0.1
molybdenum	10.22	330	0.32	60

Table 3.1: Properties of materials typically used for STM heads. Density ρ, Young's modulus E and Poisson's ratio ν are the structural properties defining the stiffness of the material. The thermal conductivity at low temperatures κ gives an indication for the thermalization times. The structural properties of sapphire and Macor are from Ref. [55]. The thermal properties at low temperatures are extracted from tables of Ref. [54] for sapphire, of Ref. [56] for Macor, and from Ref. [57] for the metals.

a quick look at the material properties in Table 3.1, it is clear that sapphire has the advantage of being stiffer, with a Young's modulus[1] much higher than Macor. Moreover, sapphire has an exceptionally high thermal conductivity at low temperatures, which is comparable to the one of copper and greatly exceeding the one of any other insulating material[2]. The main drawback of sapphire is that the material is very difficult to machine and prone to cracks. Recent advancements in production technology, however, allowed us to machine more complicated and detailed sapphire parts for the STM head than it was previously possible.

3.2.1 STM head design

The assembled STM head is shown in Fig. 3.3, in both CAD rendering and photographs.

Its main body is a hollow sapphire cylinder open on one side, inside which a triangular polished sapphire prism (the slider) is clamped via six shear piezo stacks[3] and a molybdenum plate acting as spring. The piezo stacks are glued with non-conductive epoxy[4] to the sapphire body, while the triangular prism is just clamped, and can

[1] The Young's modulus defines the relationship between stress and strain, and it is the mechanical property that measures the stiffness of a solid material.

[2] This is due to the extreme purity of single crystalline sapphire: heat in electrical insulators is carried only by phonons, and at low temperatures phonons are scattered only by defects and crystal boundaries, which are very rare in sapphire [54].

[3] P-121.01T from PI Ceramics, customized with height 2.7 mm, and polished Al_2O_3 end plates.

[4] Epotek H74F.

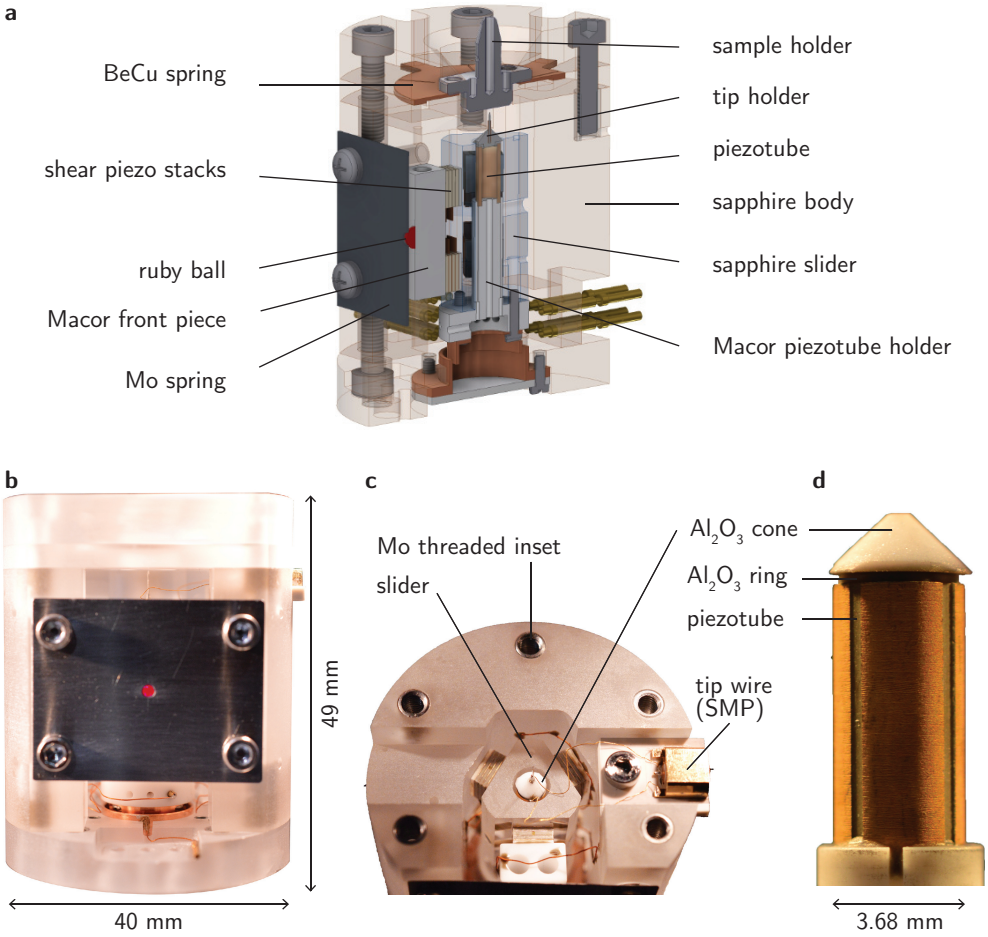

Figure 3.3: **a**, Cross section of the 3D CAD rendering of the STM head, with the main components being pointed out. **b**, Photograph of the fully assembled STM head. **c**, Top view of the open STM head, showing the slider construction and the tip holder. **d**, Photograph of the piezotube and tip holder during the construction phase.

slide up and down with respect to the body when high voltage pulses are applied to the piezo stacks (principle of stick-slip motion [29, 53]). This whole construction provides the coarse approach mechanism, also called *walker*, that allows to move the tip towards the sample over a 5 mm range with nanometer-sized steps (at 4 K, with 120 V pulses, one step up is about 20 nm). It is essential to the functioning of the walker to have very flat and perfectly parallel surfaces at the contact between the slider and the piezostacks, which requires polishing of the contacting surfaces.

The scanning motion is provided by a piezotube[5], which has four outer electrical contacts for deflections in the ±X, ±Y directions (in-plane) and one inner contact for contractions and elongation in Z. It is driven with maximum ±100 V on all contacts, resulting at 4 K in a XY field of view of 380 nm^2 and a Z elongation of 110 nm. The piezotube is glued with non-conductive epoxy on top of a Macor support which is in turn fixed inside the sapphire prism with screws.

The tip is mounted on a tip holder glued on top of the piezotube. The tip holder assembly is optimized for low weight, in order to increase the resonant frequencies of the scanner, and for low capacitance, in order to allow for high frequency STM measurements [58, 59]. It consists of a small Al_2O_3 ring glued directly on the piezotube, and a conical Al_2O_3 holder glued on the ring. This last piece hosts a small molybdenum cylinder inside which the tip is clamped by friction. The bottom surface of the conical piece is additionally sputtered with 450 nm of gold to provide a ground shield for the tip wire. With this assembly we obtain a tip-to-sample capacitance of 180 fF (at tunneling distance, with tip retracted) and a tip-to-ground shield capacitance of 2 pF. The tip-to-ground shield capacitance should be as low as possible to facilitate high frequency STM measurements, and the value we measure is reduced of more than a factor 10 with respect to commercially available instruments.

The sample holder receptacle is on top of the main body, with the sample facing downwards towards the tip and clamped by a BeCu spring. The scanner is not provided with an XY stage for coarse motion of the sample holder, in order to not reduce the stability of the assembly.

3.2.2 Improving the geometry with finite element analysis

The main factor allowing us to obtain a stiffer STM head is the optimization of the geometry, which we achieve by performing finite element analysis (FEA) calculations with the software package Comsol [60]. FEA calculations have been used before to improve the geometry of various scanning probe techniques [61–64], and in particular of high-scanning-speed STM [65–67], where high resonance frequencies are essential. Here, we use them for the first time to improve the geometry of a low-temperature STM for spectroscopic imaging.

The optimization procedure that we applied to several components of the STM head in order to achieve high resonant frequencies is shown in Fig. 3.4a. As an example, we discuss here how we apply this procedure to the piezotube. After importing the initial design in Comsol, we compute the mechanical eigenfrequencies of the first vibrational modes with the base of the piezotube fixed, as shown in Fig. 3.4b. We can identify two double degenerate bending modes, a rotational mode and a vertical mode. We then

[5] EBL4 from EBL Products. Height 8.0 mm, OD 3.68 mm, wall thickness 0.58 mm.

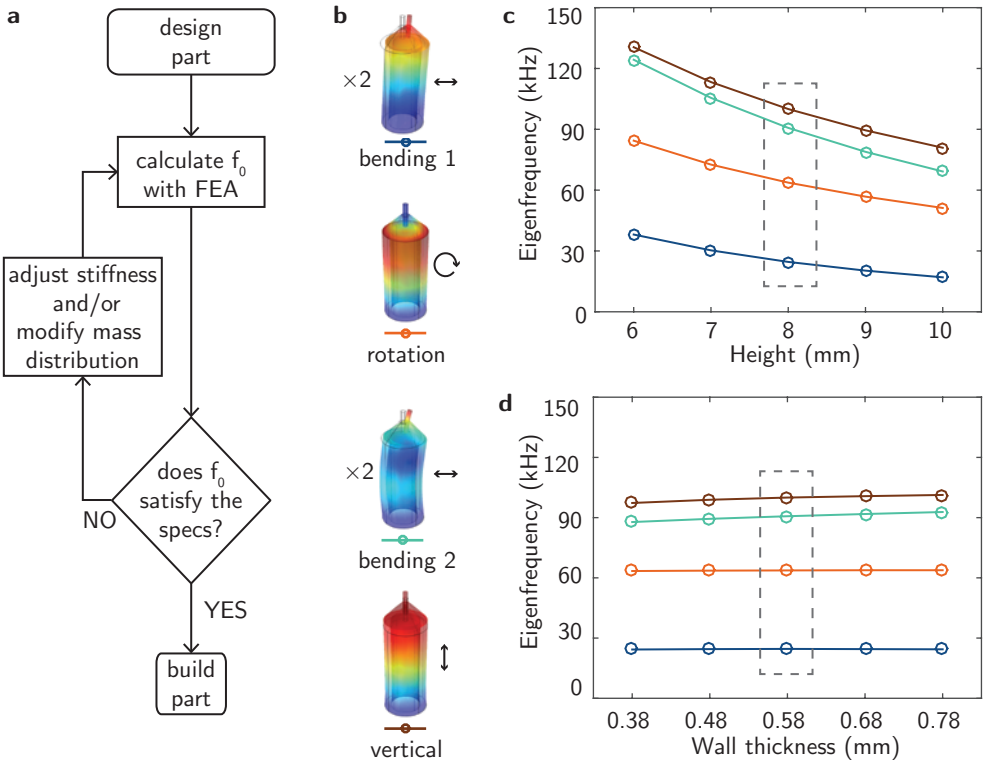

Figure 3.4: **a**, Flow chart explaining the procedure applied to several components of the STM head in order to achieve higher resonant frequencies. **b**, Mode shapes of the first six mechanical resonances of the piezotube as computed with Comsol, as a legend for panels **c**-**d**. The modes are shown as (exaggerated) displacements with colors from red (max displacement) to blue (no displacement). **c**, Variation of eigenfrequencies of the piezotube's modes with respect to the piezotube height, with base diameter fixed. **d**, Variation of eigenfrequencies of the piezotube's modes with respect to the wall thickness (with fixed outer diameter D=3.68 mm). The dashed boxes indicate the eigenfrequencies for the final chosen dimensions.

progressively change the dimensions of the part and recompute the eigenfrequencies, in order to understand which dimensions can be optimized to increase the stability. We find that is beneficial to lower the height (Fig. 3.4c), while changing the wall thickness (with fixed outer diameter) does not have a significant effect (Fig. 3.4d). In the case of a simple tube, this problem could also be solved analytically; however, here we want to show the procedure that then we will apply to more complicated parts of the STM head. In general, the optimization towards higher resonant frequencies can be limited by functional requirements and geometrical constraints. For the piezotube, reducing the aspect ratio between height and diameter diminishes the XY scanning

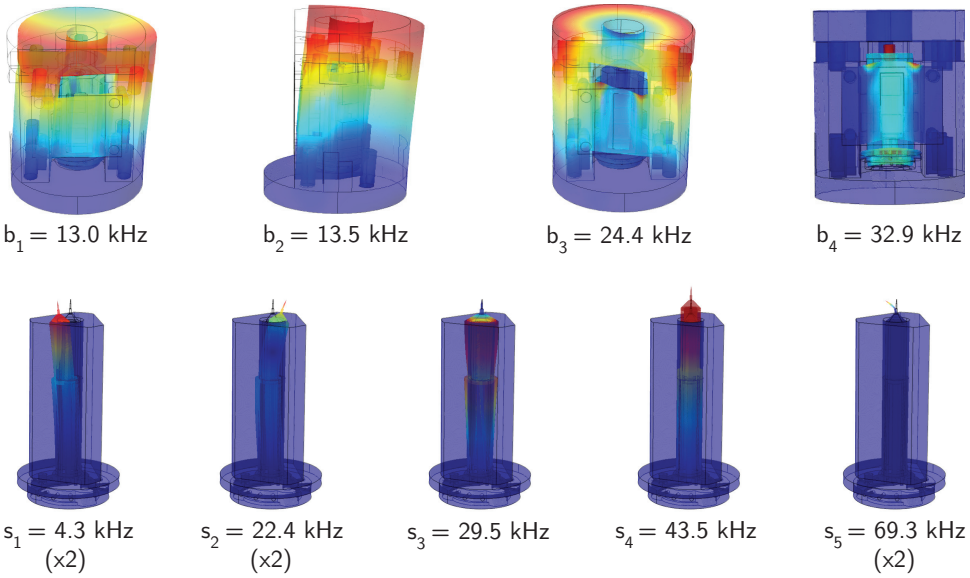

Figure 3.5: Main vibrational modes of the STM head, as calculated with Comsol, with the base of the STM fixed. The modes are shown as (exaggerated) displacements with colors from red (max displacement) to blue (no displacement). All the modes shown are calculated for the full design, but to ease visualization, the modes that belong to the scanner assembly (s_1-s_5) are shown separately. See the main text, Sec. 3.2.2, for a description of the modes.

range, and our final design is chosen as a compromise between stability and desired XY scanning range of $\approx 400\,\text{nm}$ at 4 K.

A similar analysis is performed on other STM head components, including the sapphire slider, the STM body, the Macor front piece and the sample holder. For instance, the simulations indicate that to reach a higher f_0, the STM head will benefit from a lower aspect ratio, a shorter and lighter sapphire slider and a lighter Macor front piece. The simulations also help determining until which point removing mass, for instance by drilling holes in the Macor front piece or in the sample holder, would help and when instead it would start hinder the stiffness of the part.

Finally, we also performed FEA calculations on the whole assembly of the STM head, simplified by removing small details in the design to allow for a simpler finite element mesh. This can provide further insights about the design choices, and moreover it can be directly compared to the measured values of the eigenfrequencies. The most significant modes that we obtain from FEA calculations of the full STM head are shown in Fig. 3.5. They can be divided in two groups: the modes belonging to the body of the STM ($b-$modes in Fig. 3.5) and the modes belonging to the scanner assembly ($s-$modes). The modes b_1, b_2 are almost degenerate and correspond to the

bending modes of the full head, b_3 corresponds to the rotational mode and b_4 to the motion of the slider inside the head. The modes s_1 and s_2 are double degenerate and correspond to first order and second order bending mode of the scanner, s_3 is the rotational mode of the scanner, s_4 the vertical mode of the scanner and s_5 is the bending mode of the tip.

Intuitively, one could think that the walker assembly used for coarse approach is the weakest point of the STM head design, and therefore that the lowest vibrational mode should correspond to the vertical motion of the slider inside the scanner (b_4). In our simulations, however, the main body vibrational modes and the scanner bending modes have lower frequencies, showing that the limiting factor for f_0 is mainly the STM head geometry. Clearly, the calculated value of the mode b_4 depends strongly on the stiffness of the shear piezo stacks that we feed into the simulation. The value of b_4 shown in Fig. 3.5 is obtained with half the stiffness reported in the specifications, to take into account the effect of glue and other factors involved in the mounting. Furthermore, the measured resonant frequencies reported in section 3.2.3 confirm that the slider construction is not the weakest point of the design.

3.2.3 Measurement of resonant frequencies

After the construction of the STM head, we measure both the eigenfrequencies of the walker assembly and of the piezotube assembly independently and we compare them with the calculations. The measurement is performed *in situ* with the head mounted in the cryogenic insert at room temperature and under vacuum. A lock-in amplifier is used to excite the piezo elements and to read out their response. The applied excitation is a sinusoidal signal of amplitude $1\,V_{\mathrm{peak-peak}}$ and sweeping frequency. A scheme of the circuit is presented in the inset of Fig. 3.6a [65]. Thanks to the intrinsic properties of piezoelectric materials, the electrical excitations V_{in} provided by the lock-in is converted into a mechanical excitation. When the excitation frequency corresponds to one of the STM eigenfrequencies, its amplitude gets enhanced, resulting in an enhanced electrical signal from the piezos V_{out} that is detected by the lock-in [65, 66].

Figure 3.6a-b show the transfer function obtained when exciting the six shear piezo stacks for the coarse approach connected in parallel. The main result is that we do not observe any resonant mode of the coarse approach assembly before 10 kHz, with the first strong peaks appearing at ≈13 kHz. We also performed the measurement at 4 K (not reported here), leading to slightly higher resonance frequencies due to the different stiffness of the materials at low temperatures and to thermal contractions. Remarkably, the value we achieve is a factor three better than the previously reported eigenfrequencies for a sapphire STM head [52], where the first strong peak in the coarse approach excitation appears at 4.6 kHz.

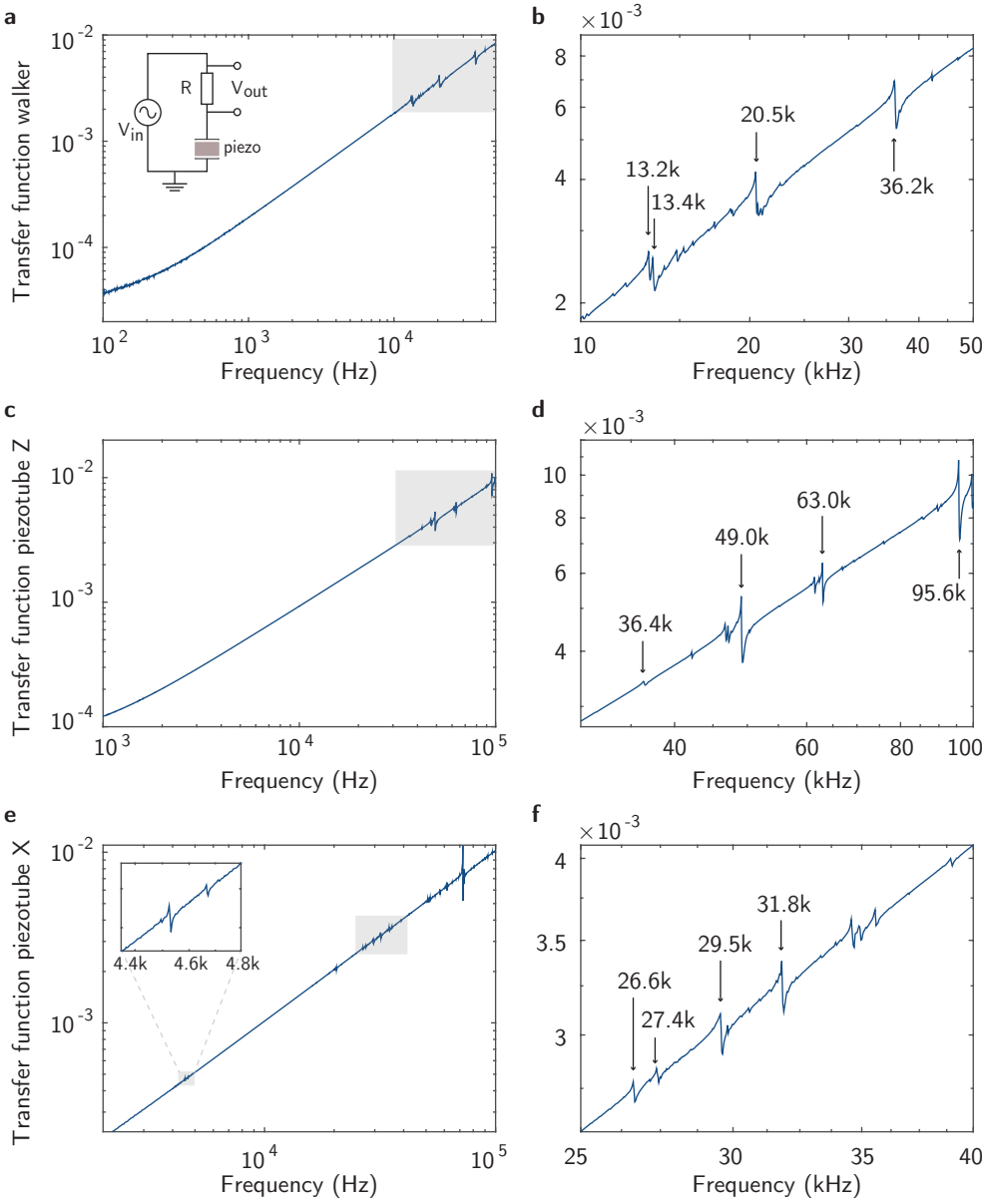

Figure 3.6: **a**, Measured transfer function V_{out}/V_{in} of the walker mechanism for the coarse approach. A scheme of the electronic circuit is shown in the inset, where R=11 Ω. **b**, Zoom of the gray area in **a**. **c**, Measured transfer function V_{out}/V_{in} of the piezotube vertical excitation. **d**, Zoom of the gray area in **c**. **e**, Measured transfer function V_{out}/V_{in} of the piezotube horizontal bending excitation. In the inset, a zoom of the low frequency peaks. **f**, Zoom of the gray area in **e**.

Additionally, we can now compare the measured resonances with the computed ones. We can easily identify the first two almost degenerate peaks at 13.2 kHz and 13.4 kHz as the two bending modes of the STM body (b_1, b_2). The peak at 20.5 kHz is more difficult to identify, but it could correspond to the rotational mode b_3. We interpret the peak measured at 36.2 kHz as the mode b_4, given that in the FEA calculations b_4 is the only mode we find in the frequency window between 30 kHz and 50 kHz, and in the measurement we do not observe any other peak before ≈80 kHz.

For the piezotube, we can measure the transfer function while exciting either the vertical modes (which are the most crucial ones) or the bending modes (which have less influence on the noise), simply by applying the excitation to different electrodes. In Fig. 3.6c-d we show the transfer function of the vertical modes, measured with the outer electrical contacts (±X,±Y) connected in parallel against the inner contact (Z) acting as ground. The small peak at 36.4 kHz results from coupling to the mode b_4, and the peak at 49.5 kHz can be identified as the vertical mode s_4 of the full scanner assembly. The peaks at 63.0 kHz and at 95.6 kHz are more difficult to identify, but could correspond to the rotational and vertical mode of the piezotube alone, that the calculations give respectively at 63.7 kHz and 100.0 kHz (from Fig. 3.4). In Fig. 3.6e-f we show the transfer function of the bending modes, measured between +X and -X contacts. The two very small peaks measured at 4.53 kHz and 4.66 kHz correspond to the first order bending modes of the piezotube s_1. The peaks at 26.6 kHz and 27.4 kHz could correspond to the second order bending modes s_2, and the peak at 29.5 kHz to the rotational mode s_3. We do not find correspondence to the calculations for the other small peaks, and the strong peak at 72.1 kHz could correspond to the bending mode of the tip s_5, even if we are doubtful that this could lead to such a sizable response of the piezotube.

The lowest resonant frequencies of the STM head thus correspond to the bending modes of the piezotube and of the STM head, which are substantially less critical for STM measurements than the vertical modes. The walker assembly, often a critical point for the vertical stability, proves to be the stiffest reported to date for a Pan-style head. Taken together, this confirms the exceptional stiffness of our STM head.

3.3 Cryogenic insert

The STM head is mounted at the bottom of a home-built cryogenic insert that operates at the base temperature of 4.27 K. The insert is rigidly connected to the UHV chamber and the table and it is placed in a ^{4}He bath cryostat. The cryostat has a capacity of 65L, which yields a hold time of ≈275 hours (≈11 days).

A picture of the cryogenic insert with the indication of the main parts is shown in Fig. 3.7. The bottom part of the insert, where the STM is rigidly connected without

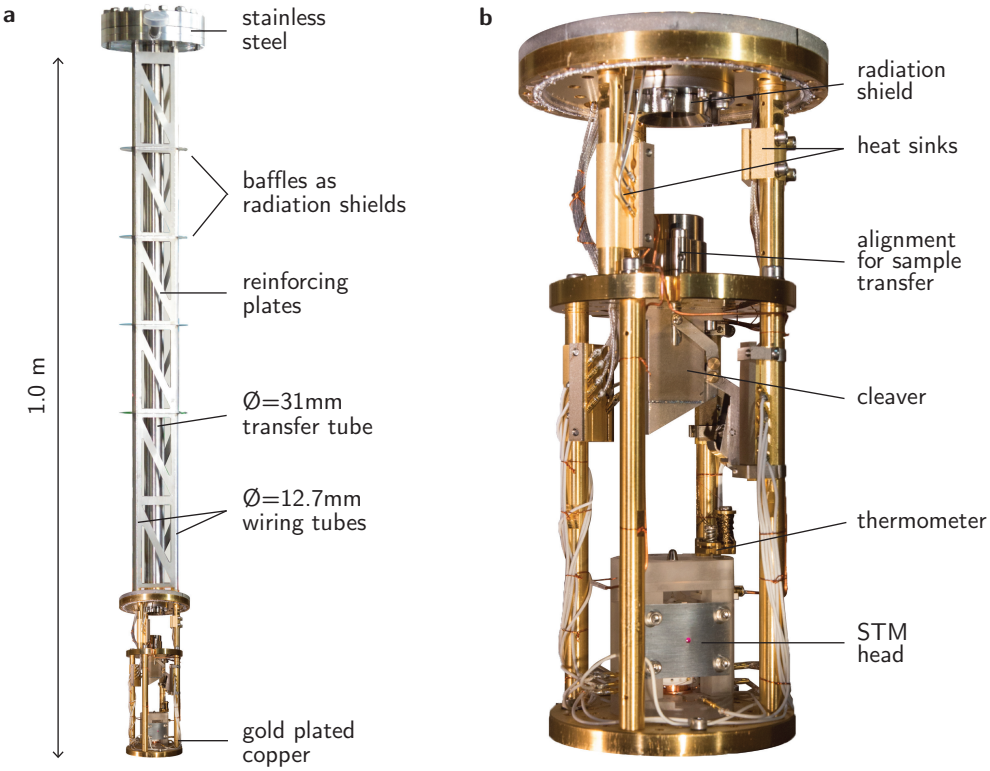

Figure 3.7: **a**, Photograph of the full cryogenic insert without the can that closes the bottom part. **b**, Zoom of the bottom part where the STM is mounted.

the use of springs, is made of gold-plated oxygen-free copper to optimize the thermal connection to the ^{4}He bath. It is enclosed in a gold-plated copper can (not shown in the picture), sealed with an indium wire gasket. The connection to the room temperature UHV chamber is made of thin-walled stainless steel tubes, that are used for pumping and wiring.

The design of the cryogenic insert has also been optimized for maximum stiffness. For this reason, we opted for a reinforced insert structure that features four stainless steel tubes. The central tube has an outer diameter of 31.0 mm and wall thickness of 0.5 mm and it is used as sample transfer line and main pumping line. The three smaller tubes (of outer diameter 12.7 mm and wall thickness 0.25 mm) are used for wiring and are placed in a triangular pattern around the central one. We find that choosing three tubes for wiring, instead of two, drastically improves the stability for the pendulum mode, with the resonant frequency corresponding to this mode increasing by 50%. Furthermore, we provide additional stability by connecting the

tubes with thin (0.3 mm) stainless steel plates. These plates have triangular holes in order to reduce the heat transfer from room temperature to the ^{4}He bath, and are laser spot welded directly to the tubes. Around the tubes, and perpendicular to them, we place four stainless steel baffles that act as radiation shields inside the dewar neck, to reduce the radiation heat transfer to the ^{4}He bath.

All the extra features that we added to improve the stability imply a higher heat conduction to the ^{4}He bath, and a compromise has to be found between stability and desired helium consumption. With our particular design we still obtain an excellent helium consumption of 0.18 L/h (4.3 L/day), which ensures a very quiet helium boil-off noise and allows for >7 days long measurements.

The bottom part of the insert is provided with a radiation shield and a sample cleaving stage. The radiation shield can be placed with the sample transfer mechanism and it significantly reduces by 0.3 K the temperature measured on the STM head. The cleaver is also actuated by the sample transfer mechanism, and it has a bucket that collects the cleaved rods. Before cleaving, the samples are thermalized for a few minutes on the 4 K plate, and we estimate that the cleaving temperature is ≈ 20 K.

3.4 Vibration isolation table

The vibration isolation table is made of two parts: a rigid stainless steel hollow frame with triangular shape and a 40-mm-thick triangular aluminum plate. The plate is rigidly connected to the frame by screws, and the assembly is designed with the specifications of not having any resonant frequencies below 300 Hz. The frame is mounted on top of three negative spring coefficient vibration isolators[6] with resonant frequency 0.5 Hz. In order to reduce acoustic-induced noise and to increase the mass of the table, the frame is filled with lead shots to reach a weight of the total system of ~ 1000 kg. The full system is standing on a measurement island that is decoupled from the surrounding walking floor, but is not additionally isolated with dampers from the foundations.

3.5 UHV chamber

The fully home-built UHV chamber comprises a small load lock chamber and a main preparation chamber. A turbo pump, which is switched off during measurements, is connected to the load lock, and an ion getter pump is installed on the main chamber, leading to a base pressure of $p = 3 \times 10^{-10}$ mbar. Sample storage space and manipu-

[6] Minus K® 800CM-1.

lators are provided in both chambers. In the main chamber, we installed an ion gun for Ar sputtering and a home-built sample heater.

3.6 Performance

We test the performance of our microscope by measuring vibrational noise spectra at the tunnel junction and by obtaining topographic and spectroscopic data on the correlated metal Sr_2RhO_4. Here, we briefly show the data to demonstrate the performance of the microscope, while the physics of Sr_2RhO_4 is discussed in the dedicated chapter 6.

3.6.1 Current and height noise at the tunneling junction

We first characterize the noise level of our laboratory by measuring both vibrations with a seismometer[7] and acoustic noise with a low-frequency microphone[8]. The measurement is reported as linear spectral density (LSD) of the velocity for the vibrations and of the pressure difference for the acoustics. The spectra are obtained by Fourier transforming one minute of real time data with the Welch method using a Hamming window.

We report in Fig. 3.8a typical spectra of (i) the vibrations measured on the island where the table is standing, (ii) the vibrations measured on the table, (iii) the sound measured in the surrounding room. The table reduces the general vibrational noise of about one order of magnitude after 10 Hz, and it dampens many of the peaks. It is instead less effective in reducing the sound-induced noise, as it can be noticed from the peak at 24 Hz that is only partially dampened.

In Fig. 3.8b we show the vibrational noise at the tunnel junction as the linear spectral density of the z height (corresponding to the tip-sample distance) measured in feedback on a $(Pb,Bi)_2Sr_2CuO_{6+x}$ sample at setup condition $V = 300\,mV$ and $I = 150\,pA$. Remarkably, the noise is very low, with an average vibration level of $\approx 6\,fm/\sqrt{Hz}$ and only two peaks with amplitude bigger than $20\,fm/\sqrt{Hz}$, respectively at 12 Hz and 50 Hz.

In Fig. 3.8c we further show the linear spectral density of the current noise measured with the same tunneling junction and setup condition. With tip retracted, we achieve an average noise level of $\approx 8\,fA/\sqrt{Hz}$. The preamplifier we use[9] has a noise floor of $6.5\,fA/\sqrt{Hz}$.

[7] Guralp CMG-40T.
[8] G.R.A.S. 46AF.
[9] FEMTO LCA-4K-1G.

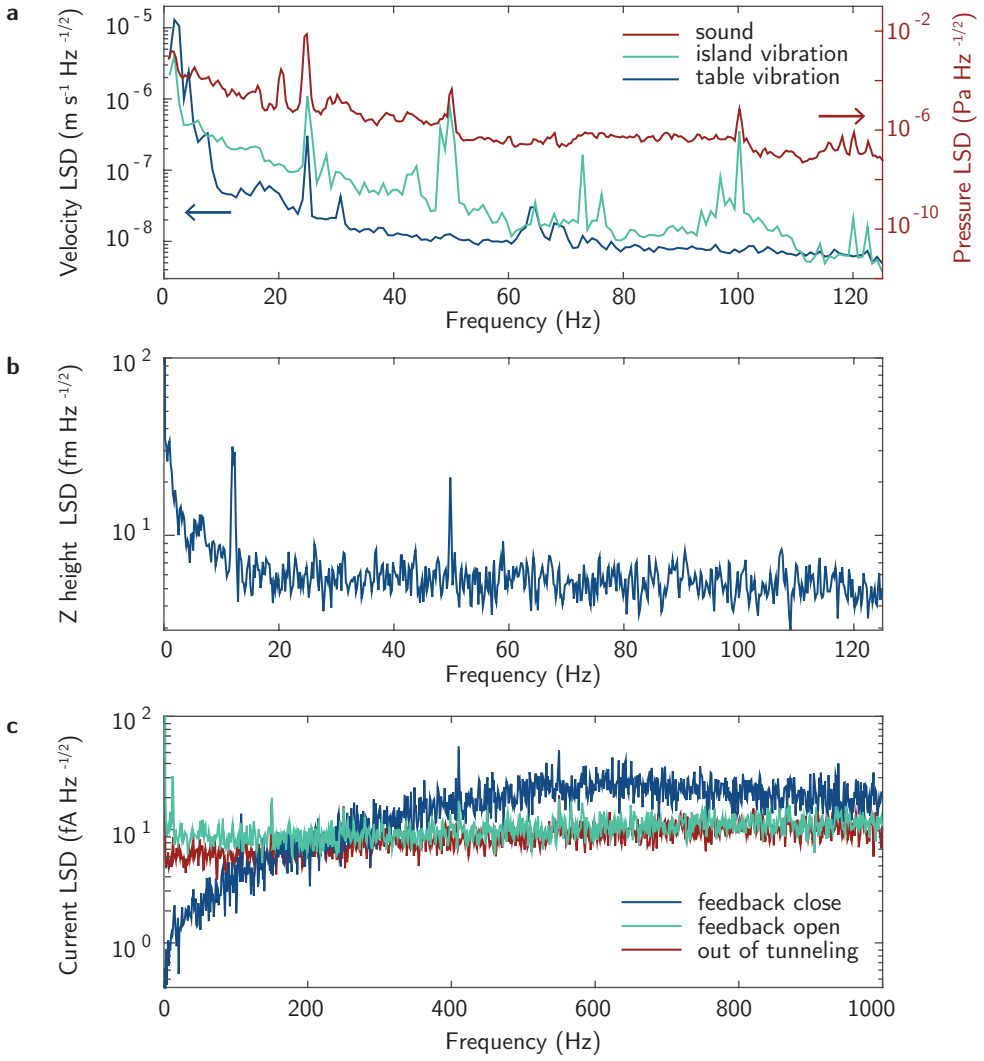

Figure 3.8: **a**, Linear spectral density (LSD) of the velocity measured in the Z direction on the island and on the STM table with a seismometer (Guralp CMG-40T). In the same graph, with scale on the right axis, acoustic noise is reported as LSD of the pressure difference measured with a low-frequency microphone (G.R.A.S. 46AF). **b**, Linear spectral density of the Z height noise at the tunnel junction measured on $(Pb,Bi)_2Sr_2CuO_{6+x}$ at setup condition $V = 300\,mV$ and $I = 150\,pA$. **c**, Linear spectral density of the tunneling current at same tunnel junction as **b**, measured out of tunneling as well as in tunneling with feedback loop closed and open.

In tunneling and with feedback loop closed we can see an increase in the noise to $\approx 20\,\mathrm{fA}/\sqrt{\mathrm{Hz}}$ above 200 Hz, with some peaks reaching up to $\approx 50\,\mathrm{fA}/\sqrt{\mathrm{Hz}}$. The feedback takes care of reducing the low frequency noise.

An important figure of merit for spectroscopic measurements is the out-of-feedback current noise (in tunneling and with feedback loop open). We obtain a noise level of $\approx 10\,\mathrm{fA}/\sqrt{\mathrm{Hz}}$, with only the peaks at 12 Hz and 50 Hz higher than $20\,\mathrm{fA}/\sqrt{\mathrm{Hz}}$, which ensures the capability of performing high quality spectroscopy experiments.

3.6.2 Quasiparticle interference on Sr_2RhO_4

To demonstrate the topographic and spectroscopic capabilities of the microscope, we show quasiparticle interference measurements on the correlated metal Sr_2RhO_4, that is known to have a highly two-dimensional electronic structure [68–70].

The sample is cleaved at the 4 K cleaving stage and immediately transferred to the STM head. Measurements are performed with a chemically etched tungsten tip that has previously been prepared by field emission on a gold surface. Atomic resolution can be easily achieved, as shown in the $15 \times 15\,\mathrm{nm}^2$ topograph in Fig. 3.9a and in the corrugation profile along the black line plotted in Fig. 3.9b. The cleaved surface shows the SrO layer; the Sr atoms are visible on the surface, with interatomic distance distance $a = 3.85\,\text{Å}$. Moreover, we can observe two different types of defects.

In Fig. 3.9c we plot a typical single $\mathrm{d}I/\mathrm{d}V$ spectrum acquired during a spectroscopic map. The spectrum is metallic, and does not show sharp features.

In Fig. 3.9d we show the real space imaging of quasiparticle interference (QPI) in the conductance layer at -20 meV (with respect to the Fermi level), acquired simultaneously to the topograph in Fig. 3.9a. The defects obviously act as scattering centers for the quasiparticles, creating an interference pattern between the standing waves that emphasizes the quantum mechanical wave nature of the quasiparticles.

In Fig. 3.9e we show the Fourier transform of the real-space QPI pattern measured at the Fermi level during a spectroscopic map. The map is acquired on a field of view of $55 \times 55\,\mathrm{nm}^2$ with 288×288 pixels, thus consists of ≈80000 spectra acquired one after the other without the use of feedback to the tip during the spectra acquisition. The Fourier-transformed data is not symmetrized nor processed in any other way, and still shows sharp features with very high signal-to-noise ratio.

A more comprehensive analysis, including a quantitative comparison with ARPES data from Ref. [69], will be discussed in chapter 6.

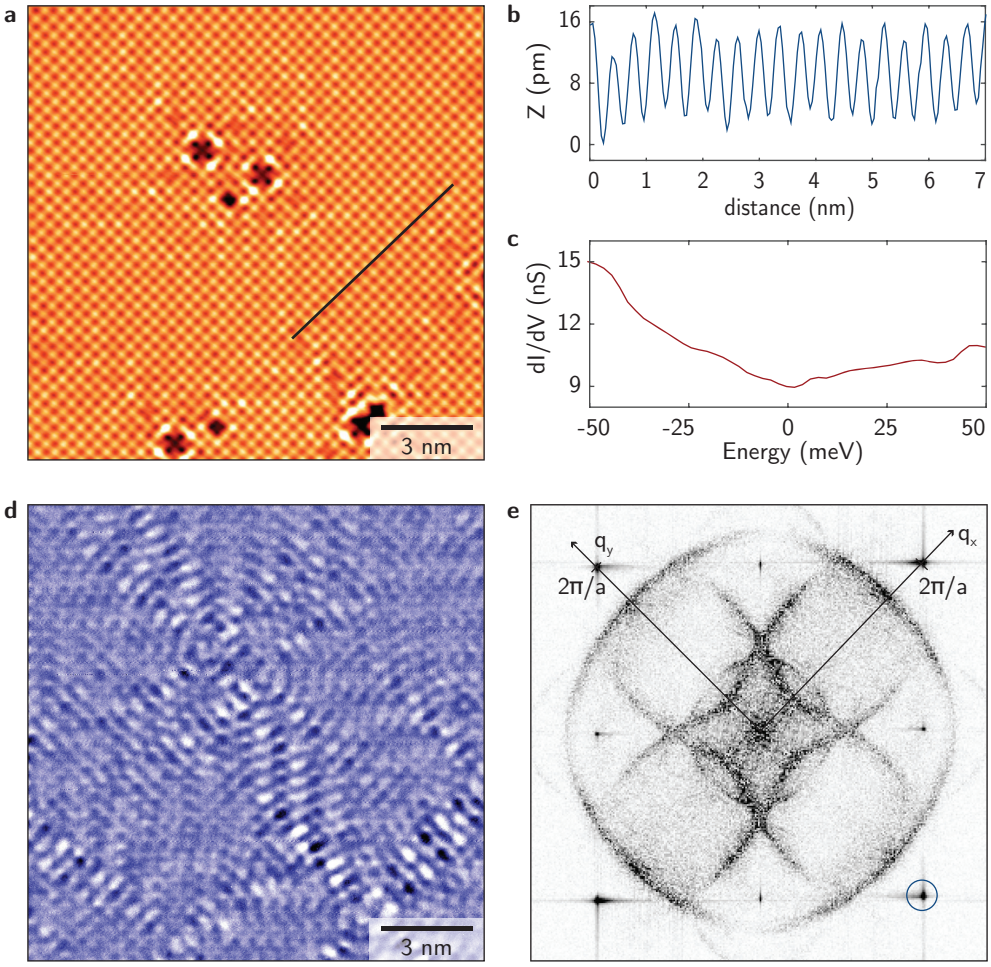

Figure 3.9: STM measurements on Sr_2RhO_4. **a**, Topograph in a field of view of $15\times15\,nm^2$. Setup conditions ($V_b=-20\,mV$, $I_t=600\,pA$). The image is not filtered. **b**, Atomic corrugation profile along the black line in **a**. **c**, Example of a single dI/dV spectrum measured during a spectroscopic map. **d**, Density of states measured simultaneously to the topograph in panel **a**, showing the quasiparticle interference pattern in real space at energy $E=-20\,meV$. **e**, Non-symmetrized Fourier transform of the conductance layer at the Fermi level acquired in a spectroscopic map over a $55\times55\,nm^2$ field of view. One of the Bragg peaks is highlighted in the blue circle.

3.7 Conclusions

In the present chapter, we describe design principles, construction and performance of our ultra-stable STM Dome. We constructed a very stiff microscope by combining smart material choice and design improvement guided by FEA calculations. This allows us to obtain outperforming data quality even in a lab not dedicated to low vibrations, as described in Sec. 3.6. While writing this thesis, the instrument has been moved to a new building with world-class low-vibration facilities, and we believe that this will improve its performance further. In chapter 7, we propose a series of experiments that we are planning to perform with the microscope Dome in the near future.

4

Universality of pseudogap and emergent order in lightly doped Mott insulators

This chapter has been published as:
Battisti *et al.*, Nat. Phys. **13**, 21 (2017).

4.1 Introduction

Mott insulators are one of the most iconic examples of correlated electron systems. In these materials, electrons are localized due to strong electron-electron interactions, and they can be thought of as frozen at the location of their atomic core (see Sec. 1.2). A core mystery of condensed-matter physics is how this rigid arrangement of electrons loosens when inserting extra carriers (doping). The strong electron correlations that characterize the Mott insulating state, in fact, are thought to be responsible for the remarkably complex, emerging behaviors that are observed upon doping [6, 9, 11].

A prime example are cuprates, copper-oxide based compounds (see Sec. 1.2 for a brief overview). Upon adding extra carriers to the Mott insulating parent compound, cuprates show, at low doping levels, the formation of a pseudogap and a variety of inhomogeneous electronic orders, and, at higher doping, high-T_c superconductivity [11]. These phenomena have often been assumed (though not verified), to not be limited to the CuO_2 planes, but common to spin-$\frac{1}{2}$ Mott physics.

Here, we study the iridate Sr_2IrO_4, a compound that is chemically radically different from cuprates, but also an effective spin-$\frac{1}{2}$ quasi two-dimensional Mott insulator. We show that, upon electron doping, a spatially inhomogeneous pseudogap as well as a local glassy charge order exists in this compound as well, revealing an universality of these emergent phenomena. Moreover, we are able to precisely elucidate how the insertion of extra carriers causes the transition from Mott to pseudogap phase.

We start with an introduction to the properties of Sr_2IrO_4 and an overview of the relevant literature (Sec. 4.2 and 4.3). We then show our STM results on the electron-doped compound $(Sr_{1-x}La_x)_2IrO_4$, at doping levels $0 \leq x \leq 5.5\,\%$. We find two distinct electronic behaviors, one at low doping levels, $x \leq 4\%$ (Sec. 4.5), and one at higher doping levels, $x \approx 5\%$ (Sec. 4.6). In section 4.7, we illustrate the melting of the Mott state with doping, and we propose a theoretical interpretation of our data.

4.2 The electron-doped iridate $(Sr_{1-x}La_x)_2IrO_4$

The parent compound Sr_2IrO_4 is a quasi two-dimensional material, isostructural to the cuprate La_2CuO_4. It has a perovskite crystal structure with alternating IrO_2 and SrO planes, such that oxygen octahedra form around each iridium atom. The IrO_6 octahedra additionally undergo an in-plane rotation of 11° (Fig. 4.1a).

Each iridium atom has five $5d$ electrons ($5d^5$), in contrast to the cuprates, where each copper atom has nine $3d$ electrons ($3d^9$). As introduced in chapter 1, the orbitals of $5d$ transition metal atoms are more spatially extended than those of $3d$ transition metals, causing larger bandwidths and higher hopping energy t. Moreover, the

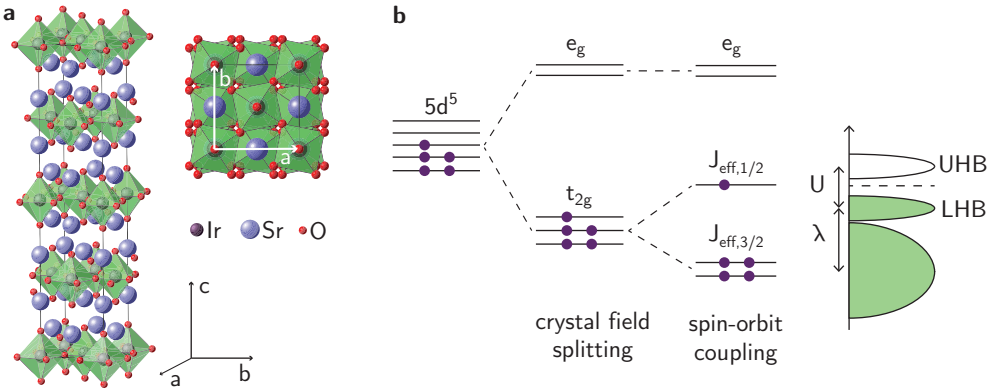

Figure 4.1: **a**, Crystal structure of Sr_2IrO_4. **b**, Effect of crystal field and spin-orbit coupling on the 5d band of Sr_2IrO_4. The Coulomb repulsion U splits the resulting $J_{eff} = 1/2$ band into a lower and upper Hubbard band (LHB and UHB, respectively) [71].

electron-electron correlations caused by the Coulomb repulsion U are reduced due to higher screening compared to $3d$ elements (for $3d$ materials the electron correlation magnitude is $U \approx 5\,\text{eV}$, for $5d$ materials typically $U \approx 0.5\,\text{eV}$). Despite the weaker electron-electron correlation U which is not able to open a Mott gap in the spatially extended $5d$ states, Sr_2IrO_4 is found to be an effective spin-$\frac{1}{2}$ Mott insulator [71, 72]. This can be explained by the fact that $5d$ atoms are heavier and therefore have a stronger spin-orbit coupling: while in cuprates spin-orbit coupling is typically negligible, in the iridates it acquires energies comparable to the electron-electron correlations.

Fig. 4.1b illustrates how this affects the electronic structure. The $5d$ states are first split by the crystal field into three t_{2g} states and two e_g states, analogous to cuprates. The crystal field energy is large enough that the five electrons prefer a low spin state and occupy only the t_{2g} states. At this point, the moderate electron correlations U are not able to open a Mott gap within the t_{2g} band. However, the strong spin-orbit coupling splits the t_{2g} band to form a filled $J_{eff} = \frac{3}{2}$ band and a half-filled $J_{eff} = \frac{1}{2}$ band. The moderate on-site Coulomb repulsion U is now strong enough to open a Mott gap in the $J_{eff} = \frac{1}{2}$ band, making Sr_2IrO_4 an effective spin-$\frac{1}{2}$ Mott insulator [71, 72].

Theoretical calculations, including LDA[1]+SO+U [71, 73], variational Monte Carlo studies [74] and LDA+DMFT[2] [75] confirm this scenario.

Experimentally, the parent compound Sr_2IrO_4 has been probed by several techniques. Optical conductivity measurements [71, 73, 76] show a Mott gap value of $\approx 500\,\text{meV}$,

[1] LDA: local-density approximation.
[2] DMFT: dynamical mean-field theory.

in good agreement with calculations [77]. Angle-resolved photoemission spectroscopy (ARPES) shows that the Mott gap is asymmetric around the Fermi level, with the upper edge of the lower Hubbard band between -200 meV and -100 meV [71, 78–80]. Resonant (inelastic) x-ray scattering (REXS - RIXS) shows antiferromagnetic ordering typical of the Mott state, with the magnetic moments $J_{eff} = \frac{1}{2}$ lying in the IrO_2 plane, and additionally canted due to the rotation of the ochtaedra [81]. The spin excitations as measured with RIXS have energies comparable to the ones of the cuprates [82], and REXS data has revealed the presence of an incommensurate magnetic state reminiscent of the diagonal spin density wave state observed in the cuprate $(La_{1-x}Sr_x)_2CuO_4$ [83].

Given the insulating behavior of the material at low temperatures, pioneering STM measurements are reported for the parent compound only at 77 K [84–86], each of them showing different Mott gap values. Accidental doping was reported in one study [84], indicating a possible cause of the different values.

Despite the very different chemical make-up, the similarity of Sr_2IrO_4 to the parent compound of cuprate superconductors is striking. It thus seems straightforward to expect that doping the material with holes or electrons will display the same mysterious phases that emerge upon doping cuprates. Indeed, theoretical studies predict that the material should become superconducting upon electron doping [87, 88].

Electron-doped samples have been created by depleting oxygen [89] or substituting La at the Sr sites in bulk crystals [79, 80, 90–92] and by surface doping through *in situ* deposition of alkali-metal atoms [93, 94]. Hole-doped samples have been made by substituting Rh at the Ir sites [80, 90]. In all cases, doping quickly suppresses magnetism and affects transport results. Moreover, there is consensus about the appearance of a pseudogap [79, 92, 93] and of a low-temperature *d*-wave gap [94, 95] upon electron doping. Unfortunately, superconductivity has not been achieved to date, possibly because samples with sufficiently high doping levels could not be created.

4.3 Sample characterization

We think that the most reliable way to dope Sr_2IrO_4 with extra electrons is by La substitution on the Sr sites, because this method produces the cleanest crystals. Therefore, the results presented in this chapter are measured on single crystal $(Sr_{1-x}La_x)_2IrO_4$ samples, spanning the doping range $0 \leq x \leq 5.5\,\%$. The samples are grown and pre-characterized by our collaborators from University College London and University of Geneva, who performed ARPES experiments on samples from the same batch [79]. The single crystals are flux grown from a mixture of off-stoichiometric quantities of IrO_2, La_2O_3 and $SrCO_3$ in an anhydrous $SrCl_2$ flux. The mixture is

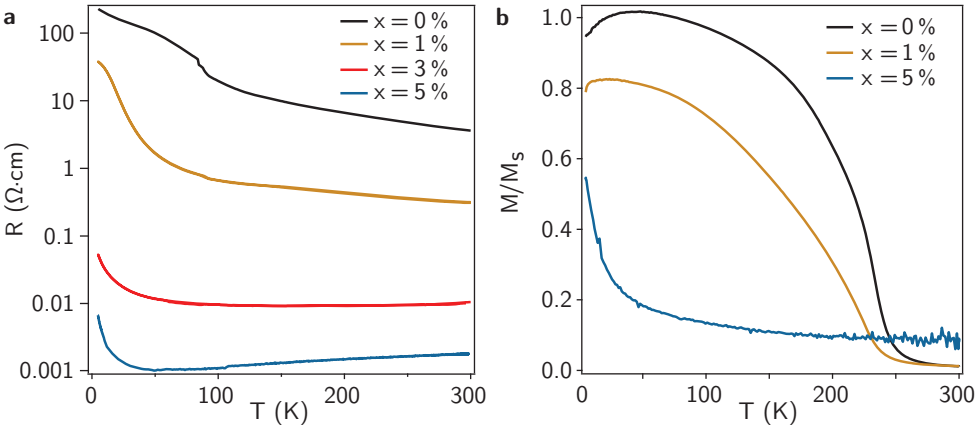

Figure 4.2: **a**, Evolution of the resistivity with doping. **b**, Evolution of the magnetic behavior with doping. The magnetization curves are taken with an applied magnetic field of $H = 1\,T$ after zero-field cooling and are normalized by the magnetic moment at $H = 2\,T$, which for the magnetic samples corresponds to the saturation field. Reproduced from Ref. [79].

heated to 1245 °C for 12 h and cooled at a rate of $8\,°C\,h^{-1}$ to 1100 °C before quenching to room temperature. The resulting crystals are mechanically separated from the flux by washing with water, and range between 200 µm and 600 µm in size.

Transport measurements of the *ab*-plane resistivity at different doping concentrations x (as determined by EDX[3]) are shown in Fig. 4.2a. For the highest doping level, the resistivity shows metallic behavior down to 50 K followed by an upturn at lower temperature. The upturn is reported from several groups [80, 91, 92, 96], and is reminiscent of low-doped cuprates [97]. Figure 4.2b shows the doping evolution of the magnetic behavior. The magnetic order persists for $x = 1\%$, but with decreased Neel temperature; the highest doping samples are paramagnetic, indicating suppression of the Mott antiferromagnetic state.

These bulk transport measurements probe the properties of the material between two macroscopically spaced electrodes (in this case, applied on two sides of the crystal). If the material is electronically inhomogeneous, transport will average the electronic properties and the interpretation of its results becomes more complicated. Importantly, we know from our STM measurements and from subsequent near-field optical microscopy measurements [96] that the doping concentration is not homogeneous within one $(Sr_{1-x}La_x)_2IrO_4$ sample. In samples with doping $x = 5\%$ determined by EDX, we find with STM areas where the local doping changes from $x = 2\%$ to $x = 5\%$ on a length-scale of $\approx 100\,\mu m$. In order to obtain more reliable results with easier interpretation, one should measure transport from areas where the doping is

[3] energy dispersive X-ray spectroscopy.

homogeneous, for example by using electron-beam lithography or focused-ion beam (FIB) to reduce the size of the crystals before measuring transport.

4.4 Doping level determination with STM

The STM experiments reported in this chapter are performed with a low-temperature (2 K), ultrahigh vacuum commercial STM[4]. The iridate crystals are cleaved *in situ* at a temperature of 20 K and a pressure of 2×10^{-10} mbar, and then transferred immediately into the STM sample stage. Importantly, we found that cleaving at a higher temperature deteriorates the quality of the surface. The STM topographs are taken in the constant current mode, and the $\mathrm{d}I/\mathrm{d}V$ spectra are collected using a standard lock-in technique with a modulation frequency of 857 Hz. We use mechanically ground PtIr tips that are tested on a crystalline Au(111) surface prepared *in situ* by Ar ion sputtering and temperature annealing.

The iridate $(Sr_{1-x}La_x)_2IrO_4$ cleaves between the SrO layers, revealing an atomically flat SrO terminated surface. In Fig. 4.3, we show two topographs at different doping concentrations. The Sr atoms are easily resolved, and the lattice constant is $a_0 = 3.9$ Å. Since La dopants substitute for Sr atoms, they are visible on the surface, and they can be identified as dark atoms surrounded by a brighter square [98].

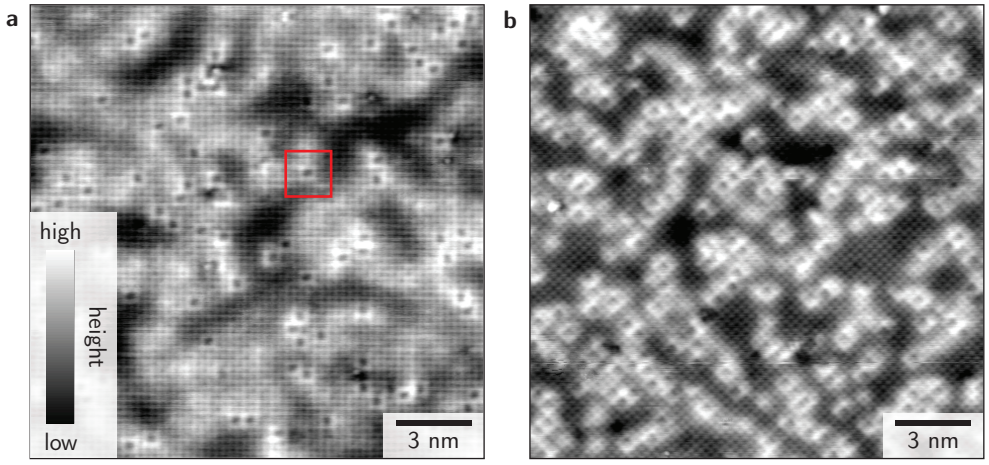

Figure 4.3: Examples of atomically resolved STM topographs measured on $(Sr_{1-x}La_x)_2IrO_4$ at different doping levels. The La^{3+} dopant atoms are readily identified as dark spots surrounded by brighter atoms (see, e.g., red square). **a**, Doping level 2.0%, field of view $18\times18\,\mathrm{nm}^2$, setup conditions ($V_b = -1.1$ V, $I_t = -200$ pA). **b**, Doping level 5.5%, field of view $18\times18\,\mathrm{nm}^2$, setup conditions ($V_b = -750$ mV, $I_t = -400$ pA).

[4]modified USM1500 from Unisoku.

The ability to easily identify the dopant positions with atomic precision (e.g. in contrast to the cuprates [17, 99]) is key to our investigation, as it allows us to precisely localize dopant atoms and investigate their effect on the electronic structure. As the doping inhomogeneities are large (see Sec. 4.3), it is important to determine the local doping level: with STM, we can simply do that by counting the La to Sr ratio within a given field of view.

We investigate surfaces with densely spaced local doping concentrations between 2.1 % and 5.5 %, where we estimate an error of ±0.7 % in the doping determination. We also attempt to measure an undoped sample, but even at 77 K the material is too insulating to allow STM experiments, and the tip crashes on the sample during the approach procedure. This is in contrast with previous measurements on the parent compound [84–86], which we interpret as a confirmation of the high purity of our samples.

In the available doping range, we find strikingly different spectroscopic properties that allow us to separate the doping levels into two main groups, one of *low doping*, where $x < 4\%$, and one of *high doping*, where $x \approx 5\%$.

4.5 Low doping levels: frozen Mott state

We find that very lightly doped samples with $x < 4\,\%$ are deep in the Mott phase. In all our measurements, these doping levels yield a clear Mott gap, as shown in Fig. 4.4 for a sample with $x = 2.2\,\%$. The shape of the gap is reminiscent of STM spectra of cuprate parent materials [100, 101].

To investigate how the Mott state reacts when dopant atoms are inserted, we acquire spectroscopic maps from which we extract Mott gap maps, i.e., the magnitude of the Mott gap as a function of location, $\Delta_{\mathrm{Mott}}(\mathbf{r})$. Figure 4.4a shows the result on a 2.2 % sample, where the La dopant positions are marked by green dots. The gap size is determined by fitting a phenomenological gap function consisting of two artificially broadened Fermi functions that have the gap energy as fitting parameter. We fit negative and positive sides separately.

The biggest variation in the Mott gap is highlighted in the inset of Fig. 4.4a, where the two spectra correspond to the average of all the spectra inside the white circles. The main difference is the small additional density of states around −0.8 eV. Importantly, La dopants do not significantly change the Mott gap size in their close vicinity. However, a long-wavelength arrangement of varying Mott gap is visible, and it is possibly induced by the presence of the dopants. We interpret these nanoscale arrangements as the first of a series of orders that will appear upon doping. The most surprising

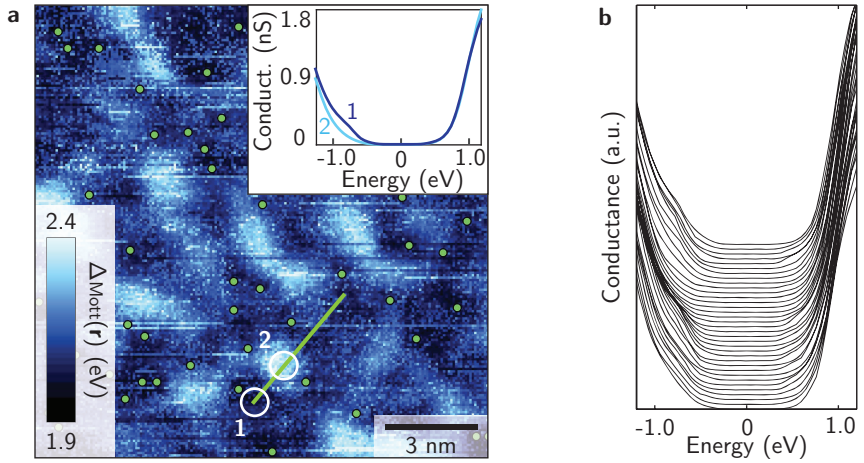

Figure 4.4: **a**, Mott gap map Δ_{Mott} of a sample with doping concentration $x = 2.2\,\%$. Position of dopant atoms are indicated by green circles. The inset shows local density of states spectra averaged inside the white circles. **b**, Local density of states spectra, each corresponding to a single measurement, along the green line in **a**, vertically offset for visual clarity.

observation is the total lack of in-gap states, despite the presence of dopants. We will discuss our interpretation of this fact in Sec. 4.7.

Another important observation regards the size of the gap: the magnitude of the Mott gap that we measure with STM on the lightly doped samples does not agree with what has been reported in literature by other techniques [71, 73, 77–79]. If we interpret the gap size as the energy range where the LDOS is zero, we measure a gap of $\approx 1\,\text{eV}$, which is very different from the 500 meV gap reported by optical spectroscopy and ARPES and predicted by theory [71, 73, 77–79].

This is caused by the phenomenon of tip-induced band bending (TIBB) that we introduced in Sec. 2.4. Due to the poor electronic screening in the material, the electric field generated by the tip can penetrate the sample, changing the potential landscape and strongly affecting the spectra measured with STM. In particular, TIBB can cause the gap measured with STM to be bigger than the intrinsic gap of the material.

In chapter 5, we show that this is exactly what happens in the lightly doped iridates, and we develop a model that is able to retrieve the intrinsic Mott gap from the apparent Mott gap measured by STM. Here, we just want to state that after applying our TIBB model to the data, we obtain an intrinsic gap value of $\approx 600\,\text{meV}$ for the low doping level samples, a value that roughly reconciles with literature.

4.6 High doping levels: pseudogap and electronic order

The pure Mott state described in section 4.5 is not sustained at higher doping levels $x \approx 5\%$. At this threshold, we find an abrupt transition to a strikingly inhomogeneous electronic structure, with a phase-separated Mott gap/pseudogap electronic landscape. Within the pseudogap regions, we additionally observe signatures of electronic order that are reminiscent of the order observed in the cuprates.

4.6.1 Phase separation

At doping levels of $x \approx 5\%$, the $\mathrm{d}I/\mathrm{d}V$ spectra drastically change[5]. In some regions we still measure a Mott gap, which now has the Fermi level pinned closer to the bottom of the upper Hubbard band (blue curve in Fig. 4.5a). This is in contrast to the low doping samples, and is to be expected for a Mott insulator doped with electrons. In other regions, we measure electronic states inside the Mott gap (red curve in Fig. 4.5a). Here, the spectra are remarkably similar to the pseudogap spectra in the cuprates [101, 102], with a gap value of 70 - 300 meV, in rough agreement with ARPES measurements [79, 93, 95]. In addition, some of the spectra show clear 'coherence peaks' (Fig. 4.5d).

In order to analyze how these two different types of spectra are spatially distributed within a field of view, we introduce a parameter that we call *Mott parameter*, $M(\mathbf{r})$. It is obtained by integrating the LDOS inside the Mott gap (red-shaded area in Fig 4.5b) and normalizing it by the integrated LDOS outside the gap (blue-shaded area in Fig 4.5b). In numbers,

$$M(\mathbf{r}) = \frac{\int_{-350\,\mathrm{meV}}^{+50\,\mathrm{meV}} \mathrm{LDOS}(E,\mathbf{r})\,\mathrm{d}E}{\int_{+200\,\mathrm{meV}}^{+500\,\mathrm{meV}} \mathrm{LDOS}(E,\mathbf{r})\,\mathrm{d}E}\,. \tag{4.1}$$

This parameter is large when there are states inside the gap, and small when the Mott gap is dominating. In Fig. 4.5c, we plot $M(\mathbf{r})$ as a function of the spatial coordinates for a spectroscopic map measured on a $x = 5.5\,\%$ surface, with the dopant atoms positions indicated by green dots. This allows us to quickly identify Mott areas (in blue) vs. pseudogap areas (in red).

The pseudogap areas, that we will, from now on, call *pseudogap puddles*, are not randomly distributed, but form around clusters of dopant atoms. We want to emphasize that pseudogap puddles are not observed in the low doping level samples, even if few dopants happen to be close together by chance: a certain threshold in the doping level is needed for the transition to occur. Moreover, the transition between the two

[5] This is also reported by Chen et al. [92].

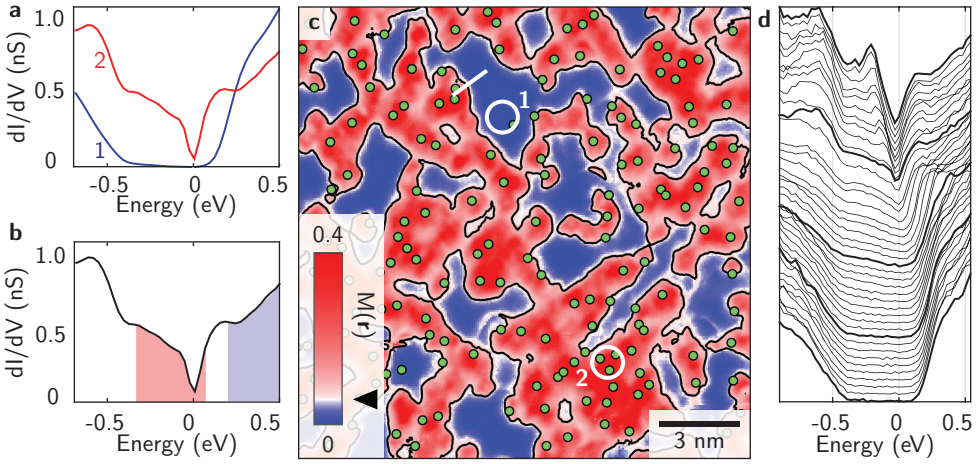

Figure 4.5: Phase separated Mott/pseudogap electronic structure at 5.5 % doping. **a**, Spectra from two different regions: Mott spectrum (blue), and mixed Mott/pseudogap spectrum (red). The spectra are the average of 180 spectra inside the white circles in panel **c**. **b**, Definition of the Mott parameter as the integrated LDOS inside the Mott gap (red) normalized by the one outside the gap (blue). **c**, The Mott parameter identifies pseudogap puddles (red) and pure Mott regions (blue). Green circles indicate the La dopant locations. The triangle on the colorbar indicates the value of the black contour. **d**, Local density of states spectra along the white line in **c** (whose length is 1.5 nm), vertically offset for clarity. Each spectrum corresponds to a single measurement.

regimes of different electronic behavior is well defined and sharp, in the sense that it occurs within less than a nanometer. We highlight the sharpness in Fig. 4.5d, where we show single spectra along the white line in Fig. 4.5c. This sharpness allows us to define a threshold between Mott and pseudogap regions (black contour in Fig. 4.5c), and to state that we observe an *electronic phase separation* at the nanoscales.

4.6.2 Mapping pseudogap and Mott gap

To further characterize the electronic structure, we develop a fitting procedure that is able to fit spectra both in the Mott regions and in the pseudogap puddles. We choose to use a largely phenomenological fitting function, given that the vast variety of the spectra complicates the development of a complete theory. It comprises a polynomial background that multiplies a phenomenological Mott gap summed with a phenomenological pseudogap (see Fig. 4.6a for a graphic representation):

$$\mathrm{LDOS}_{\mathrm{total}}(E) = \mathrm{LDOS}_{\mathrm{background}}(E) \cdot [\mathrm{LDOS}_{\mathrm{Mott}}(E) + \mathrm{LDOS}_{\mathrm{PG}}(E)]. \qquad (4.2)$$

The polynomial background density of states is given by

$$\mathrm{LDOS}_{\mathrm{background}}(E) = a\,E^2 + b, \tag{4.3}$$

where and a and b are fitting parameters. The phenomenological Mott gap Δ_{Mott} consists of two slightly broadened gap edges, asymmetric around the chemical potential:

$$\mathrm{LDOS}_{\mathrm{Mott}}(E) = \left| \frac{1}{1+e^{(-E-E_0)/w}} - \frac{1}{1+e^{(-E+E_0-\Delta_{\mathrm{Mott}})/w}} \right|, \tag{4.4}$$

where w gives the broadening, E_0 is the energy where the upper Hubbard band roughly pins to the chemical potential and Δ_{Mott} is the size of the Mott gap. We keep the first two parameters fixed ($w = 0.026\,\mathrm{eV}$, $E_0 = 0.1\,\mathrm{eV}$), while the size of the Mott gap is used as a fitting parameter. To fit the pseudogap, we follow ARPES results on electron-doped Sr_2IrO_4 [79, 95] and use a phenomenological function inspired by the d-wave gap function commonly used to fit cuprates spectra [103, 104]:

$$\mathrm{LDOS}_{\mathrm{PG}}(E) = C_0 \left| \frac{E + i\alpha\sqrt{E}}{\sqrt{\left(E + i\alpha\sqrt{E}\right)^2 - \Delta_{\mathrm{PG}}^2}} \right|. \tag{4.5}$$

It contains two fitting parameters: a scaling factor C_0 and the size of the pseudogap Δ_{PG}. We keep α, the effective scattering rate, fixed to $0.2\,\mathrm{eV}^{1/2}$. The square root in the imaginary part is selected to ensure a rather constant broadening independent of the gap.

All the spectra of the spectroscopic map shown in Fig. 4.5 are fitted with this function, using the least squares method. Since for this doping level the upper edge of the Mott gap is pinned to the chemical potential, and because in that location pseudogap and Mott gap overlap, we fit the model to the data only for negative energies. We are able to obtain excellent fits to all the spectra. This allows us to simultaneously extract both the pseudogap Δ_{PG} and the Mott gap Δ_{Mott} for all the spectra, and to plot them as a function of location, as it is shown in Fig. 4.6c-d. From these plots we can learn how the gaps are spatially distributed, and hence what are the length-scales at which the gap widths change. We can then additionally investigate the correlations between the two gaps for $> 10^4$ spectra located in the pseudogap puddles, as it is shown in Fig. 4.6b. We find a positive correlation of 0.31, i.e. the larger the Mott gap, the larger the pseudogap.

In general, the microscopic origin of the pseudogap in electron-doped Sr_2IrO_4 is still a matter of debate. Theoretical proposals include fluctuations of the long-range antiferromagnetic order [105] and the onset of short-range antiferromagnetic order [106]. The latter is supported by experimental evidence that the temperature at which the pseudogap opens ($\approx$100 K, from ARPES [93] and optical spectroscopy [76]) roughly

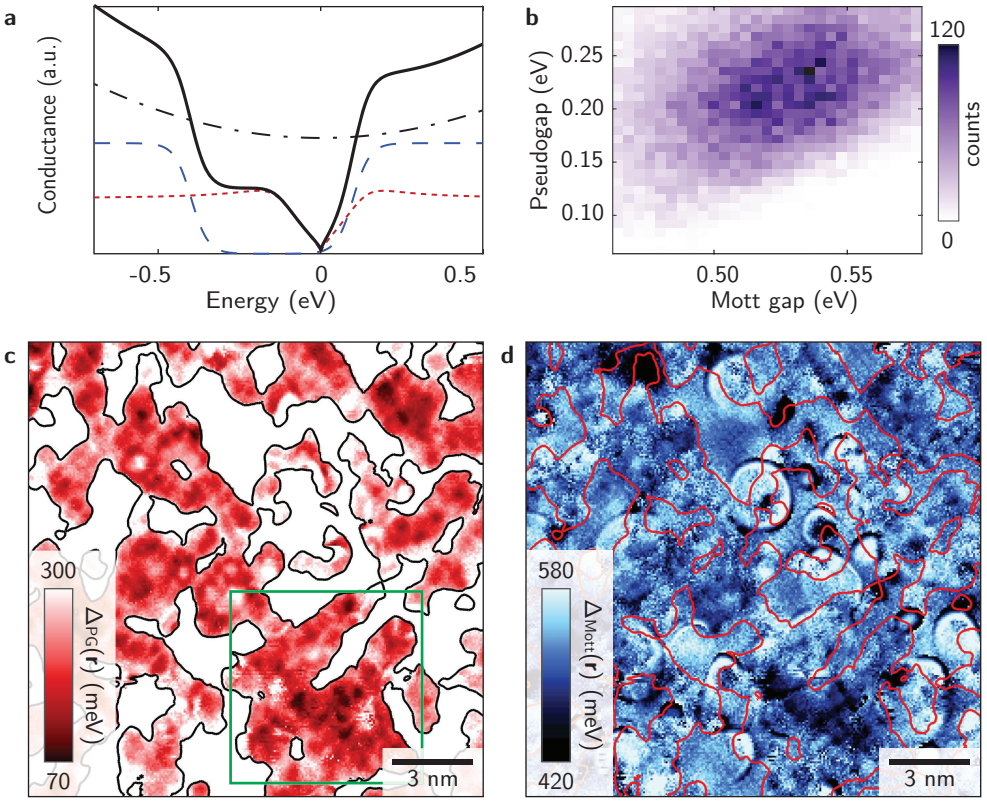

Figure 4.6: **a**, Phenomenological fit function to simultaneously extract both the Mott and pseudogap size. A parabolic density of states (dot-dashed, black) is multiplied with Mott gap (dashed, blue) summed with a V-shaped pseudogap (dotted, red). **b**, Correlation between Mott and pseudogap size for all the spectra showing a pseudogap in the field of view in panel **c**, plotted as a 2D-histogram where the colorscale indicates the amount of spectra falling in each bin. **c**, Pseudogap map extracted from the fitting procedure in the same field of view shown in Fig. 4.5. The green square indicates the area analyzed further in Fig. 4.7. **d**, Mott gap map simultaneously extracted from the same fitting procedure. The circular features are due to TIBB and will be discussed further in chapter 5.

coincides with the onset of short-range antiferromagnetic correlations measured with bulk magnetization and neutron scattering [92].

We interpret the positive correlation emerging from our data as evidence that pseudogap and Mott physics are intimately linked, therefore suggesting that the pseudogap might not simply be caused by magnetic correlations.

4.6.3 Emergent order

After observing the nucleation of pseudogap puddles in the samples, we want to test if the cuprate phenomenology can be extended further to this other lightly doped Mott insulator. In the low-doping region of the cuprates phase diagram, a sizable set of orders coexist, which are sometimes believed to cause the pseudogap [11]. In particular, these include disordered, stripy charge arrangements [4, 13, 19, 107, 108].

We therefore search for such ordered phases within the pseudogap puddles in our samples. We find that the spatial distribution of the pseudogap value, when extracted with atomic precision, reveals a striking tendency for order. We can observe in Fig. 4.6c and Fig. 4.7a that the Δ_{PG} gap maps exhibit glassy, locally unidirectional structures, reminiscent of lightly hole doped cuprates [4, 19, 103].

Glassy charge order is also visible in the density of states right outside the pseudogap. In Fig. 4.7c we show the conductance layer at $-210\,\mathrm{meV}$, where a stripy structure is clearly visible. When plotted together with the position of the Ir atoms (small green dots, while the big green dots still indicate the position of La dopants), it appears that the ordered arrangements consist of bond-centered, unidirectional objects of length scales of two to four Ir-Ir distances, clearly very disordered on a larger length scale. In Fig. 4.7d we show the laplacian of the ratio map $z = g(\text{-}210\,\mathrm{meV})/g(210\,\mathrm{meV})$ where the stripy order is emphasized. Similarly to the pseudogap, these arrangements also nucleate around the dopant atom positions and are not present in the Mott-like areas of the field of view.

The limited data that exist on underdoped cuprates [19, 101, 103] show that the patterns in the conductance layers get more disordered when patches of the sample become insulating. In our measurements, the pseudogap puddles are smaller than what has been observed on the cuprates, and we thus expect the disorder to be even stronger than in cuprates. In the last two panels of Fig. 4.7 we report examples from literature of how order manifests in the cuprates. In Fig. 4.7e, we show the conductance layer measured on an underdoped $Ca_{2\text{-}x}Na_xCuO_2Cl_2$ sample [103]. In Fig. 4.7f, we show the laplacian of the ratio map measured on a (DyBi)-2212 sample [19].

It is clear that the iridates are more disordered, with the stripy patterns appearing only in the pseudogap puddles, and becoming better arranged when the pseudogap puddles get bigger. We can therefore speculate that at higher doping the order observed in the iridates would resemble the one observed in the cuprates.

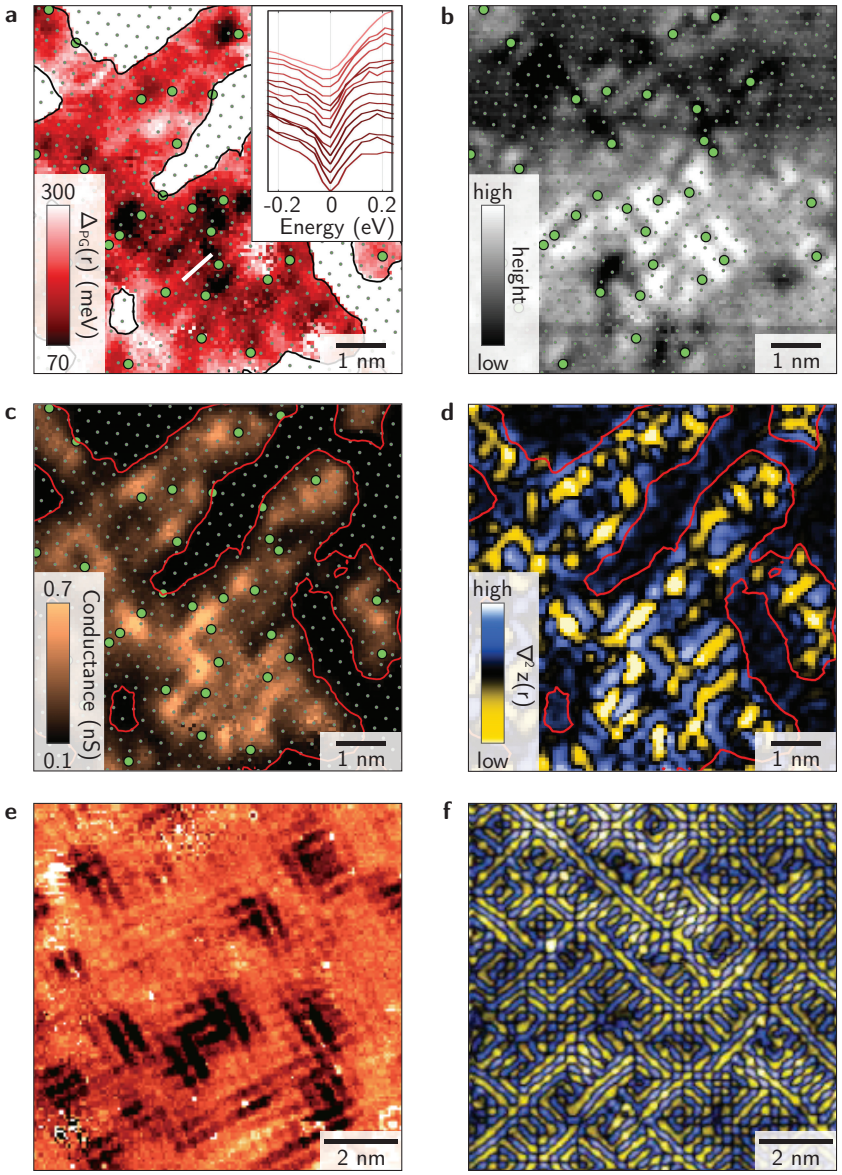

Figure 4.7: **a**, Map of the pseudogap Δ_{PG}, corresponding to the area in the green square from Fig.4.6c. The small green dots indicate Ir atom locations, the larger green circles indicate La dopant locations on the Sr sites. In the inset, spectra along the white line show the variations in the pseudogap, offset for clarity. **b**, Topograph in the same field of view, showing the atomic periodicity. **c**, Conductance layer $g = \mathrm{d}I/\mathrm{d}V$ at -210 meV. Glassy order is nucleating around the La dopant atoms. **d**, Laplacian of the ratio map layer $z = g(\text{-}210\,\text{meV})/g(210\,\text{meV})$. **e**, Conductance layer at -0.22 V measured on an underdoped $Ca_{2-x}Na_xCuO_2Cl_2$ sample, adapted from Ref. [103]. Glassy order is visible only whithin some areas. **f**, Laplacian of the ratio map $z = I(150\,\text{meV})/I(\text{-}150\,\text{meV})$ for a (Dy,Bi)-2212 sample, adapted from Ref. [19].

4.7 Doping evolution: a sharp transition

After illustrating the electronic behavior of the samples at low and high doping levels, we want to elucidate how the evolution towards the pseudogap phase occurs. Since in the iridate samples the dopant atoms can be seen on the surface, we have the unique possibility of measuring samples with densely-spaced local doping concentrations between $x = 2.1\,\%$ and $x = 5.5\,\%$. We measure spectroscopic maps with $> 10^6$ data-points at each doping concentration, and we analyze them using the methods described above. Figure 4.8 summarizes the results: Fig. 4.8a shows the evolution of the averaged spectra, Fig. 4.8b-g show the maps of the Mott parameter on the respective fields of view. For the measurements above $x = 4\,\%$, where phase separation is observed, we show the averaged spectra separately for the pseudogap regions (in red) and for the Mott regions (in blue).

It is clear that at a certain doping threshold, around $x = 5\,\%$, the electronic behavior undergoes an abrupt transition from a purely Mott-like state to a phase-separated Mott/pseudogap electronic landscape. At doping concentration below the transition threshold, none of the spectra exhibits any sort of impurity state, as we already emphasized in Sec. 4.5. Nor is the chemical potential pinned to the bottom of the upper Hubbard band, as one would expect from an electron-doped Mott insulator with shallow dopant centers. Moreover, the phenomenology of the electronic structure is surprisingly independent of the doping concentration for $x < 4\,\%$, showing a clear Mott gap with small variations. This leads to the question: Where did all the dopant electrons go?

We propose the scenario illustrated in Fig. 4.9. Randomly distributed La dopants form localized states within the forbidden energy gap, similarly to what happens when inserting donors in a semiconductor [109, 110]. At low doping, the dopant energy levels aggregate into a narrow range of energy, forming what in semiconductor parlance is called an 'impurity band' (note that this is a partially misleading term, as the electrons wave functions remain localized [110]). This nevertheless shifts the chemical potential to the mid-energy of the impurity band. In a simple one-electron picture and for shallow dopant centers, this scenario typically leads to a quick collapse of the insulating gap towards conductivity, with the impurity band merging into the conduction band and the chemical potential shifting into the latter. This simplified picture might however change when the extra electrons also experience the strong on-site Coulomb repulsion U. It was proposed by N.F. Mott that, due to the strong electron-electron correlations in the impurity band, a Mott gap can open in the latter, creating a filled lower band and an empty upper band [5, 110, 111].

We think that this is the scenario that can best explain our experimental results. There are however some points to address: How can we explain the total absence of

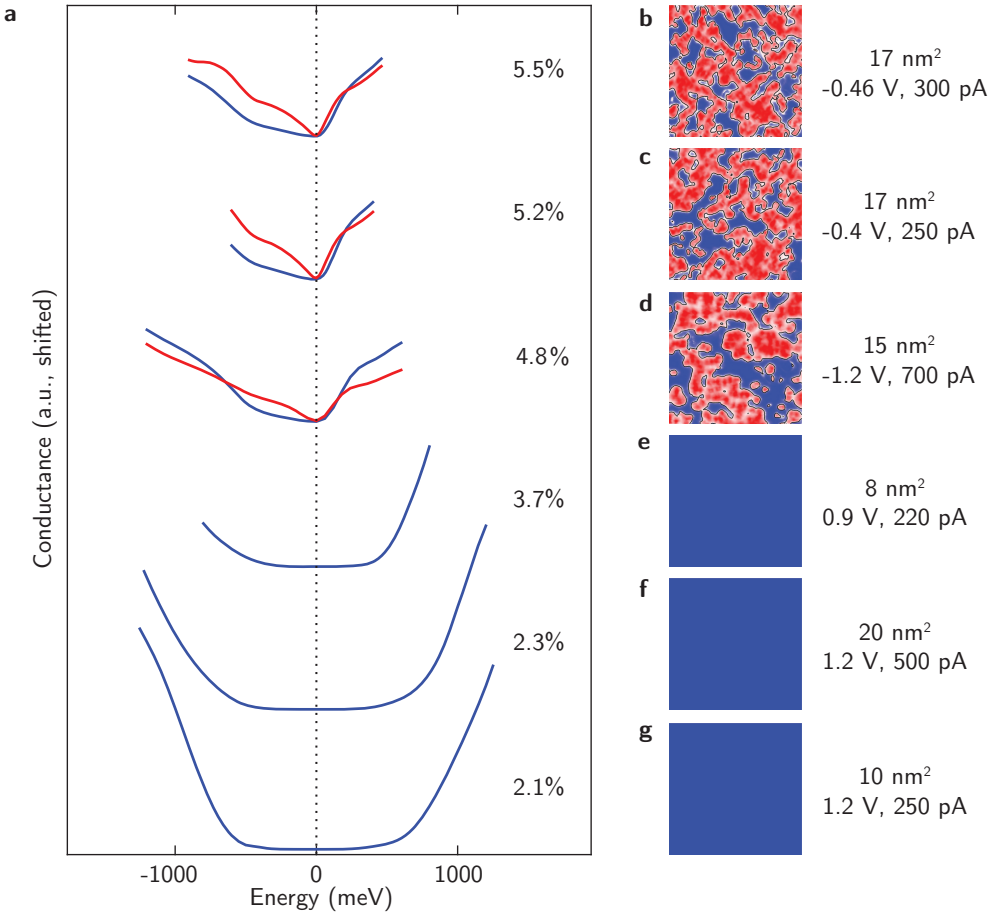

Figure 4.8: Evolution of the electronic structure with increasing dopant atoms concentration. **a**, Density of states spectra at different doping levels, each averaged over regions with Mott gap (blue) and pseudogap (red) as defined by the Mott parameter in **b**-**g**. Due to the different setup conditions for the different measurements, the spectra are normalized by their setup conditions (indicated to the right of each panel), $(\mathrm{d}I/\mathrm{d}V)/(I_\mathrm{s}/V_\mathrm{s})$. **b**-**g**, Respective maps of the Mott parameter, where blue indicates a pure Mott gap, and red indicates a pseudogap puddle.

in-gap states? Why is the chemical potential not shifting towards the upper Hubbard band with electron doping?

We propose that we do not observe in-gap states because the electron-electron correlations that cause the opening of the Mott gap in the impurity band are strong enough to push the resulting subbands outside of the Mott gap itself, as illustrated in Fig. 4.9c.

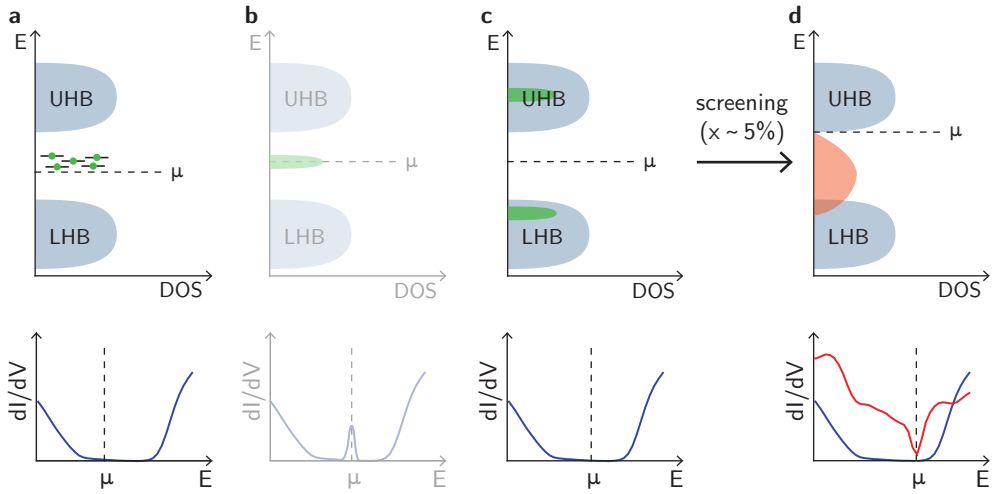

Figure 4.9: Illustration of the melting of the Mott state. **a**, With a very few extra carriers, the dopant energy levels aggregate into a narrow range of energy, however the electrons are still localized on the atomic sites. **b**, The extra carriers would eventually form a band at the Fermi level, with the appearance of in-gap states in the $\mathrm{d}I/\mathrm{d}V$ spectra. This is however not observed in $(Sr_{1-x}La_x)_2IrO_4$. **c**, Mott transition in the impurity band: the impurity band gets split due to the strong Coulomb repulsion, and pushed outside the Mott gap. The chemical potential stays at about mid-gap, at the energy of the impurity band. **d**, At sufficient doping, due to electronic screening, the Mott gap collapses and pseudogap puddles appear.

The fact that the chemical potential stays at about mid-gap upon doping indicates that the dopant electrons are tightly bound to the dopant atom, resulting in very deep dopant electronic states. In other words, the chemical potential is indeed moving to the impurity band, but the latter is located very deep, at about mid-gap. The Mott transition does not influence the position of the chemical potential, that remains roughly corresponding to the binding energy of the extra electrons.

Now that we gave a possible explanation for the low doping regime behavior, let us elucidate how the abrupt collapse to the phase-separated landscape takes place. In a static picture, increasing the dopant concentration would eventually lead to an overlap of the localized wave functions, and to a collapse of the impurity Mott state. However, if we assume the small extension of the wave functions necessary to explain the deep trapping of the extra electrons, the doping threshold for the collapse would have to be much higher than what we measure. We propose that, with increasing doping, screening of the long-range Coulomb interaction by doped carriers leads to an abrupt collapse of the impurity Mott state at doping concentrations lower than one would expect in a static picture.

In the cuprates, similar microscopic processes have initially been proposed, but the Mott state is much more fragile: even weak hole-doping of around 2% can destroy the logarithmic divergence in the resistance [112]. This is due to the much smaller energy scales of the trapping in the cuprates; below the transitions, the material behaves similar to a doped semiconductor, with an impurity band close to the energy of the valence band [112, 113]. This is consistent with the later observation that the dopant centers are quite shallow [101]. Based on our results, we predict that LDA+U calculations on doped iridates will reveal the trapping of La dopant states to be much deeper than the equivalent states in the cuprates.

4.8 Discussion and conclusions

In this chapter, we have presented our SI-STM study of the electronic behavior of Sr_2IrO_4 upon electron doping.

The appearance of a pseudogap at doping $x \approx 5\,\%$ is to date well established by different experimental techniques (STM [92, 94], ARPES [79, 95], optics [76, 96]) and theory [106, 114], with open discussions on the microscopic origin of the pseudogap, as mentioned in Sec. 4.6.2.

At lower doping, instead, the picture is still not confirmed. Due to the strong doping inhomogeneities found by us (Sec. 4.3) and by Ref. [96], it is difficult to study samples in this doping concentration with techniques that average over a big area, such as photoemission, transport and optical spectroscopy. Indeed, ARPES studies in the low-doping regime [79, 80] have contrasting results, both with our STM observations and between each other. However, two optical spectroscopy studies seem to be in partial agreement with our results [76, 96]: Both the studies reveal that in the low doping regime, below $x = 4\,\%$, the strong correlations from the Mott state are still present, with the optical transition corresponding to the Mott gap not shifting in energy, and only partially dampening. Above $x = 5\,\%$ doping, signatures of the pseudogap start to appear in both studies, and the Mott transition peak no longer persists. In Ref. [96], the authors also observe a soft collective mode at 40 meV in the low doping regime. They propose that this soft collective mode stems from the excitation of a frozen correlated state of the electrons pinned by disorder associated with the donor states. This interpretation would be consistent with the frozen Mott state proposed by us.

To conclude this chapter, we would like to go back to the comparison between the electron-doped iridates studied here and hole-doped cuprates. Detailed SI-STM measurements on cuprates, for example, $Ca_{2-x}Na_xCuO_2Cl_2$ and $Bi_2Sr_2CaCu_2O_{8+\delta}$, revealed surprising universalities including the glassy charge order observed in the CuO layer. On first look, $(Sr_{1-x}La_x)_2IrO_4$ seems to be a very different beast: electron

instead of hole doping, Ir instead of Cu, $5d^5$ instead of $3d^9$ electronic configuration. However, our data clearly shows that electronic order and pseudogap are present in $(Sr_{1-x}La_x)_2IrO_4$ as well. Moreover, we believe that the interplay between dopants, pseudogap and order seen here holds for the cuprates too. In general, our results, combined with the bigger picture emerging from literature on doped Sr_2IrO_4, confirm that the phenomenology observed in the low-doping region of the phase diagram of the cuprates is not specific to the copper oxide planes, but generic to a bigger class of two-dimensional lightly doped Mott insulators. By extension, we can expect $(Sr_{1-x}La_x)_2IrO_4$ to become a high-temperature superconductor at only slightly higher doping concentration.

5

Poor electronic screening in lightly doped Mott insulators

This chapter has been published as:
Battisti *et al.*, Phys. Rev. B **95**, 235141 (2017).

5.1 Introduction

One of the unsolved mysteries that we encountered in chapter 4 is that the effective Mott gap measured by scanning tunneling microscopy in the very lightly doped Mott insulator $(Sr_{1-x}La_x)_2IrO_4$ differs greatly from values reported by photoemission spectroscopy and optical experiments [71, 73, 78, 79].

In the present chapter, we focus on this observation. We attribute its origin to poor electronic screening of the tip-induced electric field in the sample. This phenomenon is well known from STM experiments on semiconductors and goes under the name of tip-induced band bending (TIBB) [49, 50]. In principle, TIBB can affect measurements of all materials with poor electronic screening, including Mott insulators. Indeed, signatures of TIBB are observed for the lightly hole-doped oxychloride $Ca_2CuO_2Cl_2$ [103], and poor electronic screening effects around charged impurities are observed for Fe dopants in the topological insulator Bi_2Se_3 [115], for Co adatoms in graphene [116] and possibly for chiral defects in $Sr_3Ir_2O_7$ [98, 117]. TIBB has also been discussed for 2D transition metal dichalcogenides [118] and for graphene systems [119]. However, other than in semiconductors and especially with respect to Mott insulators, the effects of TIBB have not been analyzed in much detail.

Here, we develop a model for TIBB specifically for lightly doped Mott insulators. When applied to the iridate $(Sr_{1-x}La_x)_2IrO_4$, the model is able to retrieve the intrinsic energy gap from the measured STM data, obtaning a value that reconciles with literature. In general, this model allows us to better understand the physics of the material, and to provide new insights for STM experiments on lightly doped Mott insulators.

We begin with an overview of the phenomenon of TIBB in Sec. 5.2. We start from its basics in semiconductor physics, and we discuss differences and similarities between Mott insulators and semiconductors with respect to the problem of electric field penetration. Section 5.3 is the core of the chapter. Here, we show clear indications of electric field penetration in the iridate samples, and we develop an algorithm to retrieve the intrinsic energy gap from the measured STM gap. Finally, in Sec. 5.4, we show a different manifestation of TIBB in the iridate samples, appearing at doping $x \approx 5\,\%$.

5.2 Poor electronic screening and tip-induced band bending

A good measure of how efficiently mobile charges inside a material can screen an externally applied electric field, is given by the screening length λ_s. When a charge

q is added to an electron liquid, its Coulomb potential $\phi(r)$ is screened as $\phi(r) = q/r \cdot e^{-r/\lambda_s}$. In metals like copper, the charge potential is almost perfectly screened since $\lambda_s = 0.5\,\text{Å}$, whereas, in less conducting materials, λ_s can be higher by a few orders of magnitude. In semiconductors, it is typically of the order of 10 nm [120, 121].

As illustrated in Sec. 2.4, Fig. 2.5, poor electronic screening is very detrimental for STM experiments performed on semiconductors. In contrast to metallic samples, here the electric field generated by the tip can partially penetrate the surface, causing an additional potential drop inside the material. This can strongly affect the interpretation of STM data. For instance, the gap measured with tunneling spectroscopy can significantly differ from the intrinsic bandgap in the density of states of the sample, as it has been observed, e.g., on the surfaces of Ge(111) [48], FeS_2(100) [122] and ZnO(110) [123]. Moreover, TIBB can cause the ionization of donors/acceptors in the semiconductor [124–126], an effect that has been used in tip-induced quantum dot experiments [120].

In all these cases, being able to quantitatively calculate the band bending potential φ_{BB} at the surface is necessary for the correct interpretation of STM data: only if the value of φ_{BB} is known, the intrinsic bandgap can be retrieved from the data, and the binding energies of the donors/acceptors can be extracted. For semiconductors, this is often done with a Poisson's equation solver developed by Feenstra [51], that uses the known dielectric constant and carrier concentration. This treatment yields apparent bandgaps ≈15-20% larger than the intrinsic ones [48, 122].

While Mott insulators share the reduced ability to screen electric fields with semiconductors, their underlying physics is radically different due to the strong electron-electron correlations (see Sec. 1.2). As a consequence, several material parameters that are easily accessible in semiconductors, such as the number of carriers, are difficult to estimate for a (lightly doped) Mott insulator. The models developed for calculating φ_{BB} in semiconductors can therefore not be applied to Mott insulators. In the following, we develop a model of electric field penetration in the absence of free carriers specifically for lightly doped Mott insulators.

5.3 Influence of poor screening on the energy gap of $(Sr_{1-x}La_x)_2IrO_4$

We now concentrate on the lightly doped Mott insulator $(Sr_{1-x}La_x)_2IrO_4$ at doping levels $x < 4\%$. The physics of the material has been thoroughly discussed in chapter 4, and all the experimental conditions are the same. In section 4.5, we left the open mystery that the gap in the sample LDOS as measured with STM is significantly bigger, and thus in disagreement with the one reported by other techniques. Here, we

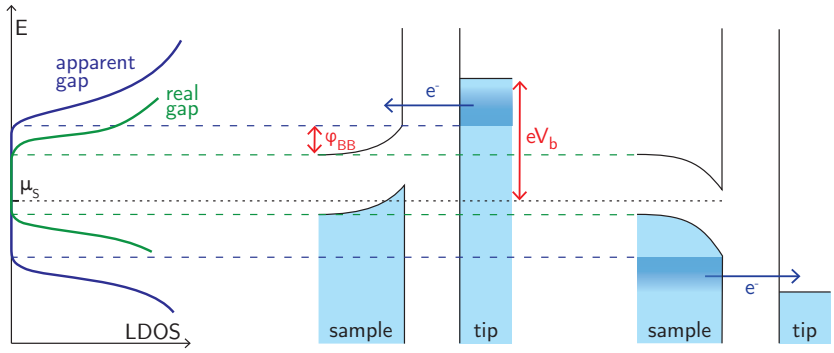

Figure 5.1: Schematic illustration of a tunneling spectroscopy experiment on a Mott insulator in absence (green) and presence (blue) of TIBB. The apparent gap measured with STM is bigger than the intrinsic gap of the material.

show how this can be attributed to the presence of field penetration in the material, and how we can correct for this phenomenon.

The main effect of field penetration is that the voltage between the tip and the sample surface directly below the tip no longer corresponds to the applied bias voltage V_b, but only to a fraction of it. It is relatively easy to qualitatively understand why this causes the measured STM gap to be bigger than the intrinsic gap in the sample LDOS. Let us consider in Fig. 5.1 how a scanning tunneling spectroscopy experiment is affected by the presence of TIBB. When acquiring a spectrum, the bias voltage V_b is swept while measuring the differential conductance $\mathrm{d}I/\mathrm{d}V$. In the case of a gapped LDOS as in a Mott insulator, the onset in the tunneling current occurs when the tip Fermi level crosses the lower boundary of the upper Hubbard band or the upper boundary of the lower Hubbard band. Both events occur at higher absolute bias voltages V_b in the presence of TIBB, as the bands bend upwards or downwards following the position of the tip Fermi level. Thus the apparent gap is wider than the real one when the tip electric field penetrates the sample.

In the following, we develop an algorithm that is able to retrieve the value of the intrinsic energy gap from the measured one. First, we need to calculate the value of the band banding potential φ_BB at the sample surface directly below the tip apex. For Mott insulators, this has never been done before: The models developed to calculate φ_BB in semiconductors [51] cannot be applied, since they require knowledge of the band structure, the carrier concentration and the dielectric constant, quantities that are not always available for Mott insulators. In Sec. 5.3.1, we introduce a model for electric field penetration in absence of free carriers that allows us to get an estimate of φ_BB by using the image charges method. Then, in Sec. 5.3.2, we use the obtained value of φ_BB as input parameter of an algorithm that allows us to retrieve the real

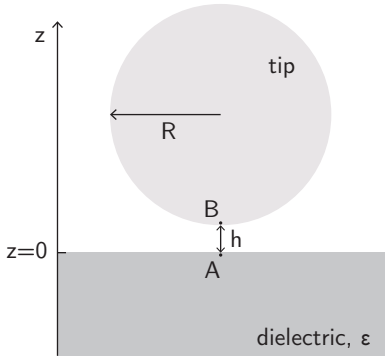

Figure 5.2: Schematic representation of the configuration used to calculate the band bending potential using the image charges method.

energy gap in the sample LDOS from the gap measured with STM, bridging the apparent contradiction with literature.

5.3.1 Calculation of the band-bending potential

Here, we develop a simple model of electric field penetration in the absence of free carriers that allows us to calculate the band-bending potential φ_{BB} for a lightly doped Mott insulator where important material parameters are unknown.

We consider the situation depicted in Fig. 5.2. As a first approximation, we model the tip as a conductive charged sphere of radius R at a distance h from the sample, where $h \ll R$, and the sample as a dielectric medium with dielectric constant ε filling a half-space. We consider a bias voltage V_{b} applied between the tip and the bottom of the sample, which is grounded. We need to find the band-bending potential φ_{BB} at the point of the sample closest to the tip (point A in Fig. 5.2), as a function of the bias voltage V_{b} applied to the tip.

In order to calculate the electric potential φ_{BB}, we make use of the image charges method [127]. In the simplest approximation of a uniformly charged sphere that can be replaced with a single point charge at the center of the sphere, an analytic expression for TIBB can be obtained:

$$\varphi_{\mathrm{BB}}(V_{\mathrm{b}}, R, h, \varepsilon) = \frac{1}{1+\varepsilon\frac{h}{R}} \cdot (eV_{\mathrm{b}} - W_0), \tag{5.1}$$

where $W_0 = W_{\mathrm{sample}} - W_{\mathrm{tip}}$ represents the difference in work functions between sample and tip. In a more realistic configuration, the surface charge redistributes on the sphere. This problem has no analytical solution, and the expression for φ_{BB} has to

be found numerically by using an infinite series of converging image charges with diminishing absolute value[1]. The set of image charges is built in the following recurrent sequence: A charge q is added to the uncharged sphere, which is the equivalent of a point charge in the center of the sphere $(q; R+h)$. This point charge induces an image charge in the dielectric medium $(-kq; -(R+h))$, where $k = \frac{\varepsilon-1}{\varepsilon+1}$. This in turn induces a dipole image on the sphere, $(\frac{-kqR}{2(R+h)}; R+h)$ and $(\frac{-kqR}{2(R+h)}, r+h-\frac{R^2}{2(R+h)})$, and so on. The electric potential in the whole space is then given by

$$\varphi(\mathbf{r}) = \frac{\kappa}{4\pi\varepsilon_0} \sum_i \frac{q_i}{|\mathbf{r}-\mathbf{r}_i|}. \tag{5.2}$$

For $z \geq 0$, $\kappa = 1$ and $(q_i, \mathbf{r}_i)$ are the initial charge and all the image charges induced on the sphere and in the sample. For $z < 0$, $\kappa = \frac{2}{1+\varepsilon}$ and $(q_i, \mathbf{r}_i)$ are the initial charge and all the image charges induced on the sphere [127].

From Eq. (5.2), we can compute $\varphi(\mathbf{r} = A)$, which corresponds to the value of φ_{BB} at the point on the sample closest to the tip. Because the value of φ_{BB} depends on the bias voltage V_{b} applied to the tip, we also compute the potential at $\varphi(\mathbf{r} = B)$. We can then extract the proportionality constant between φ_{BB} and V_{b} from the ratio of this two potentials,

$$F(R, h, \varepsilon) = \frac{\varphi(\mathbf{r} = A)}{\varphi(\mathbf{r} = B)}, \tag{5.3}$$

obtaining finally the following expression for φ_{BB}:

$$\varphi_{\mathrm{BB}}(V_{\mathrm{b}}, R, h, \varepsilon) = F(R, h, \varepsilon) \cdot (eV_{\mathrm{b}} - W_0). \tag{5.4}$$

The value of φ_{BB} therefore depends on the tip radius R, the tip-sample distance h, the static dielectric constant of the sample ϵ and the difference in work functions between sample and tip. In order to calculate φ_{BB}, we fix the values of R and ε to realistic parameters of our experiment. Using SEM, we measure typical radii R for our tips of 25 nm. We estimate the static dielectric constant of a typical Mott insulator as $\varepsilon = 30$ (based on Ref. [128] for La_2CuO_4 and Ref. [129] for Sr_2IrO_4). We assume that this value can still be applied in the case of a very low doping concentration of $\approx 2{-}3\%$ extra holes or electrons.

We further make use of finite element analysis (FEA) performed with the software package Comsol [60], first to confirm the results obtained with the image charges method on the simplified geometry, and second to estimate how different these results are in a more realistic geometry. In the latter, the tip is modeled as a cone with aperture of 20° ending with a spherical segment with the same tip radius R. The two configurations computed with FEA are represented in Fig. 5.3, where the calculated equipotential lines are shown.

[1] We verified that the simplified situation of a uniformly charged sphere underestimates φ_{BB} by a factor of two for our setup, requiring to take the full charge redistribution into account.

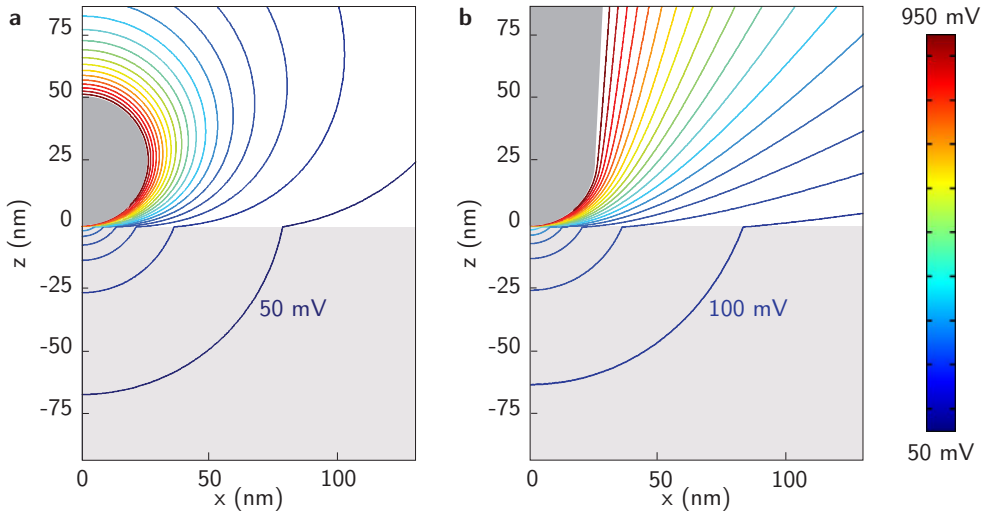

Figure 5.3: Result of FEA performed with Comsol [60] showing the electrical potential around tip and sample. **a**, Simplified spherical tip geometry. **b**, Conical tip geometry. In both panels, the tip-sample distance is set to 5 Å and the equipotential lines, emphasizing the electric field penetration in the sample, are equally spaced by 50 mV. The equipotential line at 50 mV in panel **b** is not visible, because it is deeper below the surface of the sample.

In Table 5.1, we report the values of $F(R, h, \varepsilon)$ obtained from the image charges method and from the two configurations calculated with FEA for a selection of tip-sample distances (where for simplicity we set $W_0 = 0$). The image charges method results agree within 1 % accuracy with FEA results performed on the same simplified geometry, and if the more realistic geometry is taken into account, the value of φ_{BB} increases by $\approx 10\,\%$. We can therefore conclude that our approximation of a spherical tip yields reasonable results.

h (Å)	image charges	FEA sphere	FEA cone
3	0.430	0.426	0.457
5	0.354	0.353	0.388
7	0.309	0.309	0.346

Table 5.1: Values of $F(R, h, \varepsilon)$ obtained for three different tip-sample separations h from different methods: image charges method, FEA on spherical tip geometry, FEA on conical tip geometry.

5.3.2 Algorithm to retrieve the real energy scales in the LDOS

After obtaining the expression for φ_{BB} in Eq. (5.4), we can use it to extract the native density of states from the STM spectra. In addition to the calculated value of φ_{BB}, our algorithm needs as input parameters a series of $\mathrm{d}I/\mathrm{d}V$ spectra measured at the same location with different tip-sample distances (fixed V_{s} and varying I_{s} covering at least one order of magnitude) and an $I(z)$ spectrum.

Measuring a series of spectra with different set-up conditions can already give an indication for the presence of TIBB (even though it usually cannot rule it out). Figure 5.4a shows a series of $\mathrm{d}I/\mathrm{d}V$ spectra measured subsequently at the same location with increasing tip-sample distances on a $(Sr_{1\text{-}x}La_x)_2IrO_4$ sample with 2.2 % doping. The setup bias voltage is kept constant at $V_{\mathrm{s}} = 1.5\,\mathrm{V}$ and the setup current I_{s} ranges from 600 pA to 10 pA, covering almost two orders of magnitude. A clear dependence on the setup conditions, reflecting a dependence on the tip-sample distance, is visible.

We can calculate $G = \mathrm{d}I/\mathrm{d}V$ in the presence of TIBB by taking the derivative with respect to V_{b} of Eq. (2.12):

$$G(V_{\mathrm{b}}, h) = \frac{4\pi e^2}{\hbar}\left(1 - \frac{\partial\varphi_{\mathrm{BB}}(V_{\mathrm{b}}, h)}{\partial V_{\mathrm{b}}}\right)|M(h)|^2\; g_t\; g_s\big(eV_{\mathrm{b}} - \varphi_{\mathrm{BB}}(V_{\mathrm{b}}, h)\big). \tag{5.5}$$

The tip-sample distance h is mainly included in the unknown tunneling matrix elements $|M(h)|^2$. Following Ref. [23], we eliminate $|M(h)|^2$ by normalizing the differential conductance $G(V_{\mathrm{b}}, h)$ by the setup current divided by the setup voltage:

$$\bar{G}(V_{\mathrm{b}}, h) \equiv \frac{G(V_{\mathrm{b}}, h)}{I_{\mathrm{s}}/V_{\mathrm{s}}}. \tag{5.6}$$

In absence of TIBB, $\bar{G}$ would become independent of h, and such normalized spectra should collapse on a single curve. We apply Eq. (5.6) to the data in Fig. 5.4a, plotting the result in Fig. 5.4b: the curves do not collapse exactly on each other, the biggest differences arising for negative energies (see arrow). We quantify this difference by the standard deviations calculated for each energy, shown as the gray line in Fig. 5.4b. The differences in the normalized spectra are due to the presence of TIBB and thus further modeling is required to extract the intrinsic sample LDOS.

To do so, we calculate an effective bias voltage $V^{\mathrm{eff}}(h)$ for each tip-sample distance h such that

$$eV_{\mathrm{s}} - \varphi_{\mathrm{BB}}(V_{\mathrm{s}}, h) \equiv eV^{\mathrm{eff}}(h) - \varphi_{\mathrm{BB}}(V^{\mathrm{eff}}(h), h_0) \tag{5.7}$$

for a fixed tip-sample distance h_0.

Using Eq. (5.7), we rewrite the tunneling equation Eq. (2.12) as:

$$\int_0^{eV_{\mathrm{s}} - \varphi_{\mathrm{BB}}(V_{\mathrm{s}}, h)} g_s(\epsilon)\,\mathrm{d}\epsilon = \frac{I(V^{\mathrm{eff}}(h), h_0)}{\frac{4\pi e}{\hbar}|M(h_0)|^2 g_t}. \tag{5.8}$$

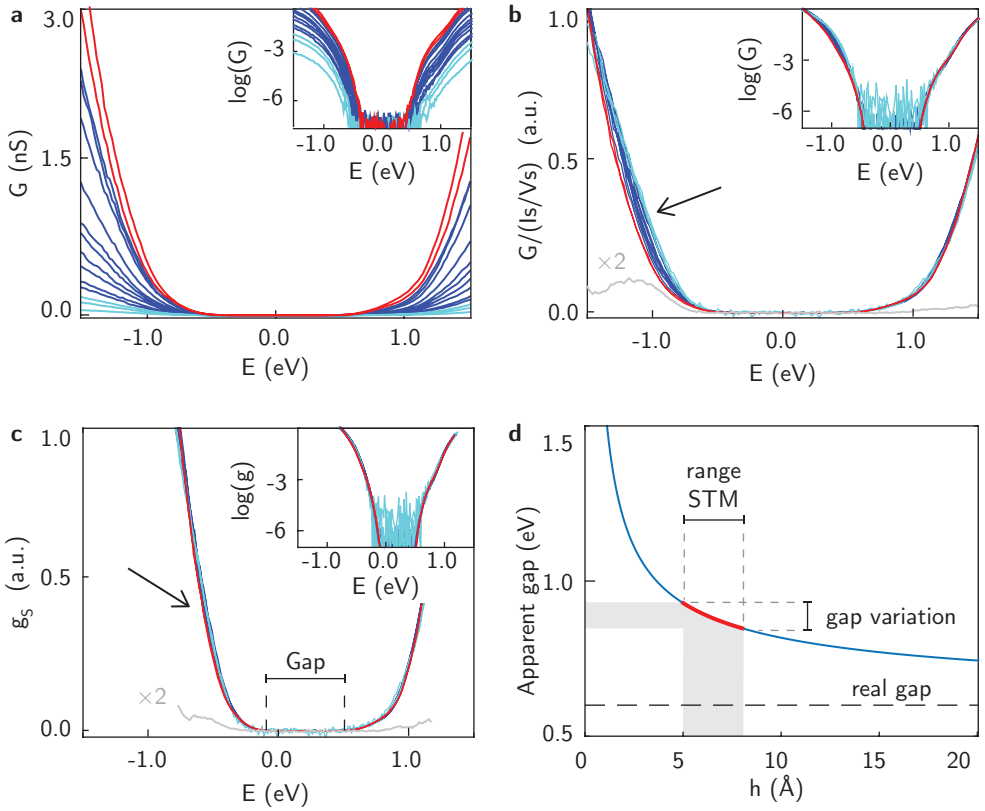

Figure 5.4: **a**, $G \equiv dI/dV$ spectra measured at different tip-sample distances h on a sample with 2.2% doping. The bias setup voltage V_s is fixed to 1.5 V and the current I_s goes from 600 pA (red) to 10 pA (light blue). In all insets the corresponding plot is shown on a logarithmic scale. **b**, The same spectra as in panel **a**, each normalized by its setup junction resistance I_s/V_s. The gray line shows the standard deviation $\sigma(G)$ calculated for each energy, multiplied by a factor two. **c**, Intrinsic LDOS g_s after correction for TIBB, obtained from Eq. (5.9). Since the rescaling of the curves causes different horizontal axes for each curve, we calculate $\sigma(g_s)$ over extrapolated values of g_s at equally spaced energies. **d**, Calculated apparent gap as a function of tip-sample distance.

By inserting Eq. (5.8) into Eq. (5.5) divided by the setup conditions, we can extract the intrinsic density of states $g_s(\epsilon)$ from measured $G(h)$ curves at different heights:

$$g_s(\epsilon) = \frac{G(h)}{I_s/V_s} \frac{1}{1 - \frac{\partial \varphi_{BB}(V_b,h)}{\partial V_b}} \frac{I(V^{\text{eff}}(h), h_0)}{\frac{4\pi e^2}{\hbar}|M(h_0)|^2 g_t}, \tag{5.9}$$

where $\epsilon = eV_b - \varphi_{BB}(V_b, h)$. The parameters in the model are the dielectric constant ε, the tip radius R, the difference in work functions W_0, the minimal tip-sample distance $h_{\min}$ and the exponential prefactor κ of the tunneling current $I = I_0 \cdot e^{-\kappa h}$.

We keep R and ε fixed at the values mentioned in Sec. 5.3.1. We estimate $h_{\min} = 5\,\text{Å}$ as a typical tunneling distance for $1\,\text{G}\Omega$ tunneling resistance for this material. From measured $I(z)$ curves, we determine $\kappa = 1.1\ \text{Å}^{-1}$. Thus the only free parameter left in Eq. (5.9) is W_0.

We apply our model to the data of Fig. 5.4a, extracting the parameter W_0 as the value that minimizes the error function $\Omega = \int[\sigma(g_s)]^2$, where $\sigma(g_s)$ are the standard deviations of the g_s curves for each energy. Minimization gives a work function difference between tip and sample of $W_0 = 0.55\,\text{eV}$.

We show in Fig. 5.4c the result of the application of our model to the data. The resulting spectra are rescaled in energy, leading to a gap value of 600 meV and to a shift of the onset of the lower Hubbard band to $-0.1\,\text{eV}$. This is in good agreement with values reported in literature by optical spectroscopy, theory and ARPES [71, 73, 77–79], allowing us to reconcile our measurement to the other techniques.

In Fig. 5.4d, we show the calculated evolution of the apparent gap with tip-sample distance. While there is a remarkable difference between the intrinsic gap value and the apparent gap, we want to stress that, within the values of h in which STM experiments are typically conducted, the variation of the apparent gap is relatively small. Therefore, even when measurements do not show sizable dependence on setup conditions, TIBB might be present, and further analysis might be required to retrieve the intrinsic energy scales.

5.4 Bubbles in the conductance layers of $(Sr_{1-x}La_x)_2IrO_4$

In the samples with higher doping levels ($x \approx 5\,\%$), we observe a different signature of field penetration: circular rings of enhanced conductance appear in the layers of constant energy of the spectroscopic maps. In the following, we will refer to these features as 'bubbles'. Their diameter increases with energy, as shown in Fig. 5.5a-d, causing hyperbolas of enhanced conductance in a (E, r) plot, as shown in Fig. 5.5e. We shall see that these bubbles are generated by the presence of a low concentration of specific impurity atoms which can be used as a probe to better understand the field penetration in the material.

Very similar features have been observed in semiconductors, where they are identified as markers of ionization/empty state filling of donors or acceptors induced by the vicinity of the STM tip. 'Bubbles' in semiconductors have been thoroughly studied because they can help in extracting material parameters such as the binding energy of the donors. This was done for instance for Si donors in GaAs [124, 125], for which it was further demonstrated that donors closer to the surface have an enhanced binding energy with respect to the bulk [130]. Effects of charge manipulation by the STM tip

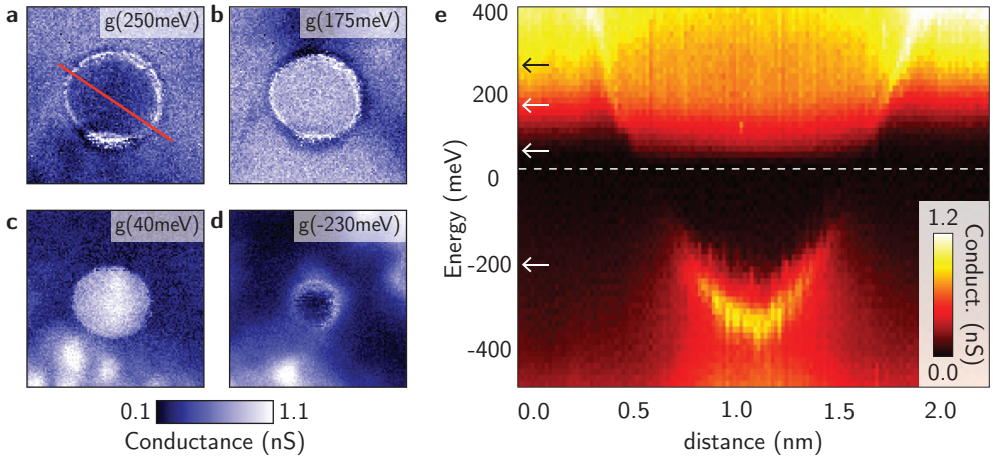

Figure 5.5: Visualization of a tip-induced band bending bubble in $(Sr_{1-x}La_x)_2IrO_4$ at x=5.5 %. **a-d**, Conductance layers in a field of view of $3\times3\,nm^2$ at 250 meV, 175 meV, 40 meV, -230 meV, respectively. **e**, (E,r) plot of the bubble along the red line in **a**. The hyperbolic profile visualizes the increasing diameter of the bubble with increasing energy. The arrows indicate the energies at which the conductance layers shown in panels **a-d** are extracted.

and enhanced binding energy closer to the surface were also reported for Mn acceptors in InAs and GaAs [121, 131] and for donors in ZnO [132, 133]. Moreover, bubbles due to TIBB effects have also been reported when using a scanning capacitance probe to image transport in two-dimensional electron gas in AlGaAs/GaAs heterostructures [134]. Despite semiconductors being relatively simple and accessible systems, the physics governing the appearance of the bubbles is quite complicated, and many details are not yet agreed upon.

We note that signatures of finite field penetration resembling the bubbles observed in our samples are also found in other correlated-electron systems, such as the lightly hole-doped oxychloride $Ca_2CuO_2Cl_2$ [103] and possibly the correlated iridates $Sr_3Ir_2O_7$ and $Sr_3(Ir_{1-x}Ru_x)_2O_7$ [98, 117, 135]. However, these bubbles have never been discussed in details for a correlated-electron system.

We expect that the mechanism leading to the formation of bubbles in our samples is the same as in semiconductors, and we refer to Ref. [124, 125] for a detailed description of the processes.

Here, we emphasize that the impurity atoms in our samples are identified as electron donors, that each of these donors generates one hyperbola as in Fig. 5.5d, and that the two parts of the hyperbola lying above and below the chemical potential come from two different tunneling processes. For $V_b > 0$, the enhanced conductance is due to the ionization of the donor, which locally changes the potential landscape in the sample.

In this process, the electrons tunnel from the tip to the bulk of the sample, therefore the bubble becomes visible only after the onset of the upper Hubbard band. For $V_b < 0$, the enhanced conductance is instead caused by the opening of an additional tunneling channel. In this process, electrons tunnel from the sample bulk to the tip via the donor state. The bubble's diameter in this part of the hyperbola reflects the extension of the donor wave function in real space. Both processes are triggered at a specific value of φ_{BB}, causing the hyperbola to follow a constant φ_{BB} contour. We emphasize that the two parts of the hyperbola will lie on the same constant φ_{BB} contour only when the sample chemical potential roughly coincides with the onset of the upper Hubbard band, otherwise they might be shifted in energy.

In a typical spectroscopic map, we can usually identify several bubbles which start to emerge at different energies. Figure 5.6a shows the topograph of a $17{\times}17$ nm^2 field of view with doping level of 5.5%, where we count 180 dopant atoms on the surface. In the same field of view, the conductance layers show the appearance of only ≈ 15 bubbles (Fig. 5.6b). In general, the number of bubbles that we observe corresponds to less than 10 % of the total number of La dopants present on the surface. We can therefore exclude that La dopants in their normal state cause the appearance of bubbles. Our best hypothesis on the nature of the bubbles is that they originate either from some special chemical state of the La atoms (for instance an oxygen vacancy next to the La atom) or from Pt atoms that substitute for the Ir atoms. The latter could originate from the Pt crucible where the samples were grown.

Even if the origin of the bubbles is not certain, from their presence and behavior we can still extract useful information about the material. Importantly, the bubbles are not influenced by and do not influence the phase-separated density of state of the sample. In Fig. 5.6b, we show the conductance layer at $E = 540\,\mathrm{meV}$ where the black contour indicates the border between pseudogap phase and Mott phase, as defined by the Mott parameter (see Sec. 4.6). The bubbles originate from both Mott regions and pseudogap regions, and when they cross the sharp border between the two regions their shape is not affected. Moreover, the phase-separated landscape and the emerging order that we describe in section 4.6 are not influenced by the presence of the bubbles.

Unfortunately, the model that we developed for the low doping level samples is unable to grasp the physics of the samples with doping $x \approx 5\%$, due to the presence of free carriers in the latter case. We can still make some important qualitative observations by plotting in Fig. 5.6c all the hyperbolas extracted from the bubbles in Fig. 5.6b:

(i), The bubbles start to appear at different threshold potentials. The threshold potential is an indication of the donor depth below the surface [130], with donors that lie deeper below the surface having a lower threshold potential. We therefore conclude that we observe bubbles originating form donors located at different depths.

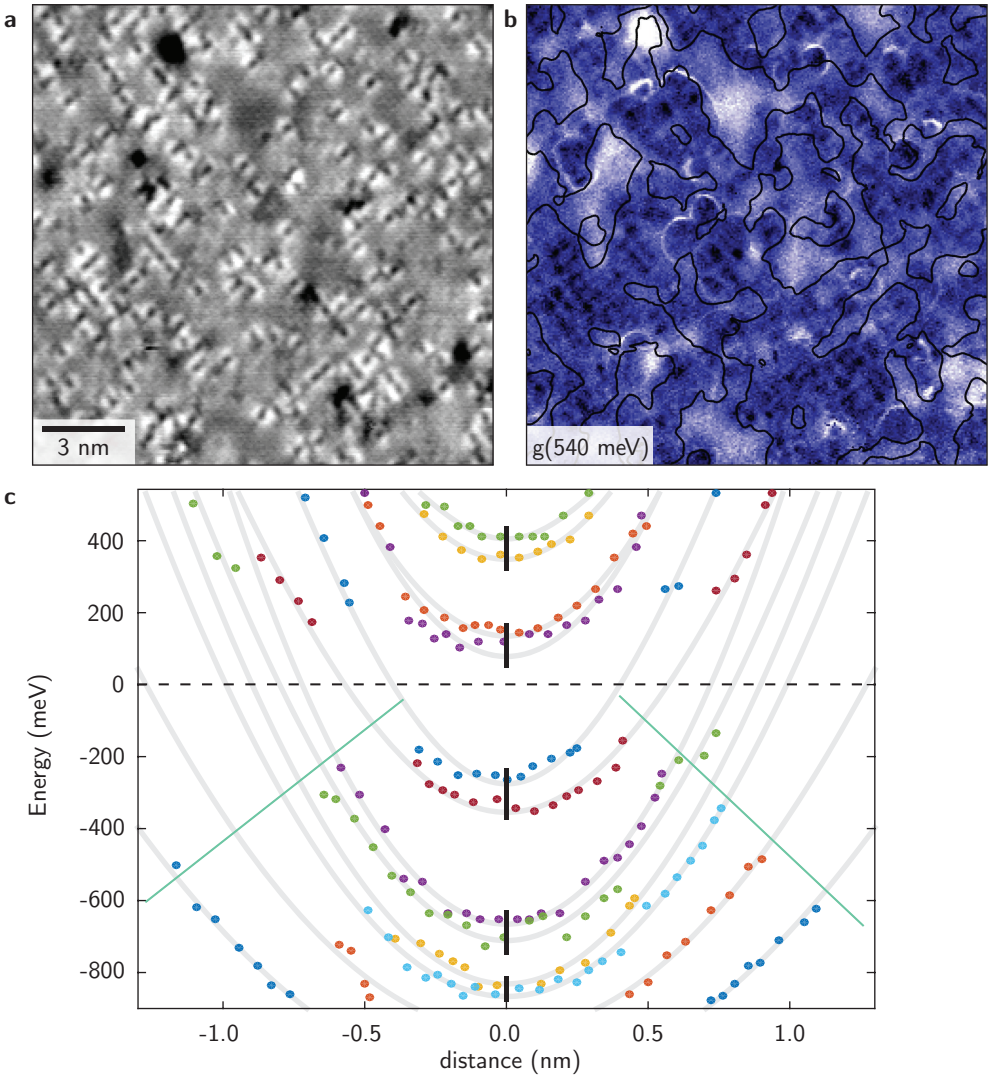

Figure 5.6: **a**, Topograph of a sample with x=5.5 % doping in a field of view of $17\times17\,\mathrm{nm}^2$ (same FOV as in Fig. 4.5). The setup conditions are ($V_s = 460\,\mathrm{meV}$, $I_s = 300\,\mathrm{pA}$). **b**, Conductance layer at 540 meV in the same field of view. We observe ≈15 circular bubbles of different sizes. The black line indicates the phase separation according to the Mott parameter defined in Sec. 4.6. **c**, Hyperbolas extracted from all the bubbles appearing in panel **b**. The gray lines are fits to the hyperbolas, added as a guide to the eye. The two green straight lines emphasize the increasing maximal bubble diameter with increasing donor depth below the surface. The vertical black lines group hyperbolas appearing at similar threshold potentials.

(ii), For the lower part of the hyperbola, the maximum bubble's diameter gets smaller for donors closer to the surface. Since the maximum diameter reflects the real space extension of the donor wave function, this gives evidence for enhanced binding energy for donors closer to the surface [130].

(iii), Most of the bubbles can be grouped as starting at roughly the same threshold potential (within an error of 50 meV), therefore probably originating from donors at the same depth below the surface, i.e. belonging to the same crystal layer. In Fig. 5.6c this is indicated by the short vertical black lines.

Concluding, we would like to emphasize a last important point that might tell us something more about the material. The typical lateral extension of the bubbles in our samples is ≈1.5 nm. This is significantly lower than in semiconductors where, for example, the typical extension of bubbles due to Si donors in GaAs is ≈10 nm. Among the factors that can influence the extension of the bubbles are the tip radius, the concentration of free carriers and the material's electrical permittivity. We can exclude that the tip radius is the cause for the small extension of the bubbles, as one would need to have an unrealistically small tip radius to reproduce the bubbles. We identify two factors that could be responsible for the reduced lateral extension of the bubbles: (i) the resistivity in $(Sr_{1-x}La_x)_2IrO_4$ is lower in the ab-crystal plane than along the c-axis [129], although with diminishing strength upon doping [91]; (ii) the electrical permittivity of Sr_2IrO_4 is anisotropic [129]. We can only speculate that the small extension of the bubbles is related to these effects; in any case it is evidence for the strongly anisotropic electronic structure of the material.

5.5 Conclusions

In this chapter, we showed that electric field penetration in materials with poor electronic screening can strongly influence STM results.

It is important to be aware of the possibility to encounter TIBB when performing experiments on lightly doped Mott insulators and other materials with poor electronic screening (including topological materials [136] and van der Waals heterostructure; magic-angle superconducting graphene [137] would likely be affected by this effect). The presence of TIBB could be difficult to identify, and one has to be extra careful when measuring such materials. The appearance of bubbles in the conductance layer can and should be used as an indication for the presence of TIBB in the sample.

In particular, we showed that the incompatibilities between STM and other techniques in the gap value measured on $(Sr_{1-x}La_x)_2IrO_4$ for $x < 4\%$ are caused by field penetration. We developed a model to correct for this effect that can generally be applied to lightly doped Mott insulators. We showed that, after correcting the data

according to this model, our STM results reconcile with literature. We would like to emphasize that what is discussed in this chapter does not influence the findings of chapter 4. Even though the gap values for the low doping samples as reported in chapter 4 do not correspond to the intrinsic values, our interpretation of the physics of the material is not affected.

6

Quasiparticle interference in the correlated metal Sr_2RhO_4

6.1 Introduction

SI-STM directly probes real space, but in metals or superconductors with sharp quasiparticles, it can also provide information about momentum space. This is possible by imaging the interference of standing waves that are caused by the scattering of quasiparticles. A general introduction to this technique, called *quasiparticle interference imaging*, is given in chapter 2, Sec. 2.3.

The most popular probe to access momentum space information is angle-resolved photoemission spectroscopy (ARPES), also a surface-sensitive technique. ARPES directly measures photon-induced quasiparticle excitations, resolving both energy and momentum. It can therefore measure the band structure of materials.

Because both STM and ARPES have advantages and disadvantages related to their experimental realizations, it is recommendable to combine their results in order to obtain a better understanding of the underlying physics. ARPES has the clear advantage of probing momentum space directly, while STM measures the scattering vectors of quasiparticles. However, ARPES probes only states below the Fermi level, and its best energy resolution is a few meV, limited by temperature. STM, on the other hand, can probe states both above and below the Fermi level, and because it can be performed at much lower temperatures, the energy resolution can be lower. For example, at 250 mK, the energy resolution is $\Delta E_{\mathrm{STM}} \sim 75\,\mu\mathrm{eV}$ (see Sec. 2.5 for details). Thanks to its superior energy resolution, STM has been able, for instance, to detect k-space anisotropy in iron-based superconductors previously invisible to ARPES [138, 139], and to image the band structure of heavy fermions materials where ARPES cannot access the energy scales [37, 38]. Quasiparticle interference imaging also brought enormous insights in the superconducting phase of cuprate high-T_c superconductors [18, 34]. However, in general QPI imaging is a difficult experimental technique, and its theoretical understanding is still in progress [140, 141].

Both STM and ARPES measure quantities proportional to the quasiparticle spectral function, as explained in section 2.3.1. Because the two techniques in principle have access to the same physical information, it is natural to try to compare their results. However, the comparison between the two is not always simple. While they generally agree on the main observed features, they very often differ in the details, as it was shown for example for cuprates [45–47], and for the normal state of Sr_2RuO_4 [43]. In both these systems, the two techniques obtain very similar Fermi surfaces, but different slopes in the energy-momentum dispersions. Discrepancies could be caused by measurements effects in both techniques, i.e., the tunneling/photoemission matrix elements, tip-induced effects, and photon energy and polarization, however they could also be related to more intrinsic factors.

Here, we use quasiparticle interference to study the electronic structure of the correlated metal Sr_2RhO_4, which is an example of an almost perfect Fermi liquid [68]. This material has very sharp quasiparticles and a simple band structure, and it is therefore relatively easy to study with quasiparticle interference. This makes it a good candidate to better understand how STM QPI can be related to ARPES results. Additionally, we study samples belonging to the same batch used in published ARPES and quantum oscillation studies [68, 69], which makes the comparison more sound.

We start with an introduction to the material and to the relevant literature, and then proceed with the presentation of our experimental results. Finally, we compare our data to ARPES results. The data that we show here is the first data that we acquire with our home-built microscope, described in chapter 3. While the data quality is good enough to have some preliminary conclusions, further measurements are needed and planned in order to confirm our findings. We will come back to this while discussing the results and in the conclusions.

6.2 The correlated metal Sr_2RhO_4

The rhodate Sr_2RhO_4 has a tetragonal crystal structure isostructural to the cuprate La_2CuO_4. The RhO_6 octahedra are additionally rotated of 11° around the c-axis, as shown in Fig. 6.1a. Sr_2RhO_4 has therefore an identical structure to the iridate Sr_2IrO_4 that has been discussed in chapter 4.

The octahedra rotation causes the formation of a new orthorhombic unit cell and, consequently, a reduction of the first Brillouin zone, as illustrated in Fig. 6.1b-c. The lattice parameters of the new orthorhombic cell are $a^* = \sqrt{2}a = 5.45\,\text{Å}$ and $c^* = 2c = 25.7\,\text{Å}$, where a and c are the lattice parameters of the undistorted structure [142].

In the periodic table, Rh belongs to $4d$ transition metals. With its odd number of electrons per unit cell (electronic configuration $4d^5$), Sr_2RhO_4 is a metal, as it is expected from simple band structure considerations. Nevertheless, Coulomb correlations U and spin-orbit coupling λ are present in this material as well, and only by taking them into account can the experimentally observed Fermi surface be reproduced by LDA calculations [69, 143, 144].

The most studied $4d$ transition metal oxides are probably the ruthenates Sr_2RuO_4 and $Sr_3Ru_2O_7$. In particular, Sr_2RuO_4 is famous for showing spin-triplet superconductivity below 1.5 K [145]. In the normal state, Sr_2RuO_4 is also a strongly two-dimensional Fermi liquid, with a Fermi surface characterized by three cylindrical sheets, called α (which is hole like), β and γ (which are electron like), as shown in Fig 6.2a. Calculations show that α and β are strongly one-dimensional and are derived from the Ru

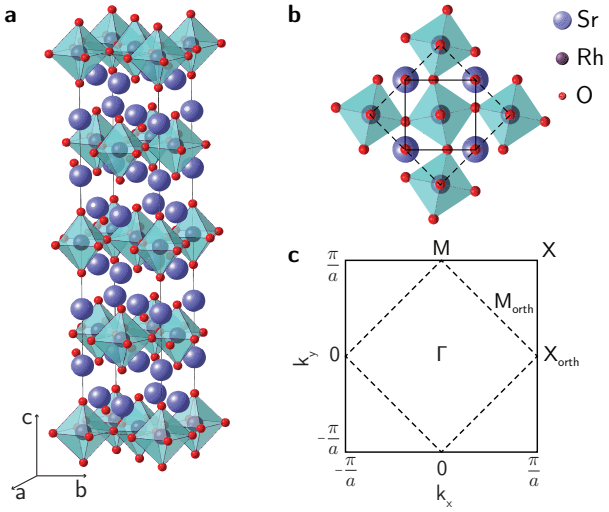

Figure 6.1: **a**, Crystal structure. **b**, Top view of the crystal structure showing the orthorhombic distortion. **c**, First Brillouin zone and reduced BZ due to orthorhombicity. The high symmetry directions Γ, X and M are indicated for both undistorted and distorted structure.

$4d_{xz,yz}$ orbitals, while γ is dominantly two-dimensional, derived from the $4d_{xy}$ orbital [145].

Rhodium has just one atom more than ruthenium, but its electronic structure is quite different. In a naïve picture, one could think to obtain the Fermi surface of Sr_2RhO_4 simply by shifting the Sr_2RuO_4 band structure to accommodate the extra electron of Rh. However, spectroscopic studies, later confirmed by theory, show that Sr_2RhO_4 has only two bands at the Fermi level [69, 143], respectively the α and β bands. In addition, they are back-folded due to the first Brillouin zone reduction caused by the octahedra rotation[1], as shown in Fig. 6.2b. It has been shown that the octahedra rotation is also responsible for the absence of the γ band from the Fermi surface: the structural distortion combined with the folding of the bands causes an additional hybridization of the occupied d_{xy} orbital with the unoccupied $d_{x^2-y^2}$ orbital, which mixes the bands and opens a gap between the two, pushing the d_{xy} band below the Fermi level [143]. The physics of the material is therefore governed by the three electrons per Rh atom that are left at the Fermi level, distributed between the α and β bands.

We will now introduce a brief summary of the most prominent experimental studies that have been performed on the rhodate Sr_2RhO_4, with a focus on photoemission

[1] Sr_2RuO_4 has an undistorted crystal structure, with a normal tetragonal unit cell. Upon cleaving it shows a surface reconstruction with the octahedra rotating by 11° in the top layer only, as for example shown by Ref. [43].

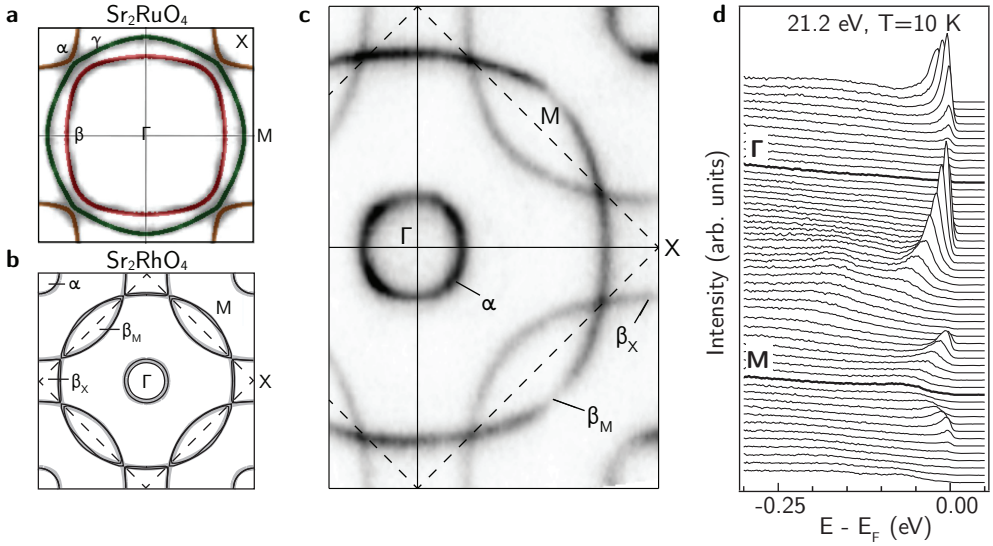

Figure 6.2: **a**, Fermi surface of Sr_2RuO_4, reproduced from Ref. [146]. **b**, Fermi surface of Sr_2RhO_4 as obtained by LDA+SOC+U calculations, reproduced from Ref. [144]. **c**, Fermi surface of Sr_2RhO_4 measured with ARPES at 10 K, reproduced from Ref. [69]. **d**, ARPES spectra along the ΓM direction of the orthorhombic Brillouin zone, reproduced from Ref. [69].

spectroscopy. Later in the chapter, we will compare our STM experimental results to these studies.

We start with crystal growth and transport properties, which have mainly been reported in Ref. [68]. Sr_2RhO_4 single crystals can be grown by the floating zone technique, with the formation of big crystals up to 1.5 cm long. Subsequent annealing in O_2 atmosphere is necessary to improve the quality of the crystals, leading to low-temperature in-plane resistivities $\rho_{ab} < 7\,\mu\Omega\,\mathrm{cm}$. The out of plane resistivity ρ_c is about three orders of magnitude higher, confirming the strongly two-dimensional nature of the electronic structure. The low in-plane residual resistivity is a hallmark of extremely high purity crystals, similar to what is achieved in Sr_2RuO_4. This allows the measurement of quantum oscillations, that are unobservable in most oxide metals due to signal suppression from impurity scattering [68].

Angle-resolved photemission spectroscopy (ARPES) provides an essential contribution to the understanding of the electronic structure of Sr_2RhO_4 [68, 69, 143]. In Fig. 6.2c-d, we reproduce ARPES data from Ref. [69]. The Fermi surface clearly shows the slightly asymmetric hole-like α band and electron-like β band, as well as their copies that are back folded along the orthorhombic zone boundary (dashed line in Fig. 6.2c). A closer investigation of the data reveals that a small gap opens at the crossing of the β band with its back folded copy at the orthorhombic zone bound-

ary, causing the formation of three different pockets at the Fermi surface: the central hole pocket (α), the lens-shaped electron pockets around the M point (β_M) and the square-shaped hole pockets around the X point (β_X). The volume of the pockets as extracted from the ARPES data leads to a total Luttinger volume[2] of three electrons per Rh atom, confirming the picture of a fully occupied γ band.

6.3 SI-STM quasiparticle interference measurements

The sharpness of the quasiparticles that are measured on Sr_2RhO_4 by ARPES and quantum oscillations makes the material a very good candidate for the imaging of quasiparticle interference with STM [70]. In the following, we report our SI-STM measurements on the same Sr_2RhO_4 samples of which growth and measurements are reported in Ref. [68, 69] and summarized in section 6.2. This allows for a direct comparison with ARPES results.

A general explanation of the techniques of quasiparticle interference imaging and Fourier transform STM is given in section 2.3, where we introduce many concepts that are used in the present chapter.

The measurements shown here have been performed with our home-built STM described in chapter 3. The samples are about 2−3 mm in lateral size, and cleave very easily. They are cleaved in situ at ≈20 K, and immediately transferred to the STM head. STM measurements are performed at the base temperature of 4.3 K with a chemically etched tungsten tip that has been previously prepared by field emission on a gold surface. STM topographs are taken in the constant current mode, and the $\mathrm{d}I/\mathrm{d}V$ spectra are collected using a standard lock-in technique with modulation frequency $f = 863$ Hz.

While the data quality we achieve from the very first measurement is confirming the exceptional performance of the microscope in terms of signal-to-noise ratio, it is not yet ideal. In particular, the tip apex shape is not perfect, and we encountered an asymmetry of the piezotube polarization. We can partially remove these effects by post-processing the data, as we explain throughout the chapter. However, to confirm our findings and accumulate more statistics, additional measurements are planned.

In Fig. 6.3a, we show a STM topograph acquired on Sr_2RhO_4. The material, similarly to Sr_2IrO_4, cleaves between SrO layers, and the Sr atoms are visible on the surface with spacing $a = 3.85$ Å. Two different types of defects are visible, and are identified based on Ref. [147]: (i) square-shaped defects, corresponding to a missing Sr atom; (ii) cross-shaped defects, centered at the position of an O atom and corresponding to

[2]Luttinger's theorem states that the volume enclosed by a material's Fermi surface is directly proportional to the particle density. Importantly, this is not changed by the presence of electron-electron interactions.

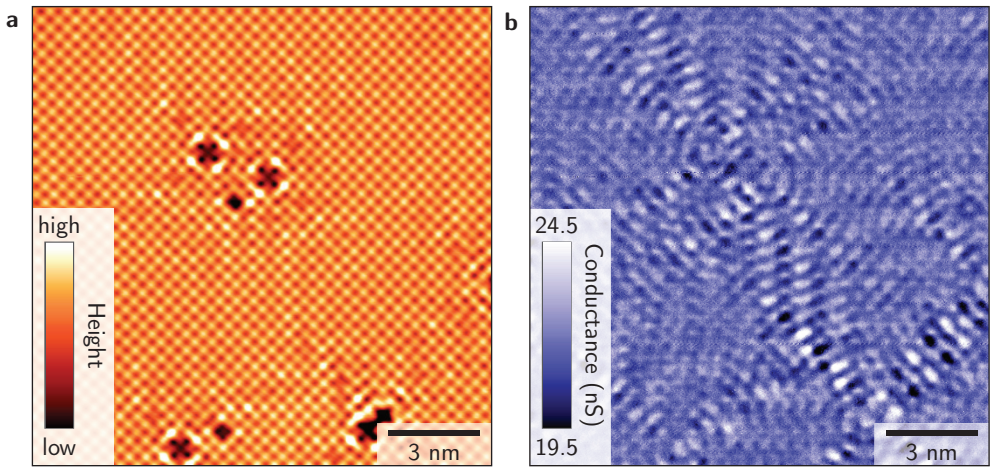

Figure 6.3: Quasiparticle interference in real space. **a**, Topograph on Sr_2RhO_4 on a field of view of $15\times15\,nm^2$. The setup conditions are ($V_b = -20\,meV$, $I_t = 600\,pA$). **b**, Conductance layer at $E = -20\,meV$ acquired simultaneously to the topograph in panel **a** with bias modulation amplitude $dV = 2\,meV$.

a chemisorbed CO molecule, where the carbon atom gets incorporated in the surface by replacing the apical oxygen atom. The cross-shaped defects show two possible orientations, depending on the rotation of the octahedra to which they are bound. In Fig. 6.3b, we show the conductance layer at $-20\,meV$ acquired simultaneously to the topograph in Fig. 6.3a, where quasiparticle interference is imaged in real space. The lattice defects obviously act as scattering centers, creating an interference pattern between the quasiparticles standing waves. Such an image contains quantitative information about the quasiparticles momenta and, therefore, the band structure, as already introduced in chapter 2.3. The easiest way to access this information is by taking two-dimensional Fourier transforms of the conductance layers, to create momentum space images of the quasiparticle scattering vectors $\mathbf{q}$.

In order to obtain high quality q-space images (i.e. high signal-to-noise ratio and resolution), one needs to scan over a bigger field of view than the one showed in Fig. 6.3, eventually reducing the real space resolution. We show an example of a spectroscopic map that is optimized for Fourier space analysis in Fig. 6.4. The field of view is $55\times55\,nm^2$ and it is measured with 288×288 pixels. Several lattice defects are visible on the topograph. They create a very rich QPI pattern in the conductance layers, as shown for the energy layer corresponding to the Fermi level in Fig. 6.4b.

In Fig. 6.4c, we plot the two-dimensional Fourier transform of Fig. 6.4b. The field of view is rotated by 45° in order to have the same orientation of ARPES data and theoretical calculations. Several features can be observed. The Bragg peaks corre-

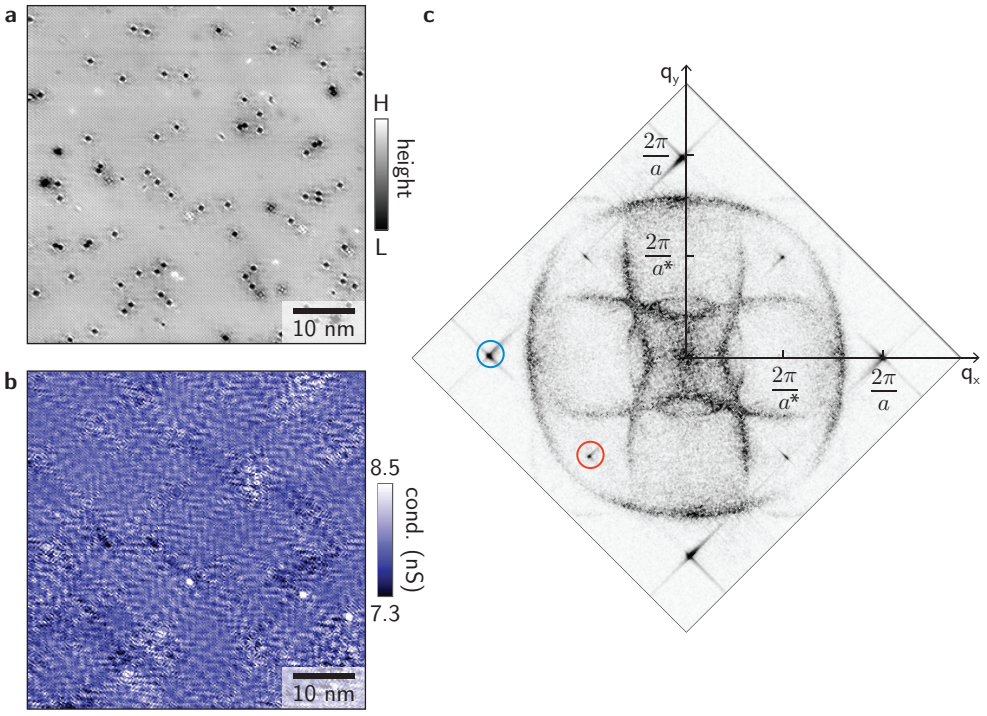

Figure 6.4: Spectroscopic map on Sr_2RhO_4. Field of view $55\times55\,nm^2$, 288×288 pixels. Setup conditions ($V_b = -50$ meV, $I_t = 500$ pA). **a**, Topograph. **b**, Conductance layer at E=0 meV, showing QPI in real space (raw data). **c**, Fourier transform of panel **b**, rotated by 45° (raw data). The Bragg peaks corresponding to the orthorhombic unit cell and to the Sr lattice periodicity are indicated with red and blue circles, respectively.

sponding to both the orthorhombic unit cell and the surface Sr lattice are indicated by the red and the blue circles, respectively. All the other features stem from quasiparticles scattering between high density of states areas of the Fermi surface, and their origin will be discussed in the rest of the chapter.

The image shown in Fig. 6.4c shows the raw Fourier transform. It is slightly distorted due to an asymmetry in the piezotube polarization and a slightly double tip, combined with a minimal thermal drift. Before extracting quantitative information from the data, we correct the images for the distortions. Additionally, we four-fold symmetrize the Fourier-transformed images, to remove residual asymmetries and improve the signal-to-noise ratio[3].

[3]To get an idea of how much distortion corrections and symmetrization change the Fourier transformed images, Fig. 6.4c (raw) should be compared with Fig. 6.6e (corrected).

6.4 Identification of scattering vectors: comparison with simulations

In order to analyze the origin of the features seen in the QPI measurements, we compute the autocorrelation of the Fermi surface, following the joint density of states (JDOS) approach introduced in section 2.3. In autocorrelation images, high intensity corresponds to scattering vectors that connect parallel regions of the Fermi surface, allowing a direct comparison with the STM q-space images.

To reproduce the Fermi surface measured with ARPES in Ref. [69], we compute the band structure from a minimal 2D tight-binding model adapted from Ref. [148]. It includes only the bands derived from the d_{xz} and d_{yz} orbitals, neglecting the γ band deriving from the d_{xy} orbital. The model uses two sublattices A, B to reproduce the band folding due to the octahedra rotation, and ignores next-nearest-neighbors hopping processes. The resulting 4×4 tight-binding hamiltonian is:

$$H = \begin{bmatrix} H_{SO} & H_{AB} \\ H_{AB}^{\dagger} & H_{SO} \end{bmatrix}, \tag{6.1}$$

where the on-site spin-orbit interaction H_{SO} and the nearest-neighbor hopping H_{AB} are given by

$$H_{SO} = \begin{bmatrix} 0 & i\lambda/2 \\ -i\lambda/2 & 0 \end{bmatrix}, \qquad H_{AB} = \begin{bmatrix} \epsilon_{yz} & \epsilon_{rot} \\ -\epsilon_{rot} & \epsilon_{xz} \end{bmatrix}. \tag{6.2}$$

Here, λ is the spin-orbit coupling constant, and it plays the role of mixing the d_{xz} and d_{yz} orbitals. The hopping is governed by the dispersions ϵ_{yz}, ϵ_{xz}, ϵ_{rot}, that are given by:

$$\epsilon_{yz} = -2t_{\pi}\cos(k_y) - 2t_{\delta}\cos(k_x), \tag{6.3}$$

$$\epsilon_{xz} = -2t_{\pi}\cos(k_x) - 2t_{\delta}\cos(k_y), \tag{6.4}$$

$$\epsilon_{rot} = -2t_{p}\cos(k_y) - 2t_{p}\cos(k_x). \tag{6.5}$$

Here, the terms t_{π} and t_{δ} represent hopping between identical orbitals on neighboring Rh sites (respectively, $yz \rightarrow yz$ and $xz \rightarrow xz$), while t_p allows hopping between different orbitals (e.g. $yz \rightarrow xz$) due to the octahedra rotation. The model has five parameters: the three hopping terms, the spin-orbit coupling and the Fermi energy: $(t_{\pi}, t_{\delta}, t_p, \lambda, E_F)$. We optimize the parameters in order to reproduce the ARPES band structure from Ref. [69], to obtain $(t_{\pi}, t_{\delta}, t_p, \lambda, E_F) = (0.104, 0.012, 0.0314, 0.14, 0.155)$.

By diagonalizing the hamiltonian in Eq. (6.1) with the given parameters, we obtain the tight-binding band structure. From the tight-binding constant energy contours,

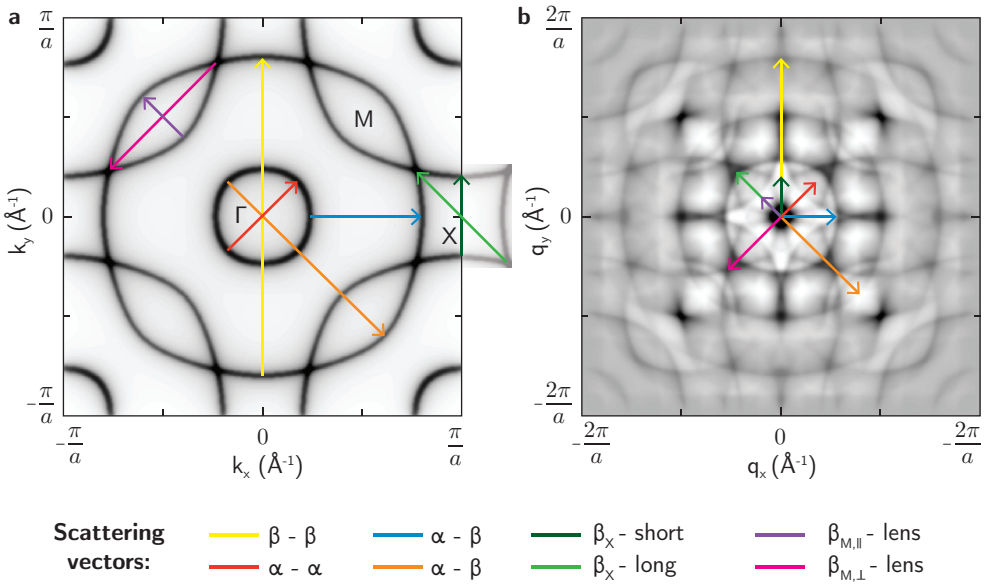

Figure 6.5: **a**, Simulated Fermi surface computed using the tight-binding model discussed in the main text. **b**, Autocorrelation of the Fermi surface in panel **a**. The main scattering vectors are indicated with the same color coding in both panels. Note the different axes.

we generate a rough simulated $A(\mathbf{k}, \omega)$. To reproduce ARPES experimental energy and momentum resolution, we add energy layers in an energy window corresponding to the ARPES energy resolution and we apply a Lorentzian smoothing in k-space.

The resulting simulated Fermi surface is shown in Fig. 6.5a. The most prominent scattering vectors are indicated by arrows. The main scattering vectors correspond to the $\alpha - \alpha$ (red) and $\beta - \beta$ (yellow) intraband scatterings and to two possibilities for the $\alpha - \beta$ interband scattering (orange and blue). In addition, we indicate vectors connecting the backfolded copies of the bands, within the lens-shaped β_M pocket (purple) and within the square-shaped β_X pocket (green).

In Fig. 6.5b, we show the computed autocorrelation from Fig. 6.5a, where the scattering vectors from the Fermi surface are identified by the same color coding. The autocorrelation shows much more details than the STM QPI data in Fig. 6.4c. This is probably because the simplistic autocorrelation approach neglects scattering probabilities due to matrix elements. It is, nevertheless, useful for the identification of the features seen in QPI data.

In order to have a more complete overview of the energy evolution, we show in Fig. 6.6 a selection of layers from the same spectroscopic map shown in Fig. 6.4. The data,

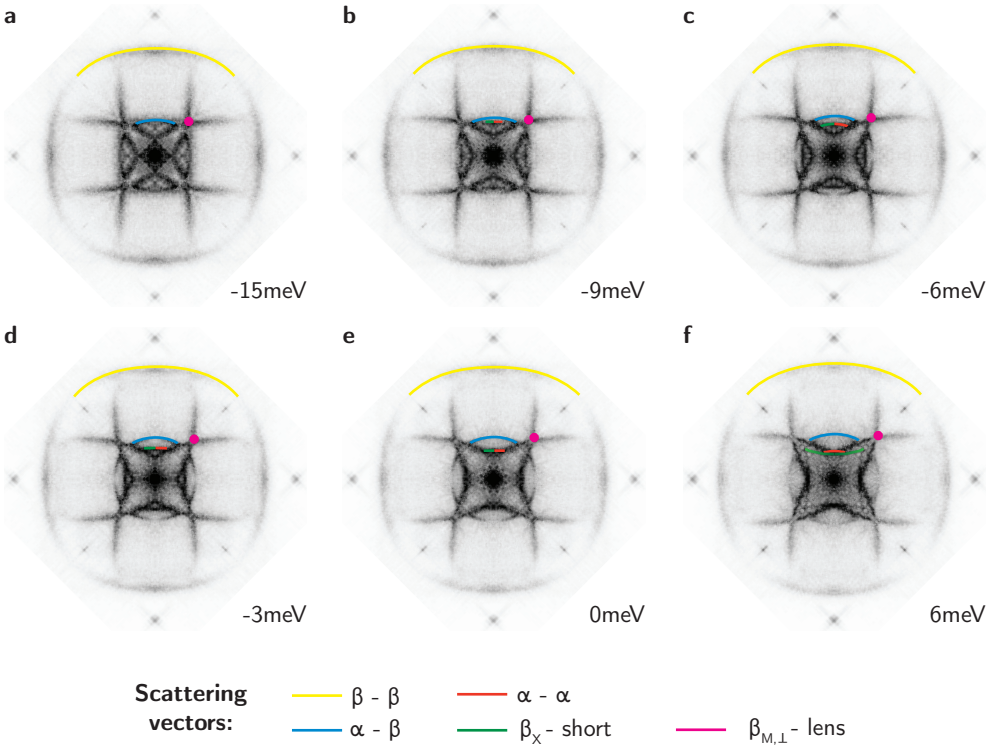

Figure 6.6: a-f Fourier transform of selected conductance layers of the same spectroscopic map shown in Fig. 6.4. The field of view is $55\times55\,\mathrm{nm}^2$, with 288×288 pixels. The setup conditions are ($V_b = -50$ meV, $I_t = 500$ pA), and the map has 11 energy layers between -15 meV and 15 meV spaced by 3 meV intervals. The real space data is corrected for drift and other distortions and the Fourier transform is 4-fold symmetrized to ease the visualization of the features.

here, is corrected for drift and piezotube miscalibration and additionally four-fold symmetrized to ease the identification.

From a careful comparison of the scattering vectors, we can identify several features in the QPI data in Fig. 6.6. The biggest circular feature corresponds to the $\beta - \beta$ intraband scattering. It grows in diameter with increasing energy, indicating its electron-like character. We can also identify the smaller $\alpha - \beta$ interband scattering (blue), while the bigger $\alpha - \beta$ interband scattering (orange arrow in Fig. 6.5) is completely absent from the QPI data. At small $\mathbf{q}$, we find the scattering vectors corresponding to the lens-shaped β_M electron pockets (magenta dot), also growing with increasing energy. The scattering vectors within the hole-like features (α and β_X pockets) are instead more difficult to identify. There is a clear signal of a hole-like feature along the ΓX direction that shrinks with energy. However it is not possible to discern whether it belongs to the α (red) or to the β_X (green) hole pocket, since along this direction

both pockets have very similar sizes, and where their shapes start to differ, the signal is partially hidden from the lens-shaped β_M pockets. We show in Sec. 6.5 that the two hole pockets can be distinguished along the ΓM direction.

6.5 Extraction of dispersions and Fermi vectors

To better characterize the dispersion of the scattering vectors, we take (E, **q**) cuts along the high symmetry directions ΓX and ΓM, as shown in Fig. 6.7 for two different measurements. Before taking the cuts, the Fourier transformed data is additionally smoothed with a small Gaussian window. The two maps have the same size and number of pixels ($55\times55\,nm^2$, 288×288 pixels), and are acquired on two different field of views about 100 nm apart from each other. They have different setup conditions (V_b, I_t) and energy ranges: (50 meV, 500 pA) and [−50 meV; 50 meV] for Fig. 6.7a-b versus (−50 meV, 500 pA) and [−15 meV; 15 meV] for Fig. 6.7c-d[4].

The main features in the cuts can be recognized as the dispersing scattering vectors that we identified in Sec. 6.4. In order to extract quantitative information, we individually plot every dispersion as intensity vs. momentum curves for all energies, as shown in Fig. 6.7f for the β_X scattering from Fig. 6.7c. This leads to the STM analogous of ARPES momentum distribution curves (MDCs). We can then fit the data with a gaussian curve summed with a linear background, to extract the peak position. The dispersion of all the scattering vectors extracted by fitting the peak positions are plotted in Fig. 6.7g-h for both the datasets in the two different directions. Sometimes the signal is not very clear, causing a considerable uncertainty in the determination of the peak position. This mostly happens when two dispersions cross each other or when they flatten out.

By fitting the dispersions with a linear curve (or with a parabolic curve for the α and β_X hole pockets), we can extract the magnitude q_F of all the q-vectors at the Fermi level. Moreover, for scattering within one single band, the Fermi velocity can be obtained from the slope of the fit. In the next section, we will compare both quantities with photoemission data.

[4] The cuts in Fig. 6.7c-d are extracted from the same measurement of which we showed conductance layers and Fourier transforms in Fig. 6.4 and Fig. 6.6.

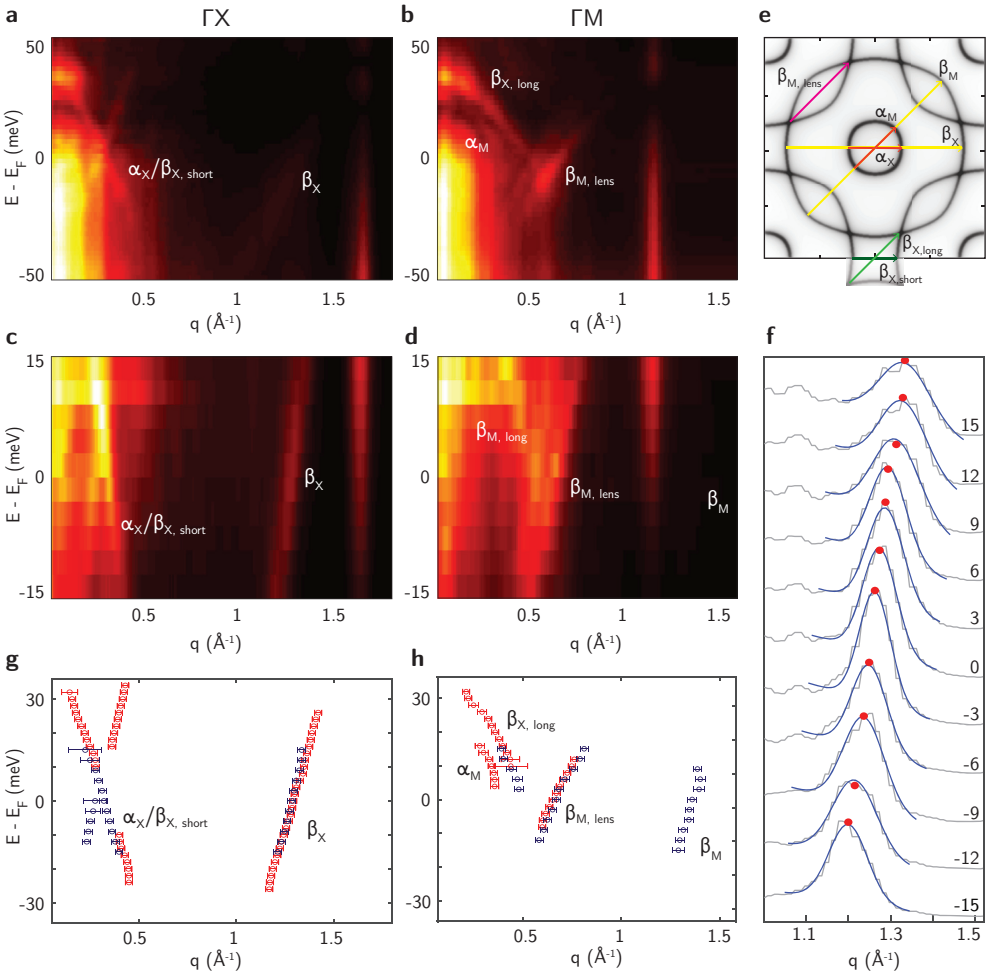

Figure 6.7: **a-b**, Cuts of a spectroscopic map with (V_b, I_t) = (50 meV, 500 pA) and energy range [-50 meV, 50 meV], along ΓX and ΓM directions. **c-d**, Cuts of a spectroscopic map with (V_b, I_t) = (-50 meV, 500 pA) and energy range [-15 meV, 15 meV], along ΓX and ΓM directions. **e**, Fermi surface from tight-binding model with identification of the main scattering vectors. **f**, Example of a gaussian fit to the QPI MDCs for the β_X scattering from panel **c**. The energies are indicated in meV units. **g-h**, Dispersions extracted from panels **a-b** (in red) and **c-d** (in blue) through fits analogous to the one shown in panel **f**. The error bars are the quadratic sum of the standard deviations extracted from the fit and the size of the smoothing window.

6.6 Comparison with ARPES

In Table 6.1, we compare the values obtained from STM data for q_F and v_F with the corresponding values obtained with ARPES in Ref. [69]. In general, we find very good agreement for what concerns the magnitude of the scattering vectors at the Fermi level, while the Fermi velocities agree less well. The values for the Fermi velocities obtained in the ΓM direction are not very reliable, due to poor S/N. However, also in the ΓX direction, where the STM signal is clear, the ARPES-derived value is about 10% larger.

In Fig. 6.8, we plot the superposition of our STM results with ARPES results from Ref. [68, 69], in order to have a further visual comparison. The STM q-axis are rescaled by a factor two, to coincide with the ARPES data.

In Fig. 6.8a, we compare the Fermi surfaces derived from ARPES and STM. We can obtain the Fermi surface for the β band from the STM data shown in Fig. 6.6e by fitting intensity profiles radially for several angles between ΓX and ΓM. We plot the values of k_F extracted in this way as datapoints above the measured ARPES Fermi surface. The two colors correspond to the two different measurements, with the respective standard deviations. The agreement is good in all directions.

		STM	ARPES
q_F (Å^{-1})	α_X	0.32*	0.32
	α_M	0.38	0.35
	β_X large	1.29	1.28
	β_M large	1.37	1.36
	β_X short	0.32*	0.34
	β_X long	0.53	0.52
	β_M lens	0.66	0.63
	$\alpha - \beta$	0.56	0.52
v_F (eV Å)	α_X	0.39*	0.41
	α_M	0.35**	0.41
	β_X short	0.39*	0.55
	β_X - large	0.46	0.55
	β_M - large	0.50**	0.61

Table 6.1: Comparison of scattering vectors q_F and velocities v_F at the Fermi level as obtained from STM (this study) and ARPES (Ref. [69]). The STM values, when possible, are averaged between the two datasets. The single asterisk indicates that the identification of the STM feature is uncertain, and could belong to both the α_X pocket and the β_X square pocket. The double asterisk indicates that the STM data is not fully reliable due to poor data quality.

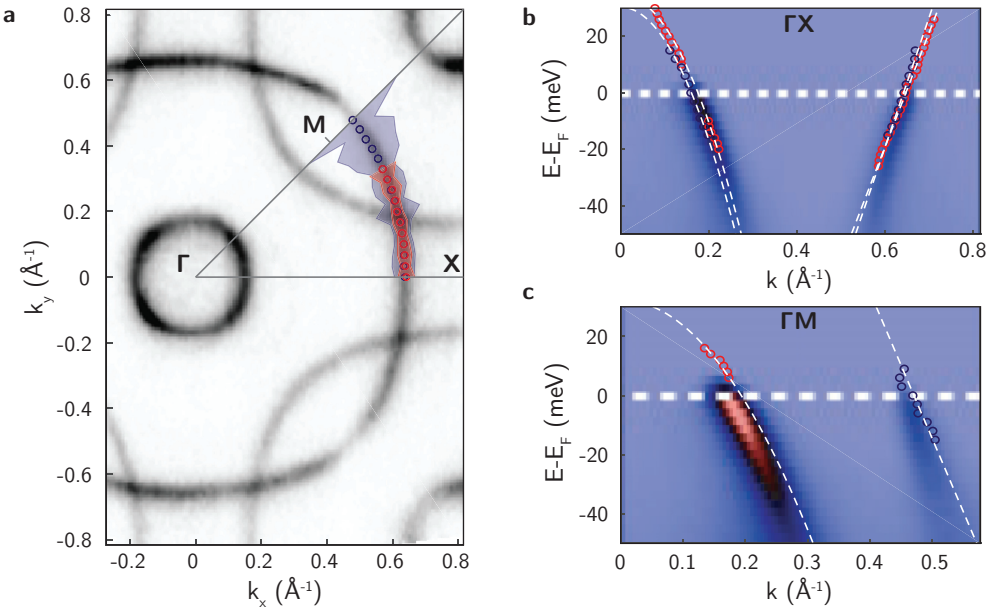

Figure 6.8: Comparison of STM and ARPES results. **a**, STM-derived Fermi surface (in circles) plotted over the ARPES Fermi surface (Ref. [69]). The STM points are obtained from radial cuts of the Fourier-transformed QPI signal between the ΓX and ΓM directions. The two STM datasets are given with different colors, and the shaded areas indicate the standard deviations. **b-c**, Superposition of the ARPES dispersions (adapted from Ref. [68]) and the STM dispersions in the ΓX and ΓM directions, respectively. The data points are indicated by circles with different colors for the two datasets, and the white dash lines are fits to the STM data. The STM dispersions are renormalized by dividing the k-axis by a factor two.

In Fig. 6.8b-c, we plot the comparison of the dispersions. For the STM data, we plot both the peak positions as in Fig. 6.7g-h and the linear or parabolic fits (white dashed lines) from which we extract the Fermi velocities. As already anticipated by the values in Table 6.1, the STM-derived dispersions are generally flatter than the ones obtained with ARPES. For what concerns the α band, the dispersions agree better, however, mostly in the ΓM direction, the STM dispersion is a bit displaced with respect to the ARPES data. For the β band, the dispersions clearly deviate from each other, with most differences visible along ΓM. As we already indicated before, along this direction the STM signal is suppressed, resulting in worse data quality.

A good agreement of the Fermi surface, but flatter STM dispersions with respect to the ARPES ones, have been encountered before, for instance on Sr_2RuO_4 [43] (which is a very similar system to Sr_2RhO_4) and on cuprates [18, 47]. For cuprates, some efforts have been made to understand the discrepancies [47]. It has been suggested that both tunneling and photoemission matrix elements could play a role. Indeed,

the dispersions agree better when ARPES experiments are performed with a photon polarization that suppresses states in the same direction as they are suppressed in STM [47].

To bring the comparison with ARPES further, one could try to extract the self energy from QPI data, as it is proposed in Ref. [149]. To do so, one needs to fit the STM MDCs with Lorentzian curves, and extract the position of the peaks and their width. However, data of outstanding quality is necessary for this type of analysis. We preliminary extracted the self energy for the β band, leading to results that are in rough agreement with ARPES. However, a more detailed analysis on better quality datasets is needed in order to draw firm conclusions.

6.7 Conclusions

We are certain that it is important to be able to compare STM with ARPES results. Both techniques have their own strengths, and combining their complementary results can lead to crucial insights into the understanding of quantum materials. However, we think that this combination is reliable only if the techniques deliver similar results when they measure the same quantities on simple materials, or if we understand well where possible discrepancies come from.

In this chapter, we show QPI measurements on the correlated metal Sr_2RhO_4, which seems like a good candidate to test the comparison between STM and ARPES. While the data quality and statistics is not yet good enough to come to sound conclusions, we obtain some promising, preliminary results.

We are able to identify all the features observed with STM as scattering between different areas of the Fermi surface, and we obtain very good agreement for the magnitude of the scattering vectors at the Fermi level. The values obtained for the Fermi velocities are instead agreeing less well with ARPES results. Interestingly, a comparable disagreement for the Fermi velocity is reported for Sr_2RuO_4 [43], which in many ways is a very similar system to Sr_2RhO_4. This might indicate a deeper origin for the disagreement, and further investigations on both systems could, for instance, indicate if they are due to the nature of the scatterers or to the measurement technique.

The quality of the Sr_2RhO_4 data presented here is possibly still affected by some measurement artifacts, and hence, we cannot yet infer the origin of this disagreement. We are planning further measurements that should lead to better results, in addition to more statistics. This will be achieved, for instance, by setting up the measurements at negative biases to avoid artifacts (following the suggestions of Ref. [150]), by reducing the energy resolution to 1.5 meV (best resolution achievable at 4.3 K), and eventually

by exploring a bigger negative energy range. Moreover, a better tip quality should help to get clearer data.

7

Conclusions and outlook

This thesis is dedicated to the study of strongly-correlated electron systems using spectroscopic-imaging scanning tunneling microscopy (SI-STM), with a focus on the physics of lightly doped Mott insulators.

We are convinced that the improvement of scientific apparatus is the foundation of new experimental discoveries. Thus, we designed and built a SI-STM (named *Dome*) that proofs to be the stiffest reported to date (chapter 3), which has direct consequences on the data quality in terms of signal-to-noise ratio. This makes the instrument particularly suited for sensitive quasiparticle interference measurements, as we show in chapter 6 on the correlated metal Sr_2RhO_4.

In parallel to the construction of this microscope, we studied the electron-doped iridate $(Sr_{1-x}La_x)_2IrO_4$ using a different, commercial STM. Our results, described in chapter 4 and 5, add important contributions to the understanding of the physics of lightly doped Mott insulators. In particular, we show that a pseudogap phase with inhomogeneous electronic order appears upon doping, similar to what it is observed in cuprates. It is the first time that these phenomena are observed in a material different that cuprates, and it shows that they are not unique to the copper oxide planes, but belong to a wider class of quasi two-dimensional Mott insulators. Based on this advanced comparison between iridates and cuprates, we support the claim that iridates should also show unconventional superconductivity at higher doping [87, 88].

Quasiparticle interference (QPI) lead to many insights into the understanding of both the pseudogap and the superconducting phase of cuprates [35, 151]. During our investigation of the iridates, we tried to get momentum space information, with the

goal to observe q-space signatures of the inhomogeneous charge order and, eventually, QPI. We were not successful, but we could identify two possible reasons: either the pseudogap puddles are too small, or the commercial STM that we used to measure the iridates cannot resolve those features since it is not very suited for QPI measurements. After having developed and tested a dedicated instrument such as Dome, it seems natural to bring the investigation on the iridates further by trying to detect QPI signatures on the iridates with Dome. The much higher signal-to-noise ratio could, in fact, reveal information that we were previously not able to resolve.

This is just one example of which type of measurements could be performed in the near future with Dome. To conclude this thesis, we give in the following other three more specific examples of experiments that could exploit the microscope's potential. The ideas we present are based on the two qualities that make the microscope 'special': first, the extreme stability that allows high-quality quasiparticle-interference measurements (as shown in chapter 3 and chapter 6), and, second, the high-frequency compatibility of the STM head (discussed in Sec. 3.2.1).

Investigation of the strange metal phase in cuprates

The strange metal phase in cuprates is still largely not understood, and much theoretical and experimental effort has been dedicated to its study in the recent years. In particular, theoretical work predicts STM QPI patterns in the strange metal phase both in the framework of Fermi-liquid and marginal-Fermi-liquid theory[1] in the presence of disorder [141].

SI-STM experiments as suggested in Ref. [141] are a good way to understand whether these descriptions are valid or not. In the case one observed the predicted pattern due to QPI, very precise measurements would be needed in order to distinguish the subtle effects that differentiate the proposed theoretical interpretations. On the other hand, observation of a completely different QPI pattern (or of no pattern at all), would indicate that this phase of matter is beyond the marginal Fermi-liquid description. This would point towards other theoretical interpretations, possibly involving quantum criticality and the absence of quasiparticle-like excitations. In recent years, a completely different approach based on holographic methods[2] was used to describe the properties of the strange metal phase [153, 154]. In general, however, more experimental data is needed to support any of the theoretical scenarios.

We believe that with our microscope we could contribute to a better understanding of the strange metal phase, given the high quality QPI measurements that we can achieve. In order to access the strange metal phase, one needs both to have sam-

[1] The phenomenological marginal Fermi liquid theory was first introduced by Varma et al. [152] and it successfully describes many of the unusual properties seen in the normal state of cuprates.

[2] These methods, indeed, do not involve quasiparticles.

ples in the right doping range and to raise the temperature above T_c. Since STM energy resolution gets worse at higher temperatures (see Sec. 2.5), and, in general, measurements become more challenging, we propose to study $Bi_2Sr_2Cu_2O_{6+\delta}$, the single layer compound of the BSCCO family. This material has a lower T_c at optimal doping ($T_c \approx 20\,\mathrm{K}$) than other members of the BSCCO family, which would make the strange metal phase accessible more easily. Our sample stage includes a resistive heater that we have already tested. We could measure 24h-long spectroscopic maps at 30 K without the observation of significant drift. This makes the exploration of the strange metal phase in $Bi_2Sr_2Cu_2O_{6+\delta}$, in principle, experimentally possible.

Other insights into the strange metal phase could come from the analysis of the self energies extracted from STM QPI data [155]. This method has been theoretically proposed [149], but has not been applied to data yet. We plan to first develop and apply the proposed data analysis methods onto the simpler system of Sr_2RhO_4 (described in chapter 6), and, if successful, proceed with STM self-energy analysis in cuprates, at low temperature and, eventually, in the strange metal phase.

Scanning noise spectroscopy

The other experiments we want to propose is based on the technique of *scanning noise spectroscopy*. This technique has recently been developed in our group, and, when first applied on cuprate high-T_c superconductors, it lead to interesting insights on the insulating nature of the material along the perpendicular 'c-axis' direction [59]. The technique is based on the development and construction of a new, low-temperature, high-frequency amplifier that allows us to measure the tunneling current in the MHz regime, simultaneously to conventional DC STM measurements [58]. This gives access to information about the current fluctuations (i.e., the noise) that are typically hidden in the 'averaged' DC current signal. Most prominently, it allows us to measure shot noise, which gives an indication of the nature of the charge carriers.

The amplifier has been developed in our group, and, to date, it has been optimized and used on a commercial STM from Unisoku [58]. We are currently at the last stages of construction and testing of a second generation amplifier that will be installed in Dome. One of the hindering factors for the quality of the high-frequency signal is the tip-to-ground capacitance. This number, on the order of 30 pF for the Unisoku system, can be reduced with a smart design of the tip holder (in fact, its origin mostly lies in the geometry of the latter). When designing the STM head for Dome, we worked towards achieving a very low tip-to-ground capacitance, as described in Sec. 3.2.1. This, combined with the superior stability of the microscope, should increase the signal-to-noise ratio of high-frequency measurements for Dome by a factor of three with respect to the Unisoku commercial system. This would enable noise spectroscopy measurements at much lower tunneling current ($\approx 50\,\mathrm{pA}$) than it is now possible,

making these experiments applicable to many more quasi two-dimensional layered materials.

In addition to further exploring cuprate high-T_c superconductors with scanning noise spectroscopy, we propose to apply this technique to the iridates described in chapter 4. Here, shot noise measurements could additionally reveal different behaviors in the Mott and pseudogap phases, bringing further insights on the nature of the carriers in both phases. In particular, in the Mott regime, an enhancement of the shot noise at the dopant locations could indicate charge trapping, confirming our proposed scenario of frozen electrons.

Shaking the condensate

The last experiment we want to propose regards the exploration of non-equilibrium superconductivity in cuprates. In other words, how is the superconducting state affected when the condensate is moving?

Our idea is based on a proposal by Semenov et al. [156], where they theoretically investigate the effect of applying a microwave field to BCS superconductors. At very low temperatures and with a microwave energy lower than the energy gap (to avoid direct Cooper pair breaking from microwaves), they find that the microwave field would lead to coherent, excited Cooper pairs with an oscillating center of mass motion. This would create a substantial modification of the single-particle density of states, that could be detected by tunneling spectroscopy experiments. We are excited by the possibility to investigate a similar scenario in cuprates.

Dome is provided with semirigid coaxial cables that allow for high-frequency measurements (up to a few GHz). Therefore it is technically possible and relatively simple to apply a microwave excitation to the sample while performing standard spectroscopic STM measurements. We investigated this possibility, and simulations predict that, with minor changes to the experimental setup, we would be able to induce the desired oscillating current densities in the sample. A closer look at the numbers reveals that we would need temperatures much lower than 4 K to observe the effect predicted by Ref. [156]. However, at 4 K, there could still be some detectable effect of microwaves on the coherence peaks of the superconducting gap. If we are able to detect this signature, it would be extremely interesting to see how its magnitude changes locally, given the electronically inhomogeneous landscape of cuprates. A different effect of microwaves on different areas would give insights on how the condensate is moving inside the material.

Bibliography

[1] N. W. Ashcroft, N. Mermin. *Solid State Physics*. Holt, Rinehart and Winston, New York (1976).

[2] J. Schrieffer. What is a quasi-particle? *J. Res. Natl. Bur. Stand. Sect. A Phys. Chem.* **74A**, 537 (1970).

[3] P. W. Anderson. More Is Different. *Science* **177**, 393–396 (1972).

[4] K. Fujita, M. Hamidian, I. Firmo, S. Mukhopadhyay, C. K. Kim, H. Eisaki, S.-I. Uchida, J. C. Davis. Spectroscopic Imaging STM: Atomic-Scale Visualization of Electronic Structure and Symmetry in Underdoped Cuprates. In *Theor. Methods Strongly Correl. Syst.*, chap. 3, 73–109. Springer Berlin Heidelberg (2015).

[5] N. F. Mott. *Metal-Insulator Transitions*. Taylor & Francis, London (1990).

[6] M. Imada, A. Fujimori, Y. Tokura. Metal-insulator transitions. *Rev. Mod. Phys.* **70**, 1039–1263 (1998).

[7] D. I. Khomskii. *Transition metal compounds*. Cambridge University Press(2014).

[8] G. Kotliar, D. Vollhardt. Strongly Correlated Materials: Insights From Dynamical Mean-Field Theory. *Phys. Today* **57**, 53–59 (2004).

[9] P. A. Lee, N. Nagaosa, X.-G. Wen. Doping a Mott insulator: Physics of high-temperature superconductivity. *Rev. Mod. Phys.* **78**, 17–85 (2006).

[10] J. Bednorz, K. Müller. Possible High-T_c Superconductivity in the BaLaCu0 System. *Z.Phys.B-Condensed Matter* **64**, 189–193 (1986).

[11] B. Keimer, S. A. Kivelson, M. R. Norman, S. Uchida, J. Zaanen. From quantum matter to high-temperature superconductivity in copper oxides. *Nature* **518**, 179–186 (2015).

[12] N. P. Armitage, P. Fournier, R. L. Greene. Progress and perspectives on electron-doped cuprates. *Rev. Mod. Phys.* **82**, 2421–2487 (2010).

[13] E. Fradkin, S. A. Kivelson, J. M. Tranquada. Colloquium: Theory of intertwined orders in high temperature superconductors. *Rev. Mod. Phys.* **87**, 457–482 (2015).

[14] N. E. Hussey, K. Takenaka, H. Takagi. Universality of the Mott–Ioffe–Regel limit in metals. *Philos. Mag.* **84**, 2847–2864 (2004).

[15] C. Howald, P. Fournier, A. Kapitulnik. Inherent inhomogeneities in tunneling spectra of $Bi_2Sr_2CaCu_2O_{8-x}$ crystals in the superconducting state. *Phys. Rev. B* **64**, 100504 (2001).

[16] K. M. Lang, V. Madhavan, J. E. Hoffman, E. W. Hudson, H. Eisaki, S. Uchida, J. C. Davis. Imaging the granular structure of high-Tc superconductivity in underdoped $Bi_2Sr_2CaCu_2O_{8+\delta}$. *Nature* **415**, 412–416 (2002).

[17] K. McElroy. Atomic-Scale Sources and Mechanism of Nanoscale Electronic Disorder in $Bi_2Sr_2CaCu_2O_{8+\delta}$. *Science* **309**, 1048–1052 (2005).

[18] J. E. Hoffman. Imaging Quasiparticle Interference in $Bi_2Sr_2CaCu_2O_{8+\delta}$. *Science* **297**, 1148–1151 (2002).

[19] Y. Kohsaka, C. Taylor, K. Fujita, A. Schmidt, C. Lupien, T. Hanaguri, M. Azuma, M. Takano, H. Eisaki, H. Takagi, S. Uchida, J. C. Davis. An Intrinsic Bond-Centered Electronic Glass with Unidirectional Domains in Underdoped Cuprates. *Science* **315**, 1380–1385 (2007).

[20] M. J. Lawler, K. Fujita, J. Lee, A. R. Schmidt, Y. Kohsaka, C. K. Kim, H. Eisaki, S. Uchida, J. C. Davis, J. P. Sethna, E.-A. Kim. Intra-unit-cell electronic nematicity of the high-Tc copper-oxide pseudogap states. *Nature* **466**, 347–351 (2010).

[21] D. Griffiths. *Introduction to quantum mechanics.* Cambridge University Press, second ed. (2016).

[22] G. Binnig, H. Rohrer. Scanning Tunneling Microscopy - from Birth to Adolescence (Nobel Lecture). *Angew. Chemie Int. Ed. English* **26**, 606–614 (1987).

[23] R. M. Feenstra, J. Stroscio, A. Fein. Tunneling spectroscopy of the Si(111)2×1 surface. *J. Vac. Sci. Technol. B* **5**, 295–306 (1987).

[24] M. Crommie, C. Lutz, D. Eigler. Imaging standing waves in a 2D electron gas. *Nature* **363**, 524–527 (1993).

[25] L. Petersen, P. T. Sprunger, P. Hofmann, E. Lægsgaard, B. G. Briner, M. Doering, H.-P. Rust, A. M. Bradshaw, F. Besenbacher, E. W. Plummer. Direct imaging of the two-dimensional Fermi contour: Fourier-transform STM. *Phys. Rev. B* **57**, R6858–R6861 (1998).

[26] S. H. Pan, E. W. Hudson, J. C. Davis. Vacuum tunneling of superconducting quasiparticles from atomically sharp scanning tunneling microscope tips. *Appl. Phys. Lett.* **73**, 2992–2994 (1998).

[27] S. H. Pan, E. W. Hudson, K. M. Lang, H. Eisaki, S. Uchida, J. C. Davis. Imaging the effects of individual zinc impurity atoms on superconductivity in $Bi_2Sr_2CaCu_2O_8$. *Nature* **403**, 746–750 (2000).

[28] E. W. Hudson, K. M. Lang, V. Madhavan, S. H. Pan, H. Eisaki, S. Uchida, J. C. Davis. Interplay of magnetism and high-T_c superconductivity at individual Ni impurity atoms in $Bi_2Sr_2CaCu_2O_{8+\delta}$. *Nature* **411**, 920–924 (2001).

[29] C. J. Chen. *Introduction to Scanning Tunneling Microscopy.* Oxford University Press, first ed. (2000).

[30] J. E. Hoffman. Spectroscopic scanning tunneling microscopy insights into Fe-based superconductors. *Reports Prog. Phys.* **74**, 124513 (2011).

[31] H. Bruus, K. Flensberg. *Many-body quantum theory in condensed matter physics.* Oxford University Press, New York (2004).

[32] P. Coleman. *Introduction to many-body physics.* Cambridge University Press (2015).

[33] P. Abbamonte, E. Demler, J. Séamus Davis, J.-C. Campuzano. Resonant soft X-ray scattering, stripe order, and the electron spectral function in cuprates. *Phys. C Supercond.* **481**, 15–22 (2012).

[34] K. McElroy, R. W. Simmonds, J. E. Hoffman, D.-H. Lee, J. Orenstein, H. Eisaki, S. Uchida, J. C. Davis. Relating atomic-scale electronic phenomena to wave-like quasiparticle states in superconducting $Bi_2Sr_2CaCu_2O_{8+\delta}$. *Nature* **422**, 592–596 (2003).

[35] K. Fujita, C. K. Kim, I. Lee, J. Lee, M. H. Hamidian, I. A. Firmo, S. Mukhopadhyay, H. Eisaki, S. Uchida, M. J. Lawler, E.-A. Kim, J. C. Davis. Simultaneous Transitions in Cuprate Momentum-Space Topology and Electronic Symmetry Breaking. *Science* **344**, 612–616 (2014).

[36] M. P. Allan, K. Lee, A. W. Rost, M. H. Fischer, F. Massee, K. Kihou, C.-H. Lee, A. Iyo, H. Eisaki, T.-M. Chuang, J. C. Davis, E.-A. Kim. Identifying the 'fingerprint' of antiferromagnetic spin fluctuations in iron pnictide superconductors. *Nat. Phys.* **11**, 177–182 (2015).

[37] B. B. Zhou, S. Misra, E. H. Da Silva Neto, P. Aynajian, R. E. Baumbach, J. D. Thompson, E. D. Bauer, A. Yazdani. Visualizing nodal heavy fermion superconductivity in $CeCoIn_5$. *Nat. Phys.* **9**, 474–479 (2013).

[38] M. P. Allan, F. Massee, D. K. Morr, J. Van Dyke, A. W. Rost, A. P. Mackenzie, C. Petrovic, J. C. Davis. Imaging Cooper pairing of heavy fermions in $CeCoIn_5$. *Nat. Phys.* **9**, 468–473 (2013).

[39] P. Roushan, J. Seo, C. V. Parker, Y. S. Hor, D. Hsieh, D. Qian, A. Richardella, M. Z. Hasan, R. J. Cava, A. Yazdani. Topological surface states protected from backscattering by chiral spin texture. *Nature* **460**, 1106–1109 (2009).

[40] H. Inoue, A. Gyenis, Z. Wang, J. Li, S. W. Oh, S. Jiang, N. Ni, B. A. Bernevig, A. Yazdani. Quasiparticle interference of the Fermi arcs and surface-bulk connectivity of a Weyl semimetal. *Science* **351**, 1184–1187 (2016).

[41] A. Gyenis, H. Inoue, S. Jeon, B. B. Zhou, B. E. Feldman, Z. Wang, J. Li, S. Jiang, Q. D. Gibson, S. K. Kushwaha, J. W. Krizan, N. Ni, R. J. Cava, B. A. Bernevig, A. Yazdani. Imaging electronic states on topological semimetals using scanning tunneling microscopy. *New J. Phys.* **18**, 105003 (2016).

[42] P. Sessi, V. M. Silkin, I. A. Nechaev, T. Bathon, L. El-Kareh, E. V. Chulkov, P. M. Echenique, M. Bode. Direct observation of many-body charge density

oscillations in a two-dimensional electron gas. *Nat. Commun.* **6**, 8691 (2015).

[43] Z. Wang, D. Walkup, P. Derry, T. Scaffidi, M. Rak, S. Vig, A. Kogar, I. Zeljkovic, A. Husain, L. H. Santos, Y. Wang, A. Damascelli, Y. Maeno, P. Abbamonte, E. Fradkin, V. Madhavan. Quasiparticle interference and strong electron–mode coupling in the quasi-one-dimensional bands of Sr_2RuO_4. *Nat. Phys.* **13**, 799–805 (2017).

[44] A. Damascelli, Z. Hussain, Z.-X. Shen. Angle-resolved photoemission studies of the cuprate superconductors. *Rev. Mod. Phys.* **75**, 473–541 (2003).

[45] R. S. Markiewicz. Bridging k and q space in the cuprates: Comparing angle-resolved photoemission and STM results. *Phys. Rev. B* **69**, 214517 (2004).

[46] U. Chatterjee, M. Shi, A. Kaminski, A. Kanigel, H. M. Fretwell, K. Terashima, T. Takahashi, S. Rosenkranz, Z. Z. Li, H. Raffy, A. Santander-Syro, K. Kadowaki, M. R. Norman, M. Randeria, J. C. Campuzano. Nondispersive Fermi Arcs and the Absence of Charge Ordering in the Pseudogap Phase of $Bi_2Sr_2CaCu_2O_{8+\delta}$. *Phys. Rev. Lett.* **96**, 107006 (2006).

[47] K. McElroy, G.-H. Gweon, S. Y. Zhou, J. Graf, S. Uchida, H. Eisaki, H. Takagi, T. Sasagawa, D.-H. Lee, A. Lanzara. Elastic Scattering Susceptibility of the High Temperature Superconductor $Bi_2Sr_2CaCu_2O_{8+\delta}$: A Comparison between Real and Momentum Space Photoemission Spectroscopies. *Phys. Rev. Lett.* **96**, 067005 (2006).

[48] R. M. Feenstra, J. Y. Lee, M. H. Kang, G. Meyer, K. H. Rieder. Band gap of the Ge(111)c(2×8) surface by scanning tunneling spectroscopy. *Phys. Rev. B* **73**, 035310 (2006).

[49] R. M. Feenstra, Y. Dong, M. P. Semtsiv, W. T. Masselink. Influence of tip-induced band bending on tunneling spectra of semiconductor surfaces. *Nanotechnology* **18**, 044015 (2007).

[50] M. Weimer, J. Kramar, J. Baldeschwieler. Band bending and the apparent barrier height in scanning tunneling microscopy. *Phys. Rev. B* **39**, 5572 (1989).

[51] R. Feenstra. SEMITIP v6 (2011).

[52] S. C. White, U. R. Singh, P. Wahl. A stiff scanning tunneling microscopy head for measurement at low temperatures and in high magnetic fields. *Rev. Sci. Instrum.* **82**, 113708 (2011).

[53] S. H. Pan, E. W. Hudson, J. C. Davis. ^{3}He refrigerator based very low temperature scanning tunneling microscope. *Rev. Sci. Instrum.* **70**, 1459–1463 (1999).

[54] F. Pobell. *Matter and Methods at Low Temperatures.* Springer Berlin Heidelberg, 3rd ed. (2007).

[55] R. J. Hussey, J. Wilson. *Advanced Technical Ceramics Directory and Databook.* Springer (2012).

[56] A. L. Woodcraft, A. Gray. A low temperature thermal conductivity database. In *Low Temp. Detect. LTD 13*, 681–684 (2009).

[57] NIST. NIST online cryogenic database. Tech. rep., National Institute of Standards and Technology (2018).

[58] K. M. Bastiaans, T. Benschop, D. Chatzopoulos, D. Cho, Q. Dong, Y. Jin, M. P. Allan. Amplifier for scanning tunneling microscopy at MHz frequencies. *Rev. Sci. Instrum.* **89**, 093709 (2018).

[59] K. M. Bastiaans, D. Cho, T. Benschop, I. Battisti, Y. Huang, M. S. Golden, Q. Dong, Y. Jin, J. Zaanen, M. P. Allan. Charge trapping and super-Poissonian noise centres in a cuprate superconductor. *Nat. Phys.* **14**, 1183–1187 (2018).

[60] COMSOL AB. COMSOL Multiphysics 5.2 (2015).

[61] J. H. Kindt, G. E. Fantner, J. A. Cutroni, P. K. Hansma. Rigid design of fast scanning probe microscopes using finite element analysis. *Ultramicroscopy* **100**, 259–265 (2004).

[62] C. R. Ast, M. Assig, A. Ast, K. Kern. Design criteria for scanning tunneling microscopes to reduce the response to external mechanical disturbances. *Rev. Sci. Instrum.* **79**, 093704 (2008).

[63] J. Maess, A. J. Fleming, F. Allgöwer. Simulation of dynamics-coupling in piezoelectric tube scanners by reduced order finite element analysis. *Rev. Sci. Instrum.* **79**, 015105 (2008).

[64] C. Braunsmann, T. E. Schäffer. High-speed atomic force microscopy for large scan sizes using small cantilevers. *Nanotechnology* **21**, 225705 (2010).

[65] M. J. Rost, L. Crama, P. Schakel, E. van Tol, G. B. E. M. van Velzen-Williams, C. F. Overgauw, H. ter Horst, H. Dekker, B. Okhuijsen, M. Seynen, A. Vijftigschild, P. Han, A. J. Katan, K. Schoots, R. Schumm, W. van Loo,T. H. Oosterkamp, J. W. M. Frenken. Scanning probe microscopes go video rate and beyond. *Rev. Sci. Instrum.* **76**, 053710 (2005).

[66] M. J. Rost, G. J. C. van Baarle, A. J. Katan, W. M. van Spengen, P. Schakel, W. A. van Loo, T. H. Oosterkamp, J. W. M. Frenken. Video-rate scanning probe control challenges: setting the stage for a microscopy revolution. *Asian J. Control* **11**, 110–129 (2009).

[67] Y. I. Yanson, F. Schenkel, M. J. Rost. Design of a high-speed electrochemical scanning tunneling microscope. *Rev. Sci. Instrum.* **84**, 023702 (2013).

[68] R. S. Perry, F. Baumberger, L. Balicas, N. Kikugawa, N. J. C. Ingle, A. Rost, J. F. Mercure, Y. Maeno, Z. X. Shen, A. P. Mackenzie. Sr_2RhO_4: a new, clean correlated electron metal. *New J. Phys.* **8**, 175 (2006).

[69] F. Baumberger, N. J. C. Ingle, W. Meevasana, K. M. Shen, D. H. Lu, R. S. Perry, A. P. Mackenzie, Z. Hussain, D. J. Singh, Z.-X. Shen. Fermi Surface and Quasiparticle Excitations of Sr_2RhO_4. *Phys. Rev. Lett.* **96**, 246402 (2006).

[70] T. Craig. *Imaging Interacting Electrons in Sr_2RhO_4.* Msc thesis, University of St. Andrews (2012).

[71] B. J. Kim, H. Jin, S. J. Moon, J.-Y. Kim, B.-G. Park, C. S. Leem, J. Yu, T. W. Noh, C. Kim, S.-J. Oh, J.-H. Park, V. Durairaj, G. Cao, E. Rotenberg. Novel

J_{eff}=1/2 Mott State Induced by Relativistic Spin-Orbit Coupling in Sr_2IrO_4. *Phys. Rev. Lett.* **101**, 076402 (2008).

[72] J. G. Rau, E. K.-H. Lee, H.-Y. Kee. Spin-Orbit Physics Giving Rise to Novel Phases in Correlated Systems: Iridates and Related Materials. *Annu. Rev. Condens. Matter Phys.* **7**, 195–221 (2016).

[73] S. J. Moon, H. Jin, K. W. Kim, W. S. Choi, Y. S. Lee, J. Yu, G. Cao, A. Sumi, H. Funakubo, C. Bernhard, T. W. Noh. Dimensionality-Controlled Insulator-Metal Transition and Correlated Metallic State in $Sr_{n+1}Ir_nO_{3n+1}$. *Phys. Rev. Lett.* **101**, 226402 (2008).

[74] H. Watanabe, T. Shirakawa, S. Yunoki. Microscopic Study of a Spin-Orbit-Induced Mott Insulator in Ir Oxides. *Phys. Rev. Lett.* **105**, 216410 (2010).

[75] C. Martins, M. Aichhorn, L. Vaugier, S. Biermann. Reduced Effective Spin-Orbital Degeneracy and Spin-Orbital Ordering in Paramagnetic Transition-Metal Oxides: Sr_2IrO_4 vs Sr_2RhO_4. *Phys. Rev. Lett.* **107**, 266404 (2011).

[76] J. H. Seo, G. H. Ahn, S. J. Song, X. Chen, S. D. Wilson, S. J. Moon. Infrared probe of pseudogap in electron-doped Sr_2IrO_4. *Sci. Rep.* **7**, 10494 (2017).

[77] B. H. Kim, G. Khaliullin, B. I. Min. Magnetic Couplings, Optical Spectra, and Spin-Orbit Exciton in 5d Electron Mott Insulator Sr_2IrO_4. *Phys. Rev. Lett.* **109**, 167205 (2012).

[78] Q. Wang, Y. Cao, J. A. Waugh, S. R. Park, T. F. Qi, O. B. Korneta, G. Cao, D. S. Dessau. Dimensionality-controlled Mott transition and correlation effects in single-layer and bilayer perovskite iridates. *Phys. Rev. B* **87**, 245109 (2013).

[79] A. de la Torre, S. McKeown Walker, F. Y. Bruno, S. Riccó, Z. Wang, I. Gutierrez Lezama, G. Scheerer, G. Giriat, D. Jaccard, C. Berthod, T. K. Kim, M. Hoesch, E. C. Hunter, R. S. Perry, A. Tamai, F. Baumberger. Collapse of the Mott Gap and Emergence of a Nodal Liquid in Lightly Doped Sr_2IrO_4. *Phys. Rev. Lett.* **115**, 176402 (2015).

[80] V. Brouet, J. Mansart, L. Perfetti, C. Piovera, I. Vobornik, P. Le Fèvre, F. Bertran, S. C. Riggs, M. C. Shapiro, P. Giraldo-Gallo, I. R. Fisher. Transfer of spectral weight across the gap of Sr_2IrO_4 induced by La doping. *Phys. Rev. B* **92**, 081117 (2015).

[81] B. J. Kim, H. Ohsumi, T. Komesu, S. Sakai, T. Morita, H. Takagi, T. Arima. Phase-Sensitive Observation of a Spin-Orbital Mott State in Sr_2IrO_4. *Science* **323**, 1329–1332 (2009).

[82] J. Kim, D. Casa, M. H. Upton, T. Gog, Y.-J. Kim, J. F. Mitchell, M. van Veenendaal, M. Daghofer, J. van den Brink, G. Khaliullin, B. J. Kim. Magnetic Excitation Spectra of Sr_2IrO_4 Probed by Resonant Inelastic X-Ray Scattering: Establishing Links to Cuprate Superconductors. *Phys. Rev. Lett.* **108**, 177003 (2012).

[83] X. Chen, J. L. Schmehr, Z. Islam, Z. Porter, E. Zoghlin, K. Finkelstein, J. P. C. Ruff, S. D. Wilson. Unidirectional spin density wave state in metallic

$(Sr_{1-x}La_x)_2IrO_4$. *Nat. Commun.* **9**, 103 (2018).

[84] J. Dai, E. Calleja, G. Cao, K. McElroy. Local density of states study of a spin-orbit-coupling induced Mott insulator Sr_2IrO_4. *Phys. Rev. B* **90**, 041102 (2014).

[85] J. Nichols, N. Bray-Ali, A. Ansary, G. Cao, K.-W. Ng. Tunneling into the Mott insulator Sr_2IrO_4. *Phys. Rev. B* **89**, 085125 (2014).

[86] Q. Li, G. Cao, S. Okamoto, J. Yi, W. Lin, B. C. Sales, J. Yan, R. Arita, J. Kuneš, A. V. Kozhevnikov, A. G. Eguiluz, M. Imada, Z. Gai, M. Pan, D. G. Mandrus. Atomically resolved spectroscopic study of Sr_2IrO_4: Experiment and theory. *Sci. Rep.* **3**, 3073 (2013).

[87] F. Wang, T. Senthil. Twisted Hubbard Model for Sr_2IrO_4: Magnetism and Possible High Temperature Superconductivity. *Phys. Rev. Lett.* **106**, 136402 (2011).

[88] H. Watanabe, T. Shirakawa, S. Yunoki. Monte Carlo Study of an Unconventional Superconducting Phase in Iridium Oxide $J_{eff}=1/2$ Mott Insulators Induced by Carrier Doping. *Phys. Rev. Lett.* **110**, 027002 (2013).

[89] O. B. Korneta, T. Qi, S. Chikara, S. Parkin, L. E. De Long, P. Schlottmann, G. Cao. Electron-doped $Sr_2IrO_{4-\delta}$: Evolution of a disordered $J_{eff}=1/2$ Mott insulator into an exotic metallic state. *Phys. Rev. B* **82**, 115117 (2010).

[90] Y. Klein, I. Terasaki. Insight on the electronic state of Sr_2IrO_4 revealed by cationic substitutions. *J. Phys. Condens. Matter* **20**, 295201 (2008).

[91] M. Ge, T. F. Qi, O. B. Korneta, D. E. De Long, P. Schlottmann, W. P. Crummett, G. Cao. Lattice-driven magnetoresistivity and metal-insulator transition in single-layered iridates. *Phys. Rev. B* **84**, 100402 (2011).

[92] X. Chen, T. Hogan, D. Walkup, W. Zhou, M. Pokharel, M. Yao, W. Tian, T. Z. Ward, Y. Zhao, D. Parshall, C. Opeil, J. W. Lynn, V. Madhavan, S. D. Wilson. Influence of electron doping on the ground state of $(Sr_{1-x}La_x)_2IrO_4$. *Phys. Rev. B* **92**, 075125 (2015).

[93] Y. K. Kim, O. Krupin, J. D. Denlinger, A. Bostwick, E. Rotenberg, Q. Zhao, J. F. Mitchell, J. W. Allen, B. J. Kim. Fermi arcs in a doped pseudospin-1/2 Heisenberg antiferromagnet. *Science* **345**, 187–190 (2014).

[94] Y. J. Yan, M. Q. Ren, H. C. Xu, B. P. Xie, R. Tao, H. Y. Choi, N. Lee, Y. J. Choi, T. Zhang, D. L. Feng. Electron-Doped Sr_2IrO_4: An Analogue of Hole-Doped Cuprate Superconductors Demonstrated by scanning tunneling microscopy. *Phys. Rev. X* **5**, 041018 (2015).

[95] Y. K. Kim, N. H. Sung, J. D. Denlinger, B. J. Kim. Observation of a d-wave gap in electron-doped Sr_2IrO_4. *Nat. Phys.* **12**, 37–41 (2016).

[96] K. Wang, N. Bachar, J. Teyssier, W. Luo, C. W. Rischau, G. Scheerer, A. de la Torre, R. S. Perry, F. Baumberger, D. van der Marel. Mott transition and collective charge pinning in electron doped Sr_2IrO_4. *Phys. Rev. B* **98**, 045107 (2018).

[97] Y. Ando, A. N. Lavrov, S. Komiya, K. Segawa, X. F. Sun. Mobility of the Doped Holes and the Antiferromagnetic Correlations in Underdoped High-T_c Cuprates. *Phys. Rev. Lett.* **87**, 017001 (2001).

[98] Y. Okada, D. Walkup, H. Lin, C. Dhital, T.-R. Chang, S. Khadka, W. Zhou, H.-T. Jeng, M. Paranjape, A. Bansil, Z. Wang, S. D. Wilson, V. Madhavan. Imaging the evolution of metallic states in a correlated iridate. *Nat. Mater.* **12**, 707–713 (2013).

[99] I. Zeljkovic, Z. Xu, J. Wen, G. Gu, R. S. Markiewicz, J. E. Hoffman. Imaging the Impact of Single Oxygen Atoms on Superconducting $Bi_{2+y}Sr_{2-y}CaCu_2O_{8+x}$. *Science* **337**, 320–323 (2012).

[100] C. Ye, P. Cai, R. Yu, X. Zhou, W. Ruan, Q. Liu, C. Jin, Y. Wang. Visualizing the atomic-scale electronic structure of the $Ca_2CuO_2Cl_2$ Mott insulator. *Nat. Commun.* **4**, 1365 (2013).

[101] P. Cai, W. Ruan, Y. Peng, C. Ye, X. Li, Z. Hao, X. Zhou, D.-H. Lee, Y. Wang. Visualizing the evolution from the Mott insulator to a charge-ordered insulator in lightly doped cuprates. *Nat. Phys.* **12**, 1047–1051 (2016).

[102] Y. Kohsaka, K. Iwaya, S. Satow, T. Hanaguri, M. Azuma, M. Takano, H. Takagi. Imaging Nanoscale Electronic Inhomogeneity in the Lightly Doped Mott Insulator $Ca_{2-x}Na_xCuO_2Cl_2$. *Phys. Rev. Lett.* **93**, 097004 (2004).

[103] Y. Kohsaka, T. Hanaguri, M. Azuma, M. Takano, J. C. Davis, H. Takagi. Visualization of the emergence of the pseudogap state and the evolution to superconductivity in a lightly hole-doped Mott insulator. *Nat. Phys.* **8**, 534–538 (2012).

[104] J. W. Alldredge, J. Lee, K. McElroy, M. Wang, K. Fujita, Y. Kohsaka, C. Taylor, H. Eisaki, S. Uchida, P. J. Hirschfeld, J. C. Davis. Evolution of the electronic excitation spectrum with strongly diminishing hole density in superconducting $Bi_2Sr_2CaCu_2O_{8+\delta}$. *Nat. Phys.* **4**, 319–326 (2008).

[105] H. Wang, S.-L. Yu, J.-X. Li. Fermi arcs, pseudogap, and collective excitations in doped Sr_2IrO_4: A generalized fluctuation exchange study. *Phys. Rev. B* **91**, 165138 (2015).

[106] A. Moutenet, A. Georges, M. Ferrero. Pseudogap and electronic structure of electron-doped Sr_2IrO_4. *Phys. Rev. B* **97**, 155109 (2018).

[107] C. V. Parker, P. Aynajian, E. H. da Silva Neto, A. Pushp, S. Ono, J. Wen, Z. Xu, G. Gu, A. Yazdani. Fluctuating stripes at the onset of the pseudogap in the high-Tc superconductor $Bi_2Sr_2CaCu_2O_{8+x}$. *Nature* **468**, 677–680 (2010).

[108] R. Comin, A. Damascelli. Resonant X-Ray Scattering Studies of Charge Order in Cuprates. *Annu. Rev. Condens. Matter Phys.* **7**, 369–405 (2016).

[109] S. H. Simon. *The Oxford Solid State Basics.* Oxford University Press (2013).

[110] X. Blase, E. Bustarret, C. Chapelier, T. Klein, C. Marcenat. Superconducting group-IV semiconductors. *Nat. Mater.* **8**, 375–382 (2009).

[111] N. F. Mott. The metal-insulator transition in an impurity band. *Le J. Phys. Colloq.* **37**, C4–301–C4–306 (1976).

[112] M. A. Kastner, R. J. Birgeneau, G. Shirane, Y. Endoh. Magnetic, transport, and optical properties of monolayer copper oxides. *Rev. Mod. Phys.* **70**, 897–928 (1998).

[113] V. I. Anisimov, M. A. Korotin, J. Zaanen, O. K. Andersen. Spin bags, polarons, and impurity potentials in $La_{2-x}Sr_xCuO_4$. *Phys. Rev. Lett.* **68**, 345–348 (1992).

[114] C. Martins, B. Lenz, L. Perfetti, V. Brouet, F. Bertran, S. Biermann. Nonlocal Coulomb correlations in pure and electron-doped Sr_2IrO_4: Spectral functions, Fermi surface, and pseudo-gap-like spectral weight distributions from oriented cluster dynamical mean-field theory. *Phys. Rev. Mater.* **2**, 032001 (2018).

[115] C.-L. Song, Y.-P. Jiang, Y.-L. Wang, Z. Li, L. Wang, K. He, X. Chen, X.-C. Ma, Q.-K. Xue. Gating the charge state of single Fe dopants in the topological insulator Bi_2Se_3 with a scanning tunneling microscope. *Phys. Rev. B* **86**, 045441 (2012).

[116] V. W. Brar, R. Decker, H.-M. Solowan, Y. Wang, L. Maserati, K. T. Chan, H. Lee, Ç. O. Girit, A. Zettl, S. G. Louie, M. L. Cohen, M. F. Crommie. Gate-controlled ionization and screening of cobalt adatoms on a graphene surface. *Nat. Phys.* **7**, 43–47 (2011).

[117] D. T. Walkup. *Doping and strain effects in strongly spin-orbit coupled systems.* Ph.D. thesis, Boston College (2016).

[118] M. M. Ugeda, A. J. Bradley, S.-F. Shi, F. H. da Jornada, Y. Zhang, D. Y. Qiu, W. Ruan, S.-K. Mo, Z. Hussain, Z.-X. Shen, F. Wang, S. G. Louie, M. F. Crommie. Giant bandgap renormalization and excitonic effects in a monolayer transition metal dichalcogenide semiconductor. *Nat. Mater.* **13**, 1091–1095 (2014).

[119] D. Wong, Y. Wang, J. Jung, S. Pezzini, A. M. DaSilva, H.-z. Tsai, H. S. Jung, R. Khajeh, Y. Kim, J. Lee, S. Kahn, S. Tollabimazraehno, H. Rasool, K. Watanabe, T. Taniguchi, A. Zettl, S. Adam, A. H. MacDonald, M. F. Crommie. Local spectroscopy of moiré-induced electronic structure in gate-tunable twisted bilayer graphene. *Phys. Rev. B* **92**, 155409 (2015).

[120] M. Morgenstern, V. Gudmundsson, R. Dombrowski, C. Wittneven, R. Wiesendanger. Nonlocality of the exchange interaction probed by scanning tunneling spectroscopy. *Phys. Rev. B* **63**, 201301 (2001).

[121] F. Marczinowski, J. Wiebe, F. Meier, K. Hashimoto, R. Wiesendanger. Effect of charge manipulation on scanning tunneling spectra of single Mn acceptors in InAs. *Phys. Rev. B* **77**, 115318 (2008).

[122] F. Herbert, A. Krishnamoorthy, K. Van Vliet, B. Yildiz. Quantification of electronic band gap and surface states on $FeS_2(100)$. *Surf. Sci.* **618**, 53–61 (2013).

[123] A. Sabitova, P. Ebert, A. Lenz, S. Schaafhausen, L. Ivanova, M. Dähne, A. Hoffmann, R. E. Dunin-Borkowski, A. Förster, B. Grandidier, H. Eisele. Intrinsic

bandgap of cleaved ZnO(110) surfaces. *Appl. Phys. Lett.* **102**, 021608 (2013).

[124] K. Teichmann, M. Wenderoth, S. Loth, R. G. Ulbrich, J. K. Garleff, A. P. Wijnheijmer, P. M. Koenraad. Controlled Charge Switching on a Single Donor with a Scanning Tunneling Microscope. *Phys. Rev. Lett.* **101**, 076103 (2008).

[125] A. P. Wijnheijmer, J. K. Garleff, K. Teichmann, M. Wenderoth, S. Loth, P. M. Koenraad. Single Si dopants in GaAs studied by scanning tunneling microscopy and spectroscopy. *Phys. Rev. B* **84**, 125310 (2011).

[126] S. Loth, M. Wenderoth, L. Winking, R. G. Ulbrich, S. Malzer, G. H. Döhler. Probing Semiconductor Gap States with Resonant Tunneling. *Phys. Rev. Lett.* **96**, 066403 (2006).

[127] J. D. Jackson. Boundary-value problems with dielectrics. In *Class. Electrodyn.* John Wiley & Sons, third ed. (1999).

[128] S. Varyukhin, A. Zkharov. Anisotropic dielectric constant of La_2CuO_4. *Phys. C Supercond.* **185-189**, 975–976 (1991).

[129] S. Chikara, O. Korneta, W. P. Crummett, L. E. DeLong, P. Schlottmann, G. Cao. Giant magnetoelectric effect in the $J_{\text{eff}}=1/2$ Mott insulator Sr_2IrO_4. *Phys. Rev. B* **80**, 140407 (2009).

[130] A. P. Wijnheijmer, J. K. Garleff, K. Teichmann, M. Wenderoth, S. Loth, R. G. Ulbrich, P. A. Maksym, M. Roy, P. M. Koenraad. Enhanced Donor Binding Energy Close to a Semiconductor Surface. *Phys. Rev. Lett.* **102**, 166101 (2009).

[131] D.-H. Lee, J. A. Gupta. Tunable Control over the Ionization State of Single Mn Acceptors in GaAs with Defect-Induced Band Bending. *Nano Lett.* **11**, 2004–2007 (2011).

[132] H. Zheng, J. Kröger, R. Berndt. Spectroscopy of Single Donors at ZnO(0001) Surfaces. *Phys. Rev. Lett.* **108**, 076801 (2012).

[133] H. Zheng, A. Weismann, R. Berndt. Manipulation of Subsurface Donors in ZnO. *Phys. Rev. Lett.* **110**, 226101 (2013).

[134] G. A. Steele, R. C. Ashoori, L. N. Pfeiffer, K. W. West. Imaging Transport Resonances in the Quantum Hall Effect. *Phys. Rev. Lett.* **95**, 136804 (2005).

[135] Z. Wang, Y. Okada, J. O'Neal, W. Zhou, D. Walkup, C. Dhital, T. Hogan, P. Clancy, Y.-J. Kim, Y. F. Hu, L. H. Santos, S. D. Wilson, N. Trivedi, V. Madhavan. Disorder induced power-law gaps in an insulator–metal Mott transition. *Proc. Natl. Acad. Sci.* **115**, 11198–11202 (2018).

[136] J. L. Collins, A. Tadich, W. Wu, L. C. Gomes, J. N. B. Rodrigues, C. Liu, J. Hellerstedt, H. Ryu, S. Tang, S.-K. Mo, S. Adam, S. A. Yang, M. S. Fuhrer, M. T. Edmonds. Electric-field-tuned topological phase transition in ultrathin Na_3Bi. *Nature* **564**, 390–394 (2018).

[137] Y. Cao, V. Fatemi, S. Fang, K. Watanabe, T. Taniguchi, E. Kaxiras, P. Jarillo-Herrero. Unconventional superconductivity in magic-angle graphene superlattices. *Nature* **556**, 43–50 (2018).

[138] M. P. Allan, A. W. Rost, A. P. Mackenzie, Y. Xie, J. C. Davis, K. Kihou, C. H. Lee, A. Iyo, H. Eisaki, T.-M. Chuang. Anisotropic Energy Gaps of Iron-Based Superconductivity from Intraband Quasiparticle Interference in LiFeAs. *Science* **336**, 563–567 (2012).

[139] M. P. Allan, A. W. Rost, A. P. Mackenzie, Y. Xie, J. C. Davis, K. Kihou, C. H. Lee, A. Iyo, H. Eisaki, T.-M. Chuang. Anisotropic Energy Gaps of Iron-Based Superconductivity from Intraband Quasiparticle Interference in LiFeAs. *Science* **336**, 563–567 (2012).

[140] M. A. Sulangi, M. P. Allan, J. Zaanen. Revisiting quasiparticle scattering interference in high-temperature superconductors: The problem of narrow peaks. *Phys. Rev. B* **96**, 134507 (2017).

[141] M. A. Sulangi, J. Zaanen. Quasiparticle density of states, localization, and distributed disorder in the cuprate superconductors. *Phys. Rev. B* **97**, 144512 (2018).

[142] M. Itoh, T. Shimura, Y. Inaguma, Y. Morii. Structure of 2D conductor Sr_2RhO_4. *J. Solid State Chem.* **118**, 206 (1995).

[143] B. J. Kim, J. Yu, H. Koh, I. Nagai, S. I. Ikeda, S.-J. Oh, C. Kim. Missing xy-Band Fermi Surface in 4d Transition-Metal Oxide Sr_2RhO_4: Effect of the octahedra rotation on the electronic structure. *Phys. Rev. Lett.* **97**, 106401 (2006).

[144] G.-q. Liu, V. N. Antonov, O. Jepsen, O. K. Andersen. Coulomb-Enhanced Spin-Orbit Splitting: The Missing Piece in the Sr_2RhO_4 Puzzle. *Phys. Rev. Lett.* **101**, 026408 (2008).

[145] A. P. Mackenzie, Y. Maeno. The superconductivity of Sr_2RuO_4 and the physics of spin-triplet pairing. *Rev. Mod. Phys.* **75**, 657–712 (2003).

[146] G. Zhang, E. Gorelov, E. Sarvestani, E. Pavarini. Fermi Surface of Sr_2RuO_4: Spin-Orbit and Anisotropic Coulomb Interaction Effects. *Phys. Rev. Lett.* **116**, 106402 (2016).

[147] B. Stöger, M. Hieckel, F. Mittendorfer, Z. Wang, D. Fobes, J. Peng, Z. Mao, M. Schmid, J. Redinger, U. Diebold. High Chemical Activity of a Perovskite Surface: Reaction of CO with $Sr_3Ru_2O_7$. *Phys. Rev. Lett.* **113**, 116101 (2014).

[148] L. J. Sandilands, W. Kyung, S. Y. Kim, J. Son, J. Kwon, T. D. Kang, Y. Yoshida, S. J. Moon, C. Kim, T. W. Noh. Spin-Orbit Coupling and Interband Transitions in the Optical Conductivity of Sr_2RhO_4. *Phys. Rev. Lett.* **119**, 267402 (2017).

[149] T. Dahm, D. J. Scalapino. Quasi-particle interference probe of the self-energy. *New J. Phys.* **16**, 023003 (2014).

[150] A. J. Macdonald, Y.-S. Tremblay-Johnston, S. Grothe, S. Chi, P. Dosanjh, S. Johnston, S. A. Burke. Dispersing artifacts in FT-STS: a comparison of set point effects across acquisition modes. *Nanotechnology* **27**, 414004 (2016).

[151] Y. He, Y. Yin, M. Zech, A. Soumyanarayanan, M. M. Yee, T. Williams, M. C. Boyer, K. Chatterjee, W. D. Wise, I. Zeljkovic, T. Kondo, T. Takeuchi, H. Ikuta, P. Mistark, R. S. Markiewicz, A. Bansil, S. Sachdev, E. W. Hudson, J. E. Hoffman. Fermi Surface and Pseudogap Evolution in a Cuprate Superconductor. *Science* **344**, 608–611 (2014).

[152] C. M. Varma, P. B. Littlewood, S. Schmitt-Rink, E. Abrahams, A. E. Ruckenstein. Phenomenology of the normal state of Cu-O high-temperature superconductors. *Phys. Rev. Lett.* **63**, 1996–1999 (1989).

[153] J. Zaanen, Y.-W. Sun, Y. Liu, K. Schalm. *Holographic duality in condensed matter physics*. Cambridge University Press (2016).

[154] R. A. Davison, K. Schalm, J. Zaanen. Holographic duality and the resistivity of strange metals. *Phys. Rev. B* **89**, 245116 (2014).

[155] M. A. Sulangi, J. Zaanen. Self-energies and quasiparticle scattering interference. *Phys. Rev. B* **98**, 094518 (2018).

[156] A. V. Semenov, I. A. Devyatov, P. J. de Visser, T. M. Klapwijk. Coherent Excited States in Superconductors due to a Microwave Field. *Phys. Rev. Lett.* **117**, 047002 (2016).

Samenvatting

De elektronische eigenschappen van de meeste materialen om ons heen kunnen met het vrije-elektronenmodel worden beschreven. Dit betekent dat de elektronen in het materiaal bijna geen afstotende Coulombkracht voelen, en dat ze vrijwel onafhankelijk van elkaar behandeld kunnen worden.

De afstotende Coulombkracht is echter in sommige bijzondere materialen niet verwaarloosbaar. Deze materialen worden 'sterk gecorreleerde elektronensystemen' genoemd. De interacties tussen de elektronen leiden tot nieuw emergent, collectief gedrag, dat niet te verklaren is als een som van het gedrag van individuele elektronen. Gecorreleerde elektronen veroorzaken veel bijzondere verschijnselen in de fysica van de gecondenseerde materie. Een van de beroemdste voorbeelden hiervan is hogetemperatuursupergeleiding. Nog steeds begrijpen natuurkundigen niet helemaal hoe dit fenomeen werkt, en er is meer experimenteel en theoretisch onderzoek nodig om dit probleem helemaal te doorgronden.

Dit proefschrift beschrijft mijn bijdrage aan een beter begrip van sterk gecorreleerde elektronensystemen en bestaat uit twee delen. Eerst wordt het ontwerp en de constructie beschreven van een nieuwe, 'state-of-the-art' scanning tunneling microscoop (STM) om hogere datakwaliteit te bereiken. Dit is nodig om de allerkleinste details van sterk gecorreleerd elektronensystemen beter te kunnen meten. Daarna bestuderen we met scanning tunneling microscopie hoe de elektronische eigenschappen van een Mott-isolator veranderen als we extra elektronen aan het materiaal toevoegen door te doteren.

De techniek van scanning tunneling microscopie en spectroscopie wordt in hoofdstuk 2 beschreven. Met een STM kunnen we de toestandsdichtheid van de elektronen met atomaire resolutie meten. Dit is erg belangrijk bij sterk gecorreleerde elektronensystemen, omdat de elektronische structuur vaak op de nanoschaal varieert. Mede hierdoor heeft STM in de afgelopen twintig jaar bijgedragen aan cruciale ontdekkingen in het gebied van sterk gecorreleerde elektronsystemen. Toch is STM een moeilijke techniek;

de microscoop is heel gevoelig voor trillingen die de meting kunnen beïnvloeden door het signaal in de ruis te verbergen.

In hoofdstuk 3 van dit proefschrift beschrijf ik het ontwerp, de constructie en de prestatie van onze STM die we Dome noemen. Dome opereert bij de lage temperatuur van 4 Kelvin, en is extreem stijf. Een stijvere STM heeft als gevolg dat externe trillingen de meting minder beïnvloeden, en dus dat we makkelijker door de ruis heen kunnen kijken. Door gebruik te maken van stijve materialen, zoals saffier, en dit te combineren met eindige-elementenmethode om het ontwerp te verbeteren, hebben we, voor zover nu bekend, de stijfste lage temperatuur STM ter wereld gebouwd.

In hoofdstuk 4 en 5 bestuderen we het iridaat Sr_2IrO_4 met een andere STM. Dit materiaal is een Mott isolator door de sterke spin-baan koppeling. Mott isolatoren zijn een simpel voorbeeld van sterk gecorreleerde elektronensystemen. Als gevolg van de sterke afstotende Coulombkracht, zitten elektronen in dit soort materialen vast op hun atomen in het kristalrooster. Ze zijn dan 'bevroren', en het materiaal gedraagt zich als een elektrische isolator. In sommige Mott isolatoren kunnen de elektronen 'ontdooid' worden door extra elektronen aan het materiaal toe te voegen door middel van doteren. Echter zorgt het 'smelten' van de elektronen voor nieuwe exotische eigenschappen die nog niet helemaal begrepen worden omdat de sterke interacties tussen de elektronen nog steeds een grote rol spelen. Cupraten, bijvoorbeeld, kunnen door dotering van Mott isolatoren in hogetemperatuursupergeleiders veranderen.

In hoofdstuk 4 bestuderen we de licht gedoteerde Mott isolator $(Sr_{1-x}La_x)_2IrO_4$ (strontium lanthanum iridaat), waarin 2% tot 5% van de Sr-atomen door La-atomen zijn vervangen. Dit is in principe een compleet ander materiaal dan de cupraat-hogetemperatuursupergeleiders. Desondanks nemen we in dit materiaal dezelfde elektronische fasen waar die in cupraten bij lage doteringsniveaus gevonden zijn, namelijk 'pseudogap' en 'charge order'. Deze fasen zijn tot nu toe in geen enkel ander materiaal dan cupraten gevonden, en onze ontdekking toont aan dat ze universele eigenschappen zijn van een klasse van Mott isolatoren. Vervolgens bestuderen we hoe het smeltingsproces van de bevroren Mott fase precies plaats vindt. We vinden dat de extra elektronen tot een bepaald doteringsniveau geen invloed op de Mott isolator hebben. Pas boven deze drempel beginnen de bevroren elektronen te smelten. Bovendien gebeurt dit smeltingsproces plaatselijk in kleine 'pseudogap-plassen' van enkele nanometers rond de doteringsatomen. Aangezien de eigenschappen van de iridaten lijkt op die van de cupraten, voorspellen we dat als er een hoog genoeg doteringsniveau bereikt wordt, de iridaten ook supergeleiders zullen worden.

Tijdens het bestuderen van de iridaten stuitten we ook op een ander bijzonder verschijnsel. We zien hier dat bij een doteringspercentage van onder de 4%, strontium lanthanum iridaat geen goede geleider is. In hoofstuk 5, bestuderen we de oorzaak van dit verschijnsel. We zien hier dat het elektrisch veld bij de naald van de STM

het materiaal kan penetreren vanwege slechte afscherming door de elektronen. Dit verschijnsel is bekend in halfgeleiders onder de naam 'tip-induced band bending'. Het begrip van dit verschijnsel is belangrijk, aangezien het invloed zou kunnen hebben op het resultaat van de meting. Dit kan bijvoorbeeld resulteren in een verandering van de gemeten breedte van de 'Mott gap'. Bij lage doteringsniveaus meten we bij de iridaten een 'Mott gap' die afwijkt van eerder gepubliceerd onderzoek. We ontwikkelen een model dat voor 'tip-induced band bending' in Mott isolatoren corrigeert, waarmee we de echte breedte van de Mott gap in licht gedoteerd Sr_2IrO_4 terugkrijgen. Bovendien is ons model ook geschikt voor andere licht gedoteerde Mott isolatoren.

In hoofdstuk 6 presenteren we data van het rhodaat Sr_2RhO_4 dat met onze nieuwe zelfgebouwde STM Dome gemeten is. Dit materiaal is een goede geleider waarin de elektronen gecorreleerd zijn, en heeft goed gedefinieerde quasideeltjes. De quasideeltjes worden verstrooid door atomaire defecten in het materiaal, en vormen een interferentiepatroon in de toestandsdichtheid. Met STM maken we een beeld van het interferentiepatroon, en door Fouriertransformatie van deze beelden krijgen we informatie over de elektronische bandstructuur in de impulsruimte. We vergelijken onze STM data met ARPES data op hetzelfde preparaat. In het algemeen vinden we een goede overeenkomst tussen de twee technieken, maar er zijn kleine verschillen tussen de Fermi-snelheden. Deze verschillen zouden door artefacten van de technieken veroorzaakt kunnen worden, maar zouden ook op een fundamenteel verschil tussen de technieken kunnen duiden. We denken dat het belangrijk is om de oorzaak van de verschillen te vinden, maar om dat beter te bestuderen zijn verdere metingen nodig.

Ten slotte stellen we in hoofdstuk 7 drie experimenten voor die in de toekomst met Dome gedaan kunnen worden: het bestuderen van de vreemde-metaalfase in de cupraten, ruis-spectroscopie op sterk gecorreleerde elektronsystemen en de studie van de supergeleidingsfase van cupraten als we deze met microgolven exciteren.

Publications

1. **I. Battisti***, K.M. Bastiaans*, V. Fedoseev, A. de la Torre, N. Iliopoulos, A. Tamai, E.C. Hunter, R.S. Perry, J. Zaanen, F. Baumberger, M.P. Allan, 'Universality of pseudogap and emergent order in lightly doped Mott insulators', *Nat. Phys.* **13**, 21 (2017).

2. **I. Battisti**, V. Fedoseev, K.M. Bastiaans, A. de la Torre, R.S. Perry, F. Baumberger, M.P. Allan, 'Poor electronic screening in lightly doped Mott insulators observed with scanning tunneling microscopy', *Phys. Rev. B* **95**, 235141 (2017).

3. M. Leeuwenhoek, R.A. Norte, K.M. Bastiaans, D. Cho, **I. Battisti**, Y.M. Blanter, S. Gröblacher, M.P. Allan, 'Nanofabricated tips as a platform for double-tip and device based scanning tunneling microscopy', *submitted*, arXiv: 1712.08620.

4. K.M. Bastiaans*, D. Cho*, T. Benschop, **I. Battisti**, Y. Huang, M.S. Golden, Q. Dong, Y. Jin, J. Zaanen, M.P. Allan, 'Charge trapping and super-Poissonian noise centres in a cuprate superconductor', *Nat. Phys.* **14**, 1183 (2018).

5. **I. Battisti**, G. Verdoes, K. van Oosten, K.M. Bastiaans, M.P. Allan, 'Definition of design guidelines, construction, and performance of an ultra-stable scanning tunneling microscope for spectroscopic imaging', *Rev. Sci. Instr.* **89**, 123705 (2018).

6. **I. Battisti**, W. Tromp, R.S. Perry, A. Tamai, F. Baumberger, A.P. Mackenzie, M.P. Allan, 'Comparing spectroscopic techniques for band structure determination on the correlated metal Sr_2RhO_4', *in preparation.*

*These authors contributed equally.

Curriculum Vitae

Irene Battisti

Born on 11 March 1990, in Padova (Italy)

09.2004 - 06.2009	High School *Liceo Scientifico Copernico*, Verona, Italy
10.2009 - 07.2012	Bachelor of Science in Physics *Padova University*, Padova, Italy Graduation project: "Stochastic models in ecology" under the supervision of Prof. dr. A. Maritan.
10.2012 - 09.2014	Master of Science in Physics *Padova University*, Padova, Italy Graduation project "Towards the experimental investigation of current-induced forces" performed at *Leiden University* under the supervision of Prof. dr. J. van Ruitenbeek, with a 7-month Erasmus scholarship.
01.2015 - 05.2019	PhD in Physics *Leiden University*, Leiden, The Netherlands Graduation project: "Visualizing strongly-correlated electrons with a novel scanning tunneling microscope" under the supervision of Dr. M.P. Allan.

Acknowledgements

During the last four years I had the pleasure to work with many inspiring people who in different ways contributed to the results presented in this thesis. I am grateful for all the nice time, the discussions, and the help I received.

First of all, I would like to thank my supervisor Milan Allan for giving me the opportunity to be part of his research group from its very first day, for his trust in me, his patience and encouragement, and for all the discussions about fascinating physics and technical details. I really enjoyed it! I would also like to express my sincere gratitude to my promoter Jan Aarts, who always kept a careful eye on my progress and happiness.

Half of my time as a PhD student has been devoted to the construction of our home-built microscope *Dome*. Its development would not have been possible without the contribution of many different people. Gijsbert Verdoes and Kees van Oosten have played a major role, and it is mostly thanks to their expertise and outstanding capabilities that *Dome* smoothly came to be. I am grateful for the passion and time they put into this project, and for the mutual trust we always felt. Additionally, I want to acknowledge all the FMD and ELD members who, in different ways, contributed to the construction of the microscope: Martijn Witlox, Tristan van Klingeren, Emiel Wiegers, Doortje Oosterlee, Freek Groenewoud, Raymond Koehler, Ko Koning, Peter Veldhuizen and Bert Crama. Wilfred van der Geest always provided us with liquid helium, even when bad planning resulted in emergency needs.

I want to thank Marcel Rost for his patience and help with finite-element analysis and microscope characterization, Marcel Hesselberth for sharing his knowledge about everything concerning vibrations, and Federica Galli for all the (not only) STM-related conversations. I also really appreciated Ellie van Rijsewijk's help with administration and infinite patience whenever I had questions about bureaucracy.

During these years, I had the pleasure to work with five undergraduate students, all of whom taught me something. I would like to thank, in chronological order, Daniëlle van Klink, Sietske Lensen, Tjerk Benschop, Willem Tromp and Amber Vervloet.

Special thanks go to all the Allan Lab members for having been a very nice and stimulating team. In particular, I enjoyed sharing the exciting time on the iridates project with Koen Bastiaans, and working on tip-induced band bending with Vitaly Fedoseev. Discussions during group meetings or lunch with Maarten Leeuwenhoek, Doohee Cho, Damianos Chatzopoulos, and more recently Willem Tromp, Tjerk Benschop and Vincent Stalman have always been interesting, useful and fun.

I would also like to thank Jan Zaanen for the discussions about our STM data, and Tjerk Oosterkamp for the conversations inside and outside the group meetings.

Further, I want to thank our collaborators Alberto de la Torre, Anna Tamai and Felix Baumberger from University of Geneva and Robin Perry from University College London for suggesting to study iridates and rhodates with STM, providing us with samples, and for hosting me in Geneva when we still had no STM in Leiden.

I would not have enjoyed these years in Leiden as much if it was not for the atmosphere created at LION by many nice people, especially Sander Blok, Nikita Lebedev, Kaveh Lahabi, Gesa Welker, Martin de Wit, Daniël Geleen, Kim Akius, Tobias de Jong and Remko Fermin. Special thanks go to Johannes Jobst, for always understanding me and for not allowing this thesis to be less nice in appearance than in content.

Finally, I would like to thank my parents for always trusting in me and supporting my choices, even when it involved me moving far away from home. I feel fortunate to know that I can always count on their and my sisters' advice and support.